

CHANGES IN BONE TISSUE PROPERTIES WITH OSTEOPOROSIS TREATMENT

A Dissertation

Presented to the Faculty of the Graduate School

of Cornell University

in Partial Fulfillment of the Requirements for the Degree of

Doctor of Philosophy

by

Garry Robert Brock Jr

January 2015

© 2015 Garry Robert Brock Jr.

CHANGES IN BONE TISSUE PROPERTIES WITH OSTEOPOROSIS TREATMENT

Garry Robert Brock Jr

Cornell University 2015

Osteoporosis is a disease characterized by low bone mass leading to an increased risk of fracture. Bisphosphonate therapies are commonly prescribed medications that reduce the risk of osteoporotic fractures through reduced bone turnover. Recently, a rise in atypical femoral fractures (AFF) has occurred in patients taking long-term bisphosphonate treatments. These fractures have features similar to a fatigue failure; however, the mechanisms through which these fractures initiate are unknown. Knowledge of material property changes with bisphosphonates has been limited to monotonic tests and measures above the scale of bone structures. The purpose of this thesis was to examine the fatigue and nanoscale properties of bisphosphonate-treated cortical bone tissue.

To examine these properties an osteoporosis model was used in sheep followed by osteoporosis treatment: bisphosphonate (alendronate or zoledronate), SERM (raloxifene), PTH (teriparatide) or vehicle. Beams of known geometry were created from the cortical bone tissue and tested in four-point bend fatigue to failure. Differences in fatigue life occurred including a loss of fatigue life with alendronate and a rise in fatigue life with PTH treatment when compared to the grand mean. The lack of fatigue life change with zoledronate treatment indicates that factors such as dosage, method of administration, or chemical structure are affecting material properties, and not solely the class of drug. Increased fatigue life with PTH may indicate effectiveness for AFF treatment.

Fatigue loading induces microdamage in cortical bone tissue that is well characterized using microscale techniques. Bisphosphonate treatments are likely inducing changes to tissue properties at the nanoscale, below levels typically viewed with bone measure techniques. To examine nanoscale tissue damage, methods were developed and implemented using transmission-ray microscopy with synchrotron radiation to gain nanoscale imaging of fatigue damaged bone tissue. Heavy metal staining of microdamage was used, in conjunction with transmission x-ray tomography (TXM), to determine where damage initiates and forms at the nanoscale. Fatigue loaded samples had more staining present within the lacunar-canalicular network as compared to monotonic loaded samples. Damage may, therefore, be occurring within the bone structures themselves and not through surrounding tissue. The lacunar-canalicular network may be altered through bisphosphonate treatments, leading to development of novel imaging networks to examine these questions. Trabeculae were examined with TXM, and tomographies were created to compare nanoscale porosity. Results indicated porosity differences throughout trabeculae with the majority of the lacunar-canalicular network forming near the surface. The TXM methods are among the first studies to view bone at the nanoscale in three dimensions. Overall, results indicated differences in fatigue life of bone tissue given an osteoporosis treatment, with novel methods developed to help examine the origin of this difference.

BIOGRAPHICAL SKETCH

Garry Robert Brock Jr was born in Washington, D.C in 1986. He was raised in the Maryland and DC suburbs and graduated from Severna Park Senior High School in 2004. He attended college at Elizabethtown College in PA studying Engineering Physics. While there he completed research in biomechanical gait motion for restoring balance under the guidance of Prof. Kurt DeGoede. Garry was part of a solar splash team that competed in competitions with the team winning the award for most commercially viable hull. During his time at Etown he also completed two research experiences for undergraduate programs at the University of Maryland. His first summer was spent synthesizing quantum dots and determining adhesion to chitosan with scanning confocal microscopy. The second summer was spent building snake-inspired robots for proof of concept designs.

Garry then attended the University of Maryland- College Park and completed an MS in Mechanical Engineering under the guidance of Prof. Michael Pecht and Dr Michael Azarian in the Mechanical Engineering department. He completed research on understanding the reliability of standard and flexible termination capacitors under temperature- humidity-bias conditions. Garry graduated from UMD in May 2009 and took an internship at ITT Corporation working on development and implementation of a new electronic component for use in circuit development. Garry began his doctoral studies at Cornell University in August 2009 under the guidance of Marjolein van der Meulen. During his time at Cornell he has served as a teaching assistant twice for ENGRD 2020, serving as the head TA in the fall of 2013.

This work is dedicated to Robert E Pullman and Christopher Galdi.

ACKNOWLEDGEMENTS

The ability of complete this thesis would not have been possible without the help of many people. First and foremost, I would like to thank my advisor, Marjolein van der Meulen, for her help and mentorship with all of the projects and for allowing me to pursue a PhD. I would like to thank Christopher Hernandez, Anthony Ingraffea and Shefford Baker for serving as committee members and providing their expertise and help with these projects. I would also like to thank Adele Boskey for her input and expertise throughout these studies.

My lab members, Grace Kim, Frank Ko, Jayme Burket, Maureen Lynch, Katie Melville, Natalie Kelly, Olufunmilayo Adebayo, Julia Chen as well as the entire Cornell Biomechanics group for their insights and suggestions in future directions for the projects. Thank you to Judy Thoroughman and Marcia Sawyer for their help with all of the forms and order supplies. Thank you to the group at SSRL, Joy C Andrews, Yijin Liu, and Florian Meirer, for their help with using the TXM and associated coding.

Finally a thank you to my friends and family for their support. To my parents for their love and support throughout the graduate school process. Shama Iyer, thank you for your kindness and support.

Funding was provided by NIH AR053571, NIH AR041325, and NIH EB004321. Portions of this thesis were completed at Beamline 6-2c of the Stanford Synchrotron Radiation Lightsource (SSRL). Use of the Stanford Synchrotron Radiation Lightsource, SLAC National Accelerator Laboratory, is supported by the U.S. Department of Energy, Office of Science, Office of Basic Energy Sciences under Contract No. DE-AC02-76SF00515. This work made use of the Cornell Center for Materials Research Shared Facilities which are supported through the NSF MRSEC program (DMR-1120296).

TABLE OF CONTENTS

Chapter 1: Bone in a Clinical Setting.....	1
1.1 Osteoporosis.....	1
1.2 Osteoporosis Diagnosis.....	1
1.3 Bone Remodeling with Osteoporosis.....	1
1.4 Osteoporosis Related Fractures.....	2
1.5 Osteoporosis Treatment	3
1.6 Side Effects for Bisphosphonate Treatment	4
1.6.1 Atypical Femoral Fractures (AFF).....	4
1.6.2 Osteonecrosis of the Jaw	5
1.7 Bone in a Clinical Setting Summary.....	6
1.8 References.....	6
Chapter 2: Bone Properties and Their Analysis	11
2.1 Hierarchical Structure of Bone	11
2.2 Mechanical Property Measurements of Bone	12
2.3 Material Property Alterations with Bisphosphonate Treatment	14
2.4 Fatigue Properties of Bone.....	14
2.5 Microdamage in Bone.....	15
2.6 Imaging Bone Microdamage	15
2.7 Synchrotron Imaging of Bone.....	16
2.8 Study Objective and Importance.....	18
2.9 My Contribution.....	21
2.10 References.....	22
Chapter 3: The Effect of Osteoporosis Treatments on Fatigue Properties of Cortical Bone Tissue.....	28
3.1 Introduction.....	28
3.2 Materials and Methods.....	31
3.2.1 Animal Models	31
3.2.2 Sample Preparation.....	33
3.2.3 Fatigue Testing	33
3.2.4 Microcomputed Tomography (microCT).....	35

3.2.5 Statistical Analysis	35
3.3 Results.....	35
3.4 Discussion and Conclusions	39
3.5 References.....	42
Chapter 4: Nanoscale Examination of Microdamage in Sheep Cortical Bone using Synchrotron Radiation Transmission X-Ray Microscopy	47
4.1 Introduction.....	47
4.2 Materials and Methods.....	49
4.3 Results.....	53
4.4 Discussion and Conclusions	60
4.5 References.....	64
Chapter 5: Lacunar-Canalicular Network is Comprised Mainly of Canaliculi near the Trabecular Surface	69
5.1 Introduction.....	69
5.2 Materials and Methods.....	71
5.3 Results.....	74
5.4 Discussion and Conclusions	78
5.5 References.....	81
Chapter 6: Summary and Future Directions	85
6.1 Discussion and Summary.....	85
6.2 Future Directions	88
6.2.1 Continued Research Avenues.....	88
6.2.1.1 Osteoporosis Treatment Analysis	88
6.2.1.2 Continued Synchrotron Imaging.....	89
6.2.1.3 Continued AFF Analysis.....	90
6.2.2 New Research Avenues.....	90
6.2.2.1 New Osteoporosis Treatment Testing.....	90
6.2.2.2 New Synchrotron Imaging Methods.....	92
6.3 References.....	93
Chapter 7: Appendix A	97
Chapter 8: Appendix B.....	111
Chapter 9: Appendix C	138

LIST OF TABLES

1.1 Bisphosphonate Types and Their Relative Potencies4
3.1 Samples Used in Study32
5.1 Experimental design for treatment groups showing experimental duration72

LIST OF FIGURES

1.1 Schematic of Bone Remodeling.....	2
2.1 Hierarchical Structure of Bone	11
2.2 Whole Bone and Material Level Test Outcomes.....	13
2.3 Microdamage Imaging Techniques by Resolution	16
3.1 Comparison of Monotonic and Fatigue Loading.....	29
3.2 Setup for Four Point Bending Fatigue Loading.....	34
3.3 Initial Modulus for Each Group.....	36
3.4 Cycles to Failure for Each Group	37
3.5 Modulus Loss at Failure for Each Group.....	38
3.6 Mineralization Measures for Each Group.....	39
4.1 Representative TXM Image.....	49
4.2 Monotonic and Fatigue Stain Comparison	55
4.3 Increased Stain Uptake in Fatigue Loaded Samples.....	56
4.4 Different Damage Morphologies in Notched Samples	58
4.5 Summary of Damage Morphologies	59
4.6 Comparison of TXM with microCT.....	60
5.1 Lacunar-Canalicular Volumes within Trabeculae.....	74
5.2 Lacunar Density	75
5.3 Volume of a Single Lacunae	76
5.4 Lacunar-Canalicular Porosity as a Function of Depth	77
5.5 Illustrations of Lacunar Morphology	78

Chapter 1

Bone in a Clinical Setting

1.1 Osteoporosis

Osteoporosis is a disease characterized by low bone mass leading to an increased risk for fracture⁽¹⁾. The risk for developing osteoporosis typically increases greatly at the onset of menopause in women, as bone mass is lost after menopause⁽²⁾. In the United States in 2005 more than 2 million fractures were related to osteoporosis, leading to a total cost of \$19 billion⁽³⁾. Total fractures and the economic burden are both expected to rise by 50% by 2025⁽³⁾. Presence of a previous osteoporotic vertebral fracture leads to a five-fold increase in future fracture risk⁽⁴⁾. Women who experience a vertebral or hip fracture from osteoporosis have a 6-9 fold increase in mortality compared to individuals not having a fracture⁽⁵⁾.

1.2 Osteoporosis Diagnosis

Osteoporosis is typically diagnosed via a t-score for bone mineral density as measured with dual energy absorptiometry (DEXA)⁽⁶⁾. With this technique x-rays at two energies are used to determine the bone mineral density present at several locations in the skeleton. These measurements are then compared to the bone mineral density of a healthy, premenopausal individual, and t-scores are calculated to determine fracture risk. A t-score of -1.5 indicates that a person has osteopenia while a measurement below -2.5 indicates a person is osteoporotic⁽⁷⁾.

1.3 Bone Remodeling with Osteoporosis

Bone is continuously being remodeled, with older and damaged tissue being removed and replaced with new, less mineralized tissue^(8,9). Turnover of bone begins with the lacunar-canalicular network. The lacunar-canalicular network forms throughout the tissue and initiates

remodeling if damaged or old bone tissue is present⁽¹⁰⁾. Two types of cells complete the remodeling process, osteoclasts and osteoblasts. Osteoclasts remove damaged and older tissue creating a resorption cavity⁽¹⁰⁾. An osteoblast will then follow the osteoclast and fill in the resorbed bone tissue (Figure 1.1)⁽¹⁰⁾. The continual removal and replacement of damaged or old bone tissue ensures bone material properties are not compromised.

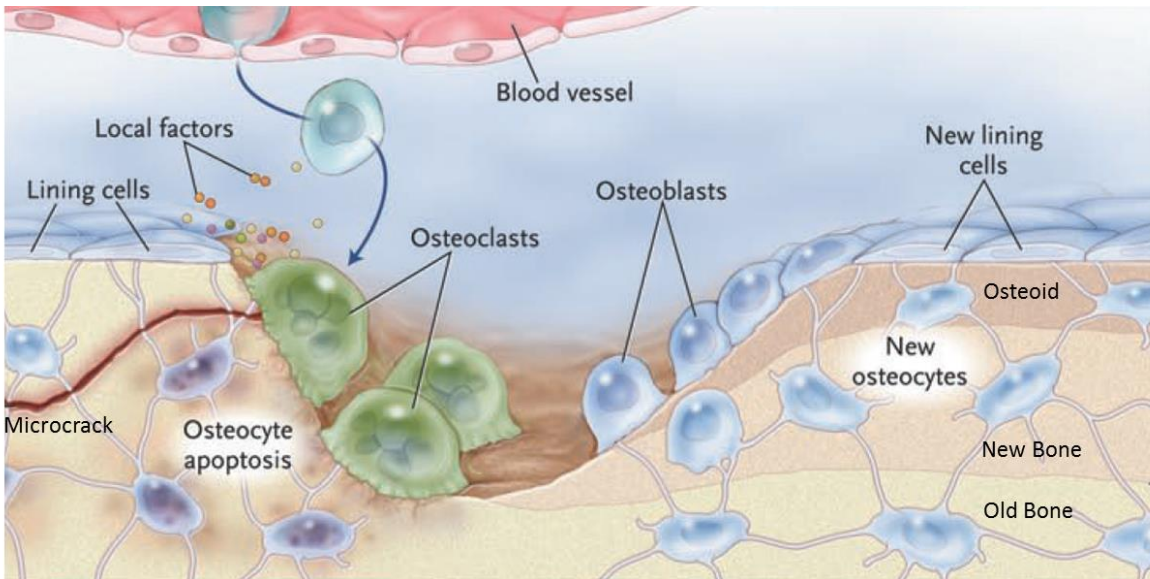


Figure 1.1: Schematic of bone remodeling. The lacunar-canalicular network signals to the osteoclast that bone needs to be remodeled. Osteoclasts remove this bone after which osteoblasts come in and apply new bone. Image adapted from Canalis et al. (10)

During osteoporosis the osteoclasts begin to resorb bone at a rate faster than the osteoblasts are able to rebuild bone, creating a net loss of bone⁽¹¹⁾. Over time this imbalance will cause a significant reduction in bone mass and increased risk of fracture.

1.4 Osteoporosis-Related Fractures

Osteoporosis reduces the bone volume of cancellous bone, leaving these regions susceptible to fracture. Fractures mainly occur in three regions: the vertebrae, hip and wrist⁽¹²⁾. Hip fractures are typically the result of a fall or mechanical overload that the person experiences⁽¹³⁾. A mechanical overload occurs to the tissue causing the femoral head or neck to fracture. Studies of

80-year-old patients who experienced a hip fracture have shown a decrease of 25% in life expectancy, and 17% of their remaining life being spent in a nursing facility, indicating significant mortality and morbidity associated with hip fractures⁽¹⁴⁾. Vertebral compression fractures occur due to a reduction in the total trabecular bone present, leading to a weakened overall structure. Repetitive loading and overload to the vertebrae can induce fracture. A population-based study showed that only 14% of vertebral fractures were due to severe trauma while 83% were due to minimal or no trauma⁽¹⁵⁾. Vertebral fractures serve as a risk factor for long-term morbidity and mortality in the elderly⁽¹⁶⁾.

1.5 Osteoporosis treatment

Osteoporotic treatments typically depend on the amount of BMD loss experienced. A small loss of BMD may be prevented or treated with increased calcium and vitamin D intake⁽¹⁷⁾.

Weightbearing exercise is also beneficial to bone, increasing the total BMD⁽¹⁸⁾. More significant bone loss typically is treated with drug intervention.

The most commonly prescribed drug therapies for osteoporosis are bisphosphonates. Bisphosphonates decrease osteoclast activity leading to a reduction in bone loss⁽¹⁹⁾. Reduced bone turnover reduces fracture risk up to 50% with a 0-8% increase in BMD⁽²⁰⁻²²⁾. The chemical structure varies by bisphosphonate type and generation leading to different potencies, binding affinities, and dosing regimens. Relative potency of bisphosphonates varies greatly with recent generations having a greater potency than previous ones (Table 1)⁽²³⁾. Bisphosphonates that do not contain nitrogen are known to form toxic adenosine triphosphate (ATP) analogs while nitrogen containing bisphosphonates inhibit farnesyl diphosphate (FPP) synthase⁽²⁴⁾(Table 1-1). Both nitrogen containing and non-nitrogen containing bisphosphonates promote osteoclast apoptosis; however, the method of this action differs depending on nitrogen presence.

Administration of bisphosphonates also varies, with both oral and intravenous methods being used^(25,26).

Table 1-1: Bisphosphonate types and their relative potencies. Adapted from ^(23,24,27-32)

Bisphosphonate	Nitrogen Containing	Relative Potency to Etidronate	Administration Method
Etidronate	No	1	Oral
Clodronate	No	10	Oral
Pamidronate	Yes	100	Intravenous
Olpadronate	Yes	200-500	Oral
Ibandronate	Yes	500-1000	Intravenous
Alendronate	Yes	1000-2000	Oral
Risedronate	Yes	2000	Oral
Zoledronate	Yes	10000	Intravenous

Selective estrogen receptor modulators (SERM) are also effective treatments for osteoporosis. SERM therapies reduce vertebral fracture risk 30-50%⁽²¹⁾. The affinity of SERMs to bind to pathways is similar to estradiol⁽³³⁾. Through binding to these pathways, SERM therapies function as an estrogen replacement for the bone. SERM therapies have side-effects and can cause thromboembolic effects on the body⁽³⁴⁾.

1.6 Side Effects from Bisphosphonate Treatment

1.6.1 Atypical Femoral Fractures (AFF)

Case studies over the past 10 years have reported instances of AFFs⁽³⁵⁾. These fractures occur within the cortical diaphysis, rather than the fracture occurring in the femoral neck. To understand these fractures better, the American Society for Bone and Mineral Research (ASBMR) formed a task force to examine and determine the prevalence and the risk of fractures^(36,37). This task force created a list of major features of AFFs that include: [1] Fractures are associated with minimal or no trauma, such as a fall from standing height or less; [2] Fractures are mostly transverse in orientation with a fracture line which originates at the lateral

cortex; [3] Incomplete fractures involve only the lateral cortex while complete fractures extend through both cortices and may be associated with a medial spike; [4] Fractures are noncomminuted or minimally comminuted; and, [5] Thickening at the periosteal or endosteal surface on the lateral cortex at the fracture site⁽³⁶⁾. AFFs are correlated with long-term bisphosphonate use^(38,39). The long-term use of bisphosphonates may suppress remodeling and lead to an increased risk of fatigue fracture⁽⁴⁰⁾. Incidence of AFF remains low⁽³⁹⁾; however, AFFs are associated with substantial morbidity often due to their bilateral nature⁽⁴¹⁾.

Treatment of an AFF depends on whether the fracture is complete or incomplete. Incomplete fractures are sometimes treated through discontinuation of bisphosphonate therapy⁽³⁶⁾. Parathyroid Hormone (PTH) has aided healing of incomplete stress fractures as compared to only discontinuation of bisphosphonate⁽⁴²⁾. PTH increases bone turnover, which may aid in AFF treatment⁽⁴³⁾. Microdamage quantities in the iliac crest of patients previously treated with alendronate were reduced with PTH⁽⁴⁴⁾.

1.6.2 Osteonecrosis of the Jaw

Osteonecrosis of the jaw is another recognized adverse side effect of bisphosphonate treatment⁽⁴⁵⁾. Duration of bisphosphonate treatment and bisphosphonate type may affect the occurrence of osteonecrosis of the jaw⁽⁴⁶⁾. Similar to atypical femoral fractures, the American Society of Bone and Mineral Research created a task force to examine osteonecrosis of the jaw⁽⁴⁷⁾. The definition of a confirmed case of osteonecrosis was stated by the task force as: “an area of exposed bone in the maxillofacial region that did not heal within 8 wk after identification by a health care provider, in a patient who was receiving or had been exposed to a bisphosphonate and had not had radiation therapy to the craniofacial region.”⁽⁴⁷⁾ The

pathophysiology of AFF and osteonecrosis are likely different; however, the pathophysiology of both side effects is poorly defined⁽⁴⁸⁾.

1.7 Bone in a Clinical Setting Summary

Bone tissue is continually changing within the body, allowing for repair and replacement of damaged or older tissue. During osteoporosis the tissue properties can become compromised leading to an increased risk of fracture. Through increased bone resorption with osteoporosis, bone loss occurs and weakens the overall structure. Osteoporosis treatments involve bisphosphonates that prohibit bone resorption preserving bone mass; however, these drugs have complications due to the inability to remodel older or damaged tissue. The occurrence of Atypical Femoral Fractures and Osteonecrosis indicates alterations to bisphosphonate treated bone tissue that need further examination.

1.8 References

1. Nordin BEC. The Definition and Diagnosis of Osteoporosis. *Calcif. Tissue Int.* 1987;40:57–8.
2. Nordin BE, MacGregor J, Smith DA. The incidence of osteoporosis in normal women: its relation to age and the menopause. *Q. J. Med.* 1966 Jan;35(137):25–38.
3. Burge R, Dawson-Hughes B, Solomon DH, Wong JB, King A, Tosteson A. Incidence and Economic Burden of Osteoporosis-Related Fractures in the United States, 2005–2025. *J. Bone Miner. Res.* 2007;22(3):465–75.
4. Lindsay R, Cooper C, Hanley DA, Barton I, Broy SB, Flowers K. Risk of New Vertebral Fracture in the Year Following a Fracture. *JAMA.* 2001;285:320–3.
5. Cauley JA, Thompson DE, Ensrud KC, Scott JC, Black D. Risk of Mortality Following Clinical Fractures. *Osteoporos. Int.* 2000;11:556–61.
6. Kanis JA. Diagnosis of osteoporosis and assessment of fracture risk. *Lancet.* 2002 Jun 1;359:1929–36.

7. Kanis JA, Melton LJ, Christiansen C, Johnston CC, Khaltaev N. The diagnosis of osteoporosis. *J. Bone Miner. Res.* 1994 Aug;9(8):1137–41.
8. Hill PA. Bone Remodelling. *Br. J. Orthod.* 1998;25:101–7.
9. Burr DB, Martin RB, Schaffler MB, Radin EL. Bone Remodelling in Response to in vivo Fatigue Microdamage. *J. Biomech.* 1985;18(3):189–200.
10. Canalis E, Giustina A, Bilezikian JP. Mechanisms of Anabolic Therapies for Osteoporosis. *N. Engl. J. Med.* 2007;357:905–16.
11. Manolagas SC, Jilka RL. Bone Marrow, Cytokines, and Bone Remodelling. *N. Engl. J. Med.* 1995;332(5):305–11.
12. Cummings SR, Melton LJ. Epidemiology and outcomes of osteoporotic fractures. *Lancet.* 2002 May 18;359:1761–7.
13. Greenspan SL, Myers ER, Maitland LA, Resnick NM, Hayes WC. Fall severity and bone mineral density as risk factors for hip fracture in ambulatory elderly. *JAMA.* 1994 Jan 12;271(2):128–33.
14. Braithwaite RS, Col NF, Wong JB. Estimating hip fracture morbidity, mortality and costs. *J. Am. Geriatr. Soc.* 2003 Mar;51(3):364–70.
15. Cooper C, Atkinson EJ, Fallon WMO, Melton LJ, Al CET. Incidence of Clinically Diagnosed Vertebral Fractures : A Population-Based Study in Rochester, Minnesota, 1985-1989. *J. Bone Miner. Res.* 1992;7(2):221–7.
16. Hasserijs R, Karlsson MK, Jónsson B, Redlund-Johnell I, Johnell O. Long-term morbidity and mortality after a clinically diagnosed vertebral fracture in the elderly--a 12- and 22-year follow-up of 257 patients. *Calcif. Tissue Int.* 2005 Apr;76:235–42.
17. Reid IR. Therapy of Osteoporosis: Calcium, Vitamin D, and Exercise. *Am. J. Med. Sci.* 1996;312(6):279–86.
18. Kohrt WM, Snead DB, Slatopolsky E, Birge SJ. Additive effects of weight-bearing exercise and estrogen on bone mineral density in older women. *J. Bone Miner. Res.* 1995 Sep;10(9):1303–11.
19. Delmas PD. How does antiresorptive therapy decrease the risk of fracture in women with osteoporosis? *Bone.* 2000 Jul;27(1):1–3.
20. Cummings SR, Karpf DB, Harris F, Genant HK, Ensrud K, LaCroix AZ, Black DM. Improvement in spine bone density and reduction in risk of vertebral fractures during treatment with antiresorptive drugs. *Am. J. Med.* 2002 Mar;112:281–9.

21. Ettinger B, Black DM, Mitlak BH, Knickerbocker RK, Nickelsen T, Genant HK, Christiansen C, Delmas PD, Zanchetta JR, Stakkestad J, Gluer CC, Krueger K, Cohen FJ, Eckert S, Ensrud KE, Avioli L V, Lips P, Cummings SR. Reduction of Vertebral Fracture Risk in Postmenopausal Women with Osteoporosis Treated with Raloxifene Results From a 3-Year Randomized Clinical Trial. *JAMA*. 1999;282(7):637–45.
22. Liberman UA, Weiss SR, Broll J, Minne HW, Quan H, Bell NH, Rodriguez-portales JA, Downs RW, Dequeker J, Favus MJ, Seeman E, Recker RR, Capizzi T, Santora AC, Lombardi A, Shah R V., Hirsch LJ, Karpf DB. Effect of Oral Alendronate on Bone Mineral Density and the Incidence of Fractures in Postmenopausal Osteoporosis. *N. Engl. J. Med.* 1995;333(22):1437–43.
23. Shaw NJ, Bishop NJ. Bisphosphonate treatment of bone disease. *Arch. Dis. Child.* 2005 May;90(5):494–9.
24. Reszka AA, Rodan GA. Bisphosphonate mechanism of action. *Curr. Rheumatol. Rep.* 2003 Feb;5:65–74.
25. Bone HG, Adami S, Rizoli R, Favus M, Ross PD, Santora A, Prahalada S, Daifotis A, Orloff J, Yates J. Weekly Administration of Alendronate: Rationale and Plan for Clinical Assessment. *Clin. Ther.* 2000;22(1):15–28.
26. Black DM, Delmas PD, Eastell R, Reid IR, Boonen S, Cauley JA, Cosman F, Lakatos P, Leung PC, Man Z, Mautalen C, Mesenbrink P, Hu H, Caminis J, Tong K, Rosario-jansen T, Krasnow J, Hue TF, Sellmeyer D, Eriksen EF, Cummings SR. Once-Yearly Zoledronic Acid for Treatment of Postmenopausal Osteoporosis. *N. Engl. J. Med.* 2007;356(18):1809–22.
27. Watts NB, Harris ST, Genant HK, Wasnich RD, Miller PD, Jackson RD, Licata AA, Ross PD, Woodson GC, Yanover MJ, Mysiw WJ, Kohse L, Rao MB, Steiger P, Richmond B, Chesnut CH. Intermittent Cyclical Etidronate Treatment of Postmenopausal Osteoporosis. *N. Engl. J. Med.* 1990;323(2):73–9.
28. Diel IJ, Solomayer E-F, Costa SD, Gollan C, Goerner R, Wallwiener D, Kaufmann M, Bastert G. Reduction in New Metastases in Breast Cancer with Adjuvant Clodronate Treatment. *N. Engl. J. Med.* 1998;339(6):357–63.
29. Berenson JR, Lichtenstein A, Porter L, Dimopoulos MA, Bordoni R, George S, Lipton A, Keller A, Ballester O, Kovacs MJ, Blacklock HA, Bell R, Simeone J, Reitsma DJ, Heffernan M, Seaman J, Knight RD. Efficacy of Pamidronate in Reducing Skeletal Events in Patients with Advanced Multiple Myeloma. *N. Engl. J. Med.* 1996;334(8):488–93.
30. Landsmeer-Beker E a., Massa GG, Maaswinkel-Mooy PD, van de Kamp JJP, Papapoulos SE. Treatment of osteogenesis imperfecta with the bisphosphonate olpadronate

- (dimethylaminohydroxypropylidene bisphosphonate). *Eur. J. Pediatr.* 1997 Sep 25;156:792–4.
31. Smith SY, Recker RR, Hannan M, Müller R, Bauss F. Intermittent intravenous administration of the bisphosphonate ibandronate prevents bone loss and maintains bone strength and quality in ovariectomized cynomolgus monkeys. *Bone.* 2003 Jan;32:45–55.
 32. Reginster J, Minne HW, Sorensen OH, Hooper M, Roux C, Brandi ML, Lund B, Ethgen D, Pack S, Roumagnac I, Eastell R. Randomized Trial of the Effects of Risedronate on Vertebral Fractures in Women with Established Postmenopausal Osteoporosis. *Osteoporos. Int.* 2000;11:83–91.
 33. Rey JRC, Cervino EV, Rentero ML, Crespo EC, Alvaro AO, Casillas M. Raloxifene: mechanism of action, effects on bone tissue, and applicability in clinical traumatology practice. *Open Orthop. J.* 2009 Jan;3:14–21.
 34. Gennari L, Merlotti D, Valleggi F, Martini G, Nuti R. Selective estrogen receptor modulators for postmenopausal osteoporosis: current state of development. *Drugs Aging.* 2007 Jan;24(5):361–79.
 35. Odvina C V, Levy S, Rao S, Zerwekh JE, Rao DS. Unusual mid-shaft fractures during long-term bisphosphonate therapy. *Clin. Endocrinol.* 2010 Feb;72:161–8.
 36. Shane E, Burr D, Abrahamsen B, Adler RA, Brown TD, Cheung AM, Cosman F, Curtis JR, Dell R, Dempster DW, Ebeling PR, Einhorn TA, Genant HK, Geusens P, Klaushofer K, Lane JM, McKiernan F, McKinney R, Ng A, Nieves J, O’Keefe R, Papapoulos S, Howe T Sen, van der Meulen MC, Weinstein RS, Whyte MP. Atypical subtrochanteric and diaphyseal femoral fractures: second report of a task force of the american society for bone and mineral research. *J. Bone Miner. Res.* 2014 Jan;29(1):1–23.
 37. Shane E, Burr D, Ebeling PR, Abrahamsen B, Adler RA, Brown TD, Cheung AM, Cosman F, Curtis JR, Dell R, Dempster D, Einhorn TA, Genant HK, Geusens P, Klaushofer K, Koval K, Lane JM, McKiernan F, McKinney R, Ng A, Nieves J, O’Keefe R, Papapoulos S, Sen HT, van der Meulen MCH, Weinstein RS, Whyte M. Atypical subtrochanteric and diaphyseal femoral fractures: report of a task force of the American Society for Bone and Mineral Research. *J. Bone Miner. Res.* 2010 Nov;25(11):2267–94.
 38. Isaacs JD, Shidiak L, Harris IA, Szomor ZL. Femoral insufficiency fractures associated with prolonged bisphosphonate therapy. *Clin. Orthop. Relat. Res.* 2010 Dec;468(12):3384–92.
 39. Schilcher J, Michaelsson K, Aspenberg P. Bisphosphonate Use and Atypical Fractures of the Femoral Shaft. *N. Engl. J. Med.* 2011;364(18):1728–37.

40. Van der Meulen MC, Boskey AL. Atypical subtrochanteric femoral shaft fractures: role for mechanics and bone quality. *Arthritis Res. Ther.* 2012 Aug 29;14(220):1–8.
41. Lo JC, Huang SY, Lee G a, Khandelwal S, Khandewal S, Provus J, Ettinger B, Gonzalez JR, Hui RL, Grimsrud CD. Clinical correlates of atypical femoral fracture. *Bone*; 2012 Jul;51:181–4.
42. Chiang CY, Zebaze RMD, Ghasem-Zadeh A, Iuliano-Burns S, Hardidge A, Seeman E. Teriparatide improves bone quality and healing of atypical femoral fractures associated with bisphosphonate therapy. *Bone*; 2013 Jan;52:360–5.
43. Sloan A V, Martin JR, Li S, Li J. Parathyroid hormone and bisphosphonate have opposite effects on stress fracture repair. *Bone*; 2010 Aug;47:235–40.
44. Dobnig H, Stepan JJ, Burr DB, Li J, Michalska D, Sipos A, Petto H, Fahrleitner-Pammer A, Pavo I. Teriparatide Reduces Bone Microdamage Accumulation in Postmenopausal Women Previously Treated With Alendronate*. *J. Bone Miner. Res.* 2009;24(12):1998–2006.
45. Ruggiero SL, Mehrotra B, Rosenberg TJ, Engroff SL. Osteonecrosis of the Jaws Associated with the Use of Bisphosphonates: A Review of 63 Cases. *J. Oral Maxillofac. Surg.* 2004 May;62:527–34.
46. Bamias A, Kastritis E, Bamia C, Moulopoulos LA, Melakopoulos I, Bozas G, Koutsoukou V, Gika D, Anagnostopoulos A, Papadimitriou C, Terpos E, Dimopoulos MA. Osteonecrosis of the Jaw in Cancer After Treatment With Bisphosphonates: Incidence and Risk Factors. *J. Clin. Oncol.* 2005;23(34):8580–7.
47. Khosla S, Burr D, Cauley J, Dempster DW, Ebeling PR, Felsenberg D, Gagel RF, Gilsanz V, Guise T, Koka S, Mccauley LK, MCGowan J, McKee MD, Mohla S, Pendrys DG, Raisz LG, Ruggiero SL, Shafer DM, Shum L, Silverman SL, Van Poznak CH, Watts N, Woo S-B, Shane E. Bisphosphonate-Associated Osteonecrosis of the Jaw: Report of a Task Force of the American Society for Bone and Mineral Research. *J. Bone Miner. Res.* 2007;22(10):1479–91.
48. Subramanian G, Fritton JC, Quek SYP. Osteonecrosis and atypical fractures-common origins? *Osteoporos. Int.* 2013 Mar 10;24(2):745–6.

Chapter 2

Bone properties and their analysis

2.1 Hierarchical structure of Bone

Bone is a composite structure comprised of many hierarchical levels to give strength and stiffness (Figure 2.1)⁽¹⁾. Bone is comprised of two types of tissue, cortical and cancellous (trabecular). Long bones, such as the femur and tibia, contain cortical shafts at the center and cancellous bone at the ends. The surface of cancellous bone is surrounded by a thin shell of cortical bone. Cancellous bone is made up of trabeculae that adapt the tissue to applied loads through changes in their thickness and separation⁽²⁾. Marrow space fills the inside of the cortical bone and also the regions between trabeculae⁽³⁾.

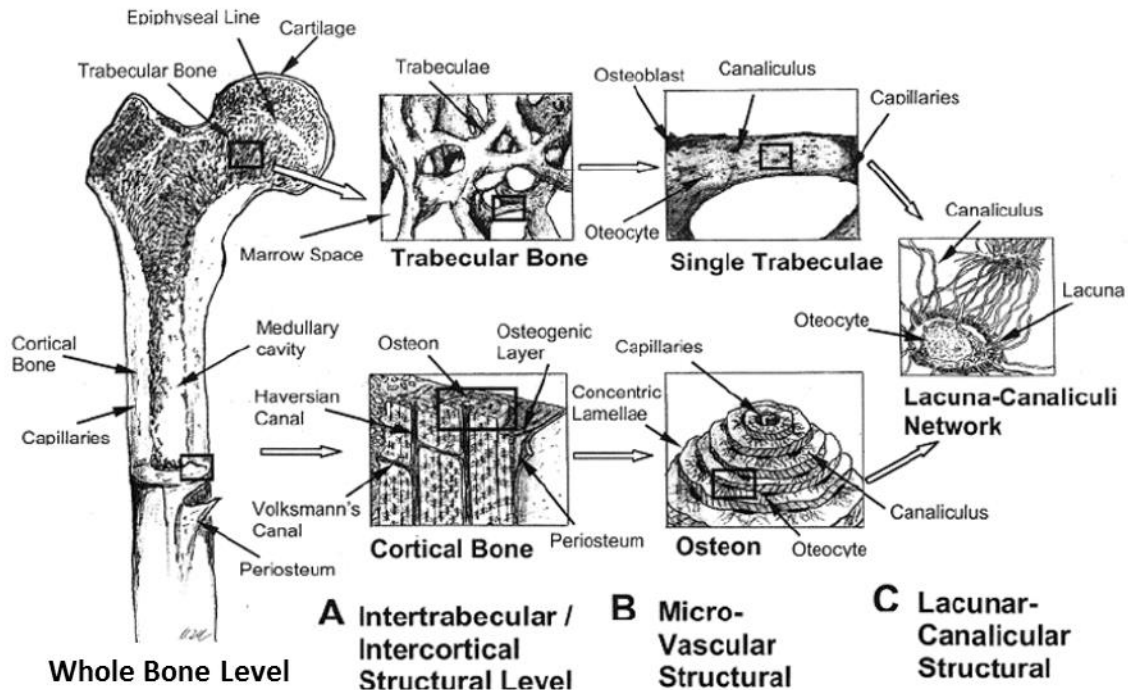


Figure 2.1: Hierarchical structure of bone. Image adapted from Liebschner & Wettergreen (1)

Quantification of cancellous bone involves analyzing the trabecular thickness, number, separation and bone volume fraction, which indicates the total tissue fraction present in a given volume⁽⁴⁾. Trabecular thickness is age dependent, with a loss of thickness occurring with age⁽⁵⁾. In cortical bone the singular structural unit is the osteon. Osteons are comprised of a Haversian canal at the center with concentric lamellae formed around these canals⁽³⁾. At the exterior of the osteon is a 1-5 micron thick cement line that may be a region of reduced mineralization⁽⁶⁾.

The micro-vascular and lacunar-canalicular levels illustrate the connective matrix within bone⁽¹⁾. Osteocytes sit in cavities known as lacunae, with emanating cellular processes, known as canaliculi, connecting osteocytes to one another⁽⁷⁾. Lacunae in human bone, as measured by synchrotron radiation, have axes lengths of $18.9 \pm 4.9\mu\text{m}$, $9.2 \pm 2.1\mu\text{m}$, and $4.8 \pm 1.1\mu\text{m}$ ⁽⁸⁾. Studies of canalicular size in mice indicated a 259 nm average diameter for canaliculi with the process inside having an average diameter of 104 nm⁽⁹⁾. Analyses of this tissue scale have been limited as canaliculi are below the typical resolution of bone imaging techniques. At the level below the lacunar canalicular network, mineral, organic matrix and water are the constituents of bone tissue⁽¹⁰⁾. Hydroxyapatite, the mineral phase of bone, consists primarily of calcium and phosphate while the organic matrix is mainly composed of collagen type I⁽³⁾.

2.2 Mechanical Property Measurements of Bone

Mechanical property analysis of bone involves two different types, whole bone level and tissue level (Figure 2.2). For whole bones, structural measurements depend on both the material properties and the geometry of the bone. The outcomes for these tests are typically: Stiffness, Strength, Failure Moment, Displacement at Failure and Energy Absorption. Results from whole bone measurements limit comparisons since the data can reflect a geometric change due to a

treatment, a material property change, or a combination of both. Strain gauging can be used for whole bone tests to get more accurate measures of material properties⁽¹¹⁾. Material (tissue) level tests are completed on samples of tissue of known geometry to determine exact material properties of the tissue using solid mechanics theory⁽¹²⁾. Material (tissue) level measures include the Young's Modulus, Ultimate Stress, Yield Stress, Strain at Failure and Toughness. Bone is anisotropic and using material level characterization techniques the full compliance matrix can be determined⁽¹³⁾.

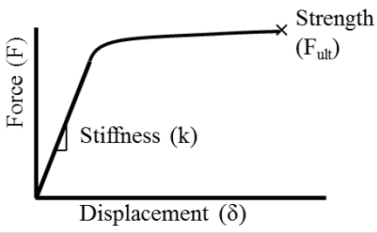
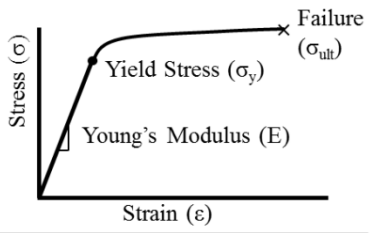
	Whole Bone Tests	Material Level Tests
Test Types	Whole bone bending, tension, compression, torsion	Micro-Beam Testing in tension compression, bending; Nanoindentation
Output Plot		
Outcome Measures	Strength, Stiffness, Displacement at Failure, Energy Absorption, Bending Moment	Ultimate Stress, Young's Modulus, Strain at Failure, Yield Stress, Toughness, Anisotropic Properties
Advantages	Functional testing measures	Exact material properties at specific locations are determined
Limitations	Alterations may be due to geometry, material property change, or localized tissue changes	Material property changes may not correlate to whole bone scale; Time intensive to create samples; Spatial heterogeneity

Figure 2.2: Whole bone and material level test outcomes

Nanoindentation can be used for nanoscale material property measurements of indentation modulus and hardness under hydrostatic compression. Measurements can be made in and around osteons with nanoindentation indicating interstitial and osteonal tissue properties^(14,15).

2.3 Material Property Alterations with Bisphosphonate Treatment

Tissue properties of individuals taking anti-resorptive therapies may be altered ⁽¹⁶⁻¹⁹⁾.

Bisphosphonate treatment reduced the heterogeneity of the mineral and matrix as measured by Fourier transform infrared spectroscopy imaging ⁽¹⁶⁾. At the whole bone level, bisphosphonates increase the strength and stiffness of bone tissue ⁽²⁰⁾. Bisphosphonate treatment is also associated with the presence of increased microdamage ⁽²¹⁻²³⁾. A loss of toughness occurred with bisphosphonate treatment; however, this result was determined to be a strain rate effect ^(20-22,24,25). No changes have been reported in the tissue modulus or ultimate stress with BP treatment ⁽²⁰⁾. As of 2010, no studies had examined fatigue properties or reaction to impact loading for bisphosphonate-treated tissue ⁽²⁶⁾. Fatigue properties are important to analyze since atypical femoral fractures have mechanisms similar to a fatigue fracture (stress fracture) ⁽²⁷⁾.

2.4 Fatigue Properties of Bone

To determine fatigue properties of cortical bone tissue uniform samples of known geometry must be tested. For cortical bone, fatigue properties on samples of known geometry depend on temperature, microstructure and stress amplitude ^(28,29). Fatigue life in cortical bone is also dictated by the time that the tissue is loaded for, not the total number of load cycles applied ⁽³⁰⁾. Damage initiation from fatigue loading of cortical bone tissue occurs at 2500 microstrain in tension, and 4000 microstrain in compression ⁽³¹⁾. Four-point bend fatigue studies have illustrated different damage morphologies by region with compressive damage being mainly linear microcracks and tensile damage being mainly diffuse ^(32,33). Alterations in the fatigue properties of cortical bone due to osteoporosis and treatments have not been extensively studied.

Alendronate reduced fatigue life of cortical tissue from the ribs of canines; however, the drug

dosage was supraphysiological, no osteoporosis model was used and samples were from a non-load bearing bone^(34,35).

2.5 Microdamage in Bone

Microdamage occurs in bone through activities of daily living⁽³⁶⁾. Microdamage consists of small cracks present in the bone tissue and can take one of three forms: linear microcracks, diffuse damage, or cross-hatch damage. Linear (discrete) microcracks are cracks that occur in interstitial bone and are smaller than vascular canals, but larger than canaliculi⁽³⁷⁾. Diffuse damage is characterized by a region of staining in which discrete cracks may or may not be visible⁽³²⁾. Cross-hatch microdamage is formed by patterned cracks occurring in the tissue⁽³⁸⁾. Microdamage accumulation causes a reduction in the strength, stiffness and energy dissipation properties of the tissue⁽³⁹⁾. A reduction of Young's Modulus of trabecular bone is also related to an increase of microdamage within the bone tissue⁽⁴⁰⁾.

2.6 Imaging of Bone Microdamage

Microdamage in bone can be imaged using a variety of histomorphometric stains and imaging methodologies (Figure 2.3). Two-dimensional methods involve light and fluorescent microscopy techniques in conjunction with basic fuchsin or fluorochrome stains in thin sections of bone⁽⁴¹⁾. Three-dimensional microdamage quantification can be completed using heavy metal stains in conjunction with microcomputed tomography (microCT)⁽⁴²⁾. Lead-uranyl acetate staining is correlated to bone microdamage in trabecular bone, with low bone volume and increased SMI correlated to more microdamage⁽⁴³⁾. Barium sulfide has also been used as a three-dimensional staining method for microdamage quantification⁽⁴⁴⁾. Fluorochrome stains can be used with serial milling to determine damaged regions within trabecular bone⁽⁴⁵⁾. Confocal microscopy also has been used for three dimensional microdamage analysis using fluorochrome stains⁽⁴⁶⁾. Scanning

electron microscopy (SEM) has been used in conjunction with lead-uranyl acetate staining methods to examine damage at the nanoscale; however, this technique only gives surface based information ⁽⁴⁷⁾. All of these techniques are limited by either being surface based or at the microscale, above resolutions necessary to analyze bone structures.

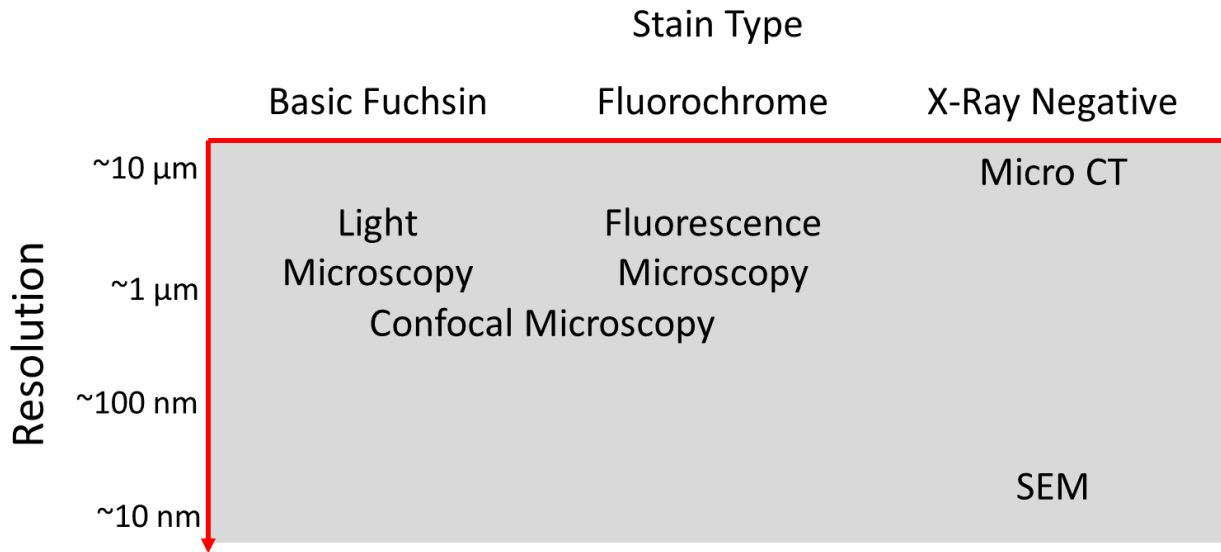


Figure 2.3: Microdamage imaging techniques as a function of resolution and stain type

2.7 Synchrotron Imaging of Bone

Synchrotron radiation imaging uses nanoscale wavelength x-rays to image samples through x-ray transmission, absorption and scattering. Visualization of the lacunar-canalicular network is feasible with synchrotron imaging and has been demonstrated with a 280 nm voxel size⁽⁴⁸⁾. Lacunar morphometry has been analyzed illustrating an ellipsoid shape ⁽⁸⁾. Comparisons of lacunar structures of mouse strains using synchrotron imaging indicated differences in the lacunae geometry ⁽⁴⁹⁾. Focused ion beam milling has been used to create samples of sufficient size for synchrotron analysis of the lacunar-canalicular network ⁽⁵⁰⁾. Microdamage has been

detected within trabeculae using synchrotron imaging with 3D image analysis techniques ⁽⁵¹⁾. Comparison of synchrotron CT and micro-CT techniques showed that the two techniques were correlated but that mineralization was underestimated with micro-CT⁽⁵²⁾. In vivo synchrotron radiation CT has been used to analyze the short-term dynamics of mouse trabecular bone microarchitecture⁽⁵³⁾; however, the spatial resolution was 11.7 μ m and the radiation dose of 5 Gy was high enough to impair bone growth in the long term ⁽⁵³⁾. These studies all have limitations associated with either larger voxel size or long scan times required collect sufficiently high resolution data. Imaging of the lacunar canalicular network in cortical bone at 65 nm required 36 hours for a single sample⁽⁵⁰⁾, limiting the possibility of collecting and comparing a large data set on a shared instrument.

Transmission X-Ray Microscopy (TXM) with synchrotron radiation is a novel imaging technique. A monochromatic hard x-ray source is used for imaging. This method has a demonstrated resolution of approximately 30 nm over a 20 to 30 micron field of view^(54,55). Two dimensional images can be combined to create a 3D tomography of a structure, and individual images with areas of overlap can be tiled to image larger regions ⁽⁵⁶⁾. The system has a depth of focus of approximately 50 microns, which can be extended using extended depth of focus algorithms ⁽⁵⁷⁾. TXM allows for determination of exact attenuation coefficient due to a monochromatic hard x-ray source. The x-ray attenuation is calculated as:

$$I = I_0 e^{-\mu t} \quad (1)$$

where I is the measured intensity, I_0 is the initial x-ray intensity, μ is the attenuation coefficient, and t is thickness of the sample. For bone mineralization, x-ray attenuation is proportional to the tissue mineralization. Thus, mineralization changes can be determined with nanoscale resolution

using TXM. Lacunar canalicular properties have also been examined with changes in lacunae area, perimeter and canaliculi occurring in mice exposed to microgravity⁽⁵⁸⁾.

2.8 Study Objective and Importance

The increased incidence of atypical fractures in osteoporotic individuals on antiresorptive therapies has led to questions about the mechanisms causing these fractures. The physiology of these fractures indicates fatigue is a likely component with these failures. Measurement of fatigue properties of treated bone tissue has been limited to a single study examining the effects of alendronate treatment in canine ribs⁽³⁴⁾. This prior study measured a loss of fatigue life with treatment; however, the drug dosage was supraphysiological, testing was completed on a non-load bearing bone, and no osteoporosis model was used⁽³⁴⁾. Microdamage increased with bisphosphonate treatment in animal models; however the implications for tissue properties is unclear and needs to be measured⁽²⁰⁻²²⁾. Increased microdamage with bisphosphonate treatment could reflect altered mechanical properties of the tissue, or the inability to repair damaged tissue. Zoledronate increased the mineral to matrix ratio in at the surface of sheep trabeculae leading to increased indentation modulus and hardness as measured by nanoindentation⁽¹⁴⁾. These surface based effects indicate that not all bisphosphonates have the same effects on bone. Bisphosphonates with higher binding affinity have less diffusion into the bone⁽⁵⁹⁾, which may indicate that bisphosphonates do not all have the same fatigue failure risk. Surface-based effects with some treatments may indicate different fatigue and fracture properties for tissues with different binding affinities. Alterations to the fatigue and fracture properties of treated bone tissue could influence a patient's susceptibility to an AFF.

The first objective of this thesis was to examine the fatigue properties of osteoporotic and treated cortical bone tissue. We hypothesized that fatigue life of cortical bone would be reduced

with bisphosphonate treatment, and preserved with SERM and PTH treatment. Beams of known geometry were created from the diaphysis of sheep femora. Sheep were given a metabolic acidosis (MA) diet followed by a bisphosphonate (alendronate or zoledronate), a SERM (raloxifene), parathyroid hormone, or vehicle. Samples were tested in four-point bend fatigue to failure. Initial modulus, cycles to failure, modulus loss at failure and TMD were measured and compared between groups. Initial modulus was greater with PTH treatment and its MA control. Alendronate elicited a reduction in fatigue life while PTH increased fatigue life as compared to the grand mean of the data set. TMD did not explain the differences. This result indicates that factors such as dosing duration, chemical structure and method of drug administration may affect the fatigue life of cortical bone tissue. Changes were not evident with TMD, leading to the question of why zoledronate and alendronate would alter fatigue properties differently despite a similar mechanism of action. Damage to bone tissue may initiate at the nanoscale for this result to hold true.

The second objective was to build on our first result and examine the nanoscale damage mechanisms of cortical bone tissue. Greater damage formation with alendronate treatment occurs at the microscale^(21,22); however, the mechanism by which this microdamage forms is unknown. We hypothesized that the microstructure of the bone would play a role in the initiation and propagation of damage to tissue. Beams of known geometry of sheep cortical bone were again created with a subset receiving a notch. Beams were then loaded using a monotonic or a fatigue load to create damage. Samples were stained with lead-uranyl acetate and sectioned to 50 microns. Imaging was completed using Transmission X-Ray Microscopy (TXM) with synchrotron radiation creating nanoscale resolution images of damage accumulation and morphologies. Three damage morphologies occurred in the tissue: discrete microcracks, damage

to existing bone structures and cross hatch microdamage. A greater amount of staining was present in samples following cyclic loading, not monotonic loading, as would be expected. The stain localized to existing bone structures within the tissue suggesting that damage may initiate within these structures. The lacunar-canalicular network is not typically visible with microdamage analysis techniques, and comparison of TXM and microCT-based damage measurement on the same sample illustrated damage measured with microCT was greater, likely due to partial volume effects associated with the larger voxel size. Damage initiation within the lacunar-canalicular network could be altered by different osteoporosis treatments that may change the nanoscale morphology.

The final objective was to examine the nanoscale porosity of tissue treated with bisphosphonates. Single trabeculae were excised from the condyles of sheep femurs given an osteoporosis model followed by bisphosphonate (alendronate or zoledronate) treatment, a SERM (raloxifene) or a vehicle. A separate group served as a control tissue and was not given any treatment. Samples were imaged using TXM with synchrotron radiation with projection images taken at 3 degree increments around the sample. Slices were reconstructed and compared between groups to examine how porosity changes within trabeculae. Surface-based alterations in material properties of trabeculae have occurred with bisphosphonate treatment; however, studies have not examined the lacunar-canalicular network to determine if alterations originate at the nanoscale. We hypothesized that alterations would be present in the lacunar-canalicular network with bisphosphonate treatment and that these changes should be evident by TXM-based tomography. The majority of the lacunar-canalicular network was present at the surface of the trabeculae. The greatest porosity occurred within the first 20 microns from the surface of the

trabeculae. The volume of porosity due to canaliculi was approximately twice the porosity resulting from lacunae.

2.9 My Contribution

In the first study, I developed and implemented four point bend fatigue testing of beams of known geometry. For this testing, my data is the first to demonstrate differences in fatigue life by bisphosphonate type. In conjunction with Julia Chen, we completed testing on PTH-treated samples that indicated improved fatigue life with PTH treatment. A manuscript is published in Bone Reports from this work and results were presented at the annual meeting of the ASBMR in 2013.

- **Brock GR**, Chen JT, Ingrassia AR, MacLeay J, Pluhar GE, Boskey AL, van der Meulen MCH (2015) The effect of osteoporosis treatments on fatigue properties of cortical bone tissue. Bone Reports 2: 8–13
- **Brock GR**, Ingrassia AR, MacLeay J, Boskey A, van der Meulen MCH (2013) Alterations to Cortical Bone Fatigue Life Depend on Bisphosphonate Type. J Bone Miner Res 28 (Suppl 1), LB-SA06

In the second study, I developed novel techniques for nanoscale microdamage evaluation using TXM. This study involved development of sample preparation methods, image reconstruction and image analysis. Differences were seen in nanoscale damage morphologies, with increased staining present within bone structures. This result is novel, as damage had never been viewed at this resolution using a projection image. These results indicate that damage morphologies are different at the nanoscale and may be influenced by the bone microstructure. These results were presented at the 2012 meeting of the Orthopaedic Research Society and published in PLoS One.

- **Brock GR**, Kim G, Ingrassia AR, Andrews JC, Pianetta P, van der Meulen MCH (2013) Nanoscale examination of microdamage in bone using synchrotron radiation transmission x-ray microscopy. *PLoS One* 8(3):e57942
- **Brock G**, Kim G, Andrews JC, Ingrassia AR, van der Meulen MCH (2012) A nanoscale examination of microdamage in cortical bone using synchrotron radiation transmission X-Ray microscopy. *Trans Orthop Res Soc* 37: 37: 137

In the final study I completed synchrotron tomographies of bone trabeculae to calculate nanoscale porosity measures of the tissue. For this project I developed a method for extracting individual trabeculae, mounting and imaging trabeculae with TXM, and for post-reconstruction image analysis. The majority of the lacunar-canalicular network existed at the surface of the trabeculae. The network was also composed of approximately twice the volume of canaliculi as lacunae. Differences were not detected with treatment. The methods developed in this study can be used to further examine alterations in continuum scale material properties due to osteoporosis treatments.

2.10 References

1. Liebschner MA., Wettergreen MA. Optimization of Bone Scaffold Engineering for Load Bearing Applications. In: Waris T, Ashammakhi N, editors. *Top. Tissue Eng.* 2003. p. 1–39.
2. Turner CH. Three rules for bone adaptation to mechanical stimuli. *Bone.* 1998 Nov;23(5):399–407.
3. Nordin M, Frankel VH. *Biomechanics of Bone. Basic Biomech. Musculoskelet. Syst.* Second. Malvern, Pennsylvania, USA: Lee & Febiger; 1989. p. 3–29.
4. Dempster DW, Compston JE, Drezner MK, Glorieux FH, Kanis JA, Malluche H, Meunier PJ, Ott SM, Recker RR, Parfitt AM. Standardized nomenclature, symbols, and units for bone histomorphometry: A 2012 update of the report of the ASBMR Histomorphometry Nomenclature Committee. *J. Bone Miner. Res.* 2013 Jan;28(1):1–16.
5. Ding M, Hvid I. Quantification of age-related changes in the structure model type and trabecular thickness of human tibial cancellous bone. *Bone.* 2000 Mar;26(3):291–5.

6. Burr DB, Schaffler MB, Frederickson RG. Composition of the Cement Line and its Possible Mechanical Role as a Local Interface in Human Compact Bone. *J. Biomech.* 1988;21(11):939–45.
7. Aarden EM, Burger EH, Nijweide PJ. Function of osteocytes in bone. *J. Cell. Biochem.* 1994 Jul;55:287–99.
8. Dong P, Hauptert S, Hesse B, Langer M, Gouttenoire P-J, Bousson V, Peyrin F. 3D osteocyte lacunar morphometric properties and distributions in human femoral cortical bone using synchrotron radiation micro-CT images. *Bone*; 2014 Mar;60:172–85.
9. You L-D, Weinbaum S, Cowin SC, Schaffler MB. Ultrastructure of the osteocyte process and its pericellular matrix. *Anat. Rec. A. Discov. Mol. Cell. Evol. Biol.* 2004 Jun;278:505–13.
10. Elliott SR, Robinson RA. The water content of bone. I. The mass of water, inorganic crystals, organic matrix, and CO₂ space components in a unit volume of the dog bone. *J. Bone Joint Surg. Am. The Journal of Bone and Joint Surgery*; 1957 Jan 1;39-A(1):167–88.
11. Turner CH, Burr DB. Basic Biomechanical Measurements of bone: A Tutorial. *Bone.* 1993;14:595–608.
12. Beer FP, Johnston ER, DeWolf JT. *Mechanics of Materials.* 4th ed. New York, NY: McGraw Hill; 1996. p. 308–63.
13. Ashman RB, Cowin SC, Van Buskirk WC, Rice JC. A continuous wave technique for the measurement of the elastic properties of cortical bone. *J. Biomech.* 1984;17(5):349–61.
14. Burket JC, Brooks DJ, MacLeay JM, Baker SP, Boskey AL, van der Meulen MCH. Variations in nanomechanical properties and tissue composition within trabeculae from an ovine model of osteoporosis and treatment. *Bone*; 2013 Jan;52(1):326–36.
15. Burket J, Gourion-Arsiquaud S, Havill LM, Baker SP, Boskey AL, van der Meulen MCH. Microstructure and nanomechanical properties in osteons relate to tissue and animal age. *J. Biomech*; 2011 Jan 11;44(2):277–84.
16. Donnelly E, Meredith DS, Nguyen JT, Gladnick BP, Rebolledo BJ, Shaffer AD, Lorich DG, Lane JM, Boskey AL. Reduced cortical bone compositional heterogeneity with bisphosphonate treatment in postmenopausal women with intertrochanteric and subtrochanteric fractures. *J. bone Miner. Res.* 2012 Mar;27(3):672–8.
17. Bala Y, Depalle B, Farlay D, Douillard T, Meille S, Follet H, Chapurlat R, Chevalier J, Boivin G. Bone micromechanical properties are compromised during long-term alendronate therapy independently of mineralization. *J. bone Miner. Res.* 2012 Apr;27(4):825–34.

18. Paschalis EP, Mendelsohn R, Boskey AL. Infrared assessment of bone quality. *Clin. Orthop. Relat. Res.* 2011 Aug;469(8):2170–8.
19. Roschger P, Paschalis EP, Fratzl P, Klaushofer K. Bone mineralization density distribution in health and disease. *Bone.* 2008 Mar;42(3):456–66.
20. Allen MR, Burr DB. Mineralization , Microdamage , and Matrix : How Bisphosphonates Influence Material Properties of Bone. *BoneKEy-Osteovision.* 2007;4(2):49–60.
21. Mashiba T, Hirano T, Turner CH, Forwood MR, Johnston CC, Burr DB. Suppressed bone turnover by bisphosphonates increases microdamage accumulation and reduces some biomechanical properties in dog rib. *J. Bone Miner. Res.* 2000 Apr;15(4):613–20.
22. Mashiba T, Turner CH, Hirano T, Forwood MR, Johnston CC, Burr DB. Effects of suppressed bone turnover by bisphosphonates on microdamage accumulation and biomechanical properties in clinically relevant skeletal sites in beagles. *Bone.* 2001 May;28(5):524–31.
23. Yamagami Y, Mashiba T, Iwata K, Tanaka M, Nozaki K, Yamamoto T. Effects of minodronic acid and alendronate on bone remodeling, microdamage accumulation, degree of mineralization and bone mechanical properties in ovariectomized cynomolgus monkeys. *Bone;* 2013 May;54(1):1–7.
24. Komatsubara S, Mori S, Mashiba T, Ito M, Li J, Kaji Y, Akiyama T, Miyamoto K, Cao Y, Kawanishi J, Norimatsu H. Long-term treatment of incadronate disodium accumulates microdamage but improves the trabecular bone microarchitecture in dog vertebra. *J. Bone Miner. Res.* 2003 Mar;18(3):512–20.
25. Smith ER, Allen MR. Bisphosphonate-Induced Reductions in Rat Femoral Bone Energy Absorption and Toughness Are Testing Rate-Dependent. *J. Orthop. Res.* 2013 Mar 13;31(2):16–21.
26. Allen MR, Burr DB. Bisphosphonate effects on bone turnover, microdamage, and mechanical properties: what we think we know and what we know that we don't know. *Bone;* 2011 Jul;49(1):56–65.
27. Van der Meulen MC, Boskey AL. Atypical subtrochanteric femoral shaft fractures: role for mechanics and bone quality. *Arthritis Res. Ther.* 2012 Aug 29;14(220):1–8.
28. Carter DR, Hayes WC, Schurman DJ. Fatigue life of compact bone-II. Effects of microstructure and density. *J. Biomech. Eng.* 1976;9:211–8.
29. Carter DR, Hayes WC. Fatigue life of compact bone-I: Effects of stress amplitude, temperature and density. *J. Biomech.* 1976 Jan;9(1):27–34.

30. Zioupos P, Currey JD, Casinos A. Tensile Fatigue in Bone: Are Cycles-, or Time to Failure, or Both, Important? *J. Theor. Biol.* 2001 Jun 7;210:389–99.
31. Pattin CA, Caler WE, Carter DR. Cyclic mechanical property degradation during fatigue loading of cortical bone. *J. Biomech.* 1996 Jan;29(1):69–79.
32. Boyce TM, Fyhrie DP, Glotkowski MC, Radin EL, Schaffler MB. Damage type and strain mode associations in human compact bone bending fatigue. *J. Orthop. Res.* 1998 May;16(3):322–9.
33. Diab T, Vashishth D. Effects of damage morphology on cortical bone fragility. *Bone.* 2005 Jul;37(1):96–102.
34. Bajaj D, Geissler JR, Allen MR, Burr DB, Fritton JC. The resistance of cortical bone tissue to failure under cyclic loading is reduced with alendronate. *Bone*; 2014 Apr 1;64:57–64.
35. Geissler JR, Bajaj D, Allen MR, Burr DB, Fritton JC. Alendronate Treatment Elicits a Reduction in Fatigue-Life of Canine Cortical Bone. *Trans. Orthop. Res. Soc.* 2012;37(37):0089.
36. Muir P, Johnson KA, Ruaux-Mason CP. In Vivo Matrix Microdamage in a Naturally Occurring Canine Fatigue Fracture. *Bone.* 1999;25(5):571–6.
37. Burr DB, Stafford T. Validity of the bulk staining technique to separate artifactual from in vivo bone microdamage. *Clin. Orthop. Relat. Res.* 1990;260:305–8.
38. Wenzel TE, Schaffler MB, Fyhrie DP. In vivo trabecular microcracks in human vertebral bone. *Bone.* 1996 Aug;19(2):89–95.
39. Burr D. Microdamage and bone strength. *Osteoporos. Int.* 2003 Sep;14 Suppl 5:S67–72.
40. Lambers FM, Bouman AR, Rimnac CM, Hernandez CJ. Microdamage caused by fatigue loading in human cancellous bone: relationship to reductions in bone biomechanical performance. *PLoS One.* 2013 Jan;8(12):e83662.
41. Lee TC, Mohsin S, Taylor D, Parkesh R, Gunnlaugsson T, O'Brien FJ, Giehl M, Gowin W. Detecting microdamage in bone. *J. Anat.* 2003 Aug;203(2):161–72.
42. Tang SY, Vashishth D. A non-invasive in vitro technique for the three-dimensional quantification of microdamage in trabecular bone. *Bone.* 2007;40:1259–64.
43. Karim L, Vashishth D. Role of trabecular microarchitecture in the formation, accumulation, and morphology of microdamage in human cancellous bone. *J. Orthop. Res.* 2011 Apr 27;1–6.

44. Leng H, Wang X, Ross RD, Niebur GL, Roeder RK. Micro-computed tomography of fatigue microdamage in cortical bone using a barium sulfate contrast agent. *J. Mech. Behav. Biomed. Mater.* 2008 Jan;1(1):68–75.
45. Bigley RF, Singh M, Hernandez CJ, Kazakia GJ, Martin RB, Keaveny TM. Validity of serial milling-based imaging system for microdamage quantification. *Bone.* 2008 Jan;42(1):212–5.
46. Mohsin S, O'Brien FJ, Lee TC. Microcracks in compact bone: a three-dimensional view. *J. Anat.* 2006 Jul;209(1):119–24.
47. Schaffler MB, Pitchford WC, Choi K, Riddle JM. Examination of compact bone microdamage using back-scattered electron microscopy. *Bone.* 1994;15(5):483–8.
48. Pacureanu A, Langer M, Boller E, Tafforeau P, Peyrin F. Nanoscale imaging of the bone cell network with synchrotron X-ray tomography: optimization of acquisition setup. *Med. Phys.* 2012;39(4):2229–38.
49. Schneider P, Stauber M, Voide R, Stampanoni M, Donahue LR. Ultrastructural Properties in Cortical Bone Vary Greatly in Two Inbred Strains of Mice as Assessed by Synchrotron Light Based Micro- and Nano-CT. *J. Bone Miner. Res.* 2007;22(10):1557–70.
50. Dierolf M, Menzel A, Thibault P, Schneider P, Kewish CM, Wepf R, Bunk O, Pfeiffer F. Ptychographic X-ray computed tomography at the nanoscale. *Nature.* Nature Publishing Group; 2010 Sep 23;467(7314):436–9.
51. Larrue A, Rattner A, Peter Z-A, Olivier C, Laroche N, Vico L, Peyrin F. Synchrotron Radiation Micro-CT at the Micrometer Scale for the Analysis of the Three-Dimensional Morphology of Microcracks in Human Trabecular Bone. Brechbiel MW, editor. *PLoS One.* 2011 Jul 7;6(7):e21297.
52. Kazakia GJ, Burghardt a. J, Cheung S, Majumdar S. Assessment of bone tissue mineralization by conventional x-ray microcomputed tomography: Comparison with synchrotron radiation microcomputed tomography and ash measurements. *Med. Phys.* 2008;35(7):3170.
53. Matsumoto T, Nishikawa K, Tanaka M, Uesugi K. In vivo CT quantification of trabecular bone dynamics in mice after sciatic neurectomy using monochromatic synchrotron radiation. *Calcif. Tissue Int.* 2011 May;88(5):432–41.
54. Andrews JC, Almeida E, van der Meulen MCH, Alwood JS, Lee C, Liu Y, Chen J, Meirer F, Feser M, Gelb J, Rudati J, Tkachuk A, Yun W, Pianetta P. Nanoscale X-ray microscopic imaging of mammalian mineralized tissue. *Microsc. Microanal.* 2010 Jun;16:327–36.

55. Andrews JC, Brennan S, Pianetta P, Ishii H, Gelb J, Feser M, Rudati J, Tkachuk a, Yun W. Full-field transmission x-ray microscopy at SSRL. *J. Phys. Conf. Ser.* 2009 Sep 1;186:012002.
56. Liu Y, Meirer F, Williams PA, Wang J, Andrews JC, Pianetta P. TXM-Wizard: a program for advanced data collection and evaluation in full-field transmission X-ray microscopy. *J. Synchrotron Radiat. International Union of Crystallography*; 2012 Mar;19:281–7.
57. Liu Y, Wang J, Hong Y, Wang Z, Zhang K, Williams PA, Zhu P, Andrews JC, Pianetta P, Wu Z. Extended depth of focus for transmission x-ray microscope. *Opt. Lett.* 2012;37(17):3708–10.
58. Blaber E a, Dvorochkin N, Lee C, Alwood JS, Yousuf R, Pianetta P, Globus RK, Burns BP, Almeida EAC. Microgravity induces pelvic bone loss through osteoclastic activity, osteocytic osteolysis, and osteoblastic cell cycle inhibition by CDKN1a/p21. *PLoS One.* 2013 Jan;8(4):e61372.
59. Nancollas GH, Tang R, Phipps RJ, Henneman Z, Gulde S, Wu W, Mangood a, Russell RGG, Ebetino FH. Novel insights into actions of bisphosphonates on bone: differences in interactions with hydroxyapatite. *Bone.* 2006 May;38(5):617–27.

Chapter 3

The Effect of Osteoporosis Treatments on Fatigue Properties of Cortical Bone Tissue¹

3.1 Introduction

Osteoporotic fractures are a substantial public health concern with total fractures and associated costs estimated to continue to rise through 2025⁽¹⁾. Bisphosphonates are a commonly prescribed class of anti-resorptive drug that increase bone mineral density between 0-8% while reducing the risk of fracture by up to 50% in osteoporotic patients^(2,3). The large decrease in fracture risk despite the modest increase in bone mineral density suggests a material property change in bisphosphonate-treated tissue. Suppression of bone remodeling with bisphosphonates has led to concern over inability to repair damaged and older tissue⁽⁴⁾. To fully understand the reduction in fracture risk, all fracture properties and mechanisms should be examined.

Fracture of osteoporotic bone typically occurs through one of two mechanisms, a single overload (traumatic failure), or repetitive sub-fracture loads (fatigue failure; Figure 3.1). Typical osteoporotic hip fractures are due to mechanical overload, in which the femoral head and neck are subjected to loads that the bone cannot withstand due to reduced bone mass. Fatigue loads are repetitive, sub-failure forces applied to the tissue. Activities of daily living create fatigue loads that in turn create microdamage in the tissue⁽⁵⁾. Healthy individuals are unlikely to experience fatigue fractures under normal loading conditions since damage to the bone is typically repaired before fracture can occur. However, tissue properties may be altered in individuals using anti-resorptive treatments⁽⁶⁻⁹⁾. Knowledge of fatigue on bone tissue has been

¹Reprinted from: Garry R. Brock, Julia T. Chen, Anthony R. Ingraffea, Jennifer MacLeay, G. Elizabeth Pluhar, Adele L. Boskey, Marjolein C.H. van der Meulen. The effect of osteoporosis treatments on fatigue properties of cortical bone tissue. *Bone Reports* 2 (2015) 8–13.

primarily gained from testing of machined sections of bones and has shown fatigue dependence with temperature, stress amplitude, and bone microstructure⁽¹⁰⁻¹²⁾. Studies examining fatigue of osteoporotic and treated tissue have focused on microdamage accumulation rather than the material properties of the tissue⁽⁴⁾.

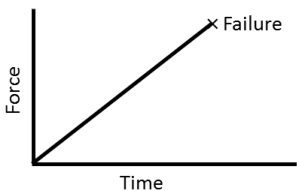
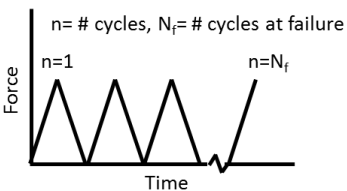
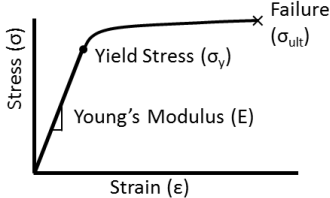
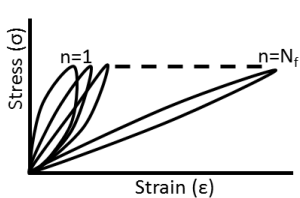
	Monotonic Loading	Fatigue Loading
Clinical Occurrence	Falls, blunt force trauma	Activities of daily living, including running
Load Levels	Single load applied to failure	Repetitive sub-failure loads applied
Force Applied over Time		
Stress - Strain		
Failure Mode	Failure when material is loaded to ultimate stress	Cracks (microdamage) formed during each cycle until a critical level is reached inducing failure

Figure 3.1: Comparison of monotonic and fatigue loading. In monotonic loaded samples, force is increased until the sample fails. In fatigue, a repetitive sub-failure load is applied creating damage that eventually coalesces to cause failure.

Bisphosphonates act through osteoclast inhibition, which leads to reduced bone turnover, increased bone mass and increased mineralization⁽¹³⁾. However, injury within tissue cannot be remodeled leading to an accumulation of microdamage⁽¹⁴⁻¹⁷⁾. Reduced bone turnover with bisphosphonate treatment increases mineralization and collagen maturity in bone tissue as measured by Fourier transform infrared spectroscopy (FTIR)⁽¹⁸⁾. Tests on whole bones after

bisphosphonate therapy indicate an increase in monotonic strength and stiffness at corticocancellous sites without concomitant changes to the tissue-level modulus or ultimate strength^(4,17). A loss of toughness and energy dissipation in cortical and cancellous tissue has been found with bisphosphonate treatment⁽⁴⁾. Fatigue properties are likely altered with bisphosphonate treatment; however, minimal data regarding these properties have been published⁽⁴⁾. Increased microdamage in both cortical and cancellous tissue with bisphosphonate treatment may reflect an inability to repair damage within the tissue⁽¹⁴⁻¹⁷⁾. Alendronate reduced the fatigue life in beams created from rib bones from healthy canines; however, the dosing was supraphysiological and osteoporosis was not induced prior to treatment⁽¹⁹⁾.

Long-term bisphosphonate use is associated with atypical femoral fractures (AFF)^(20,21). AFF incidence with bisphosphonate use is relatively low, but is associated with considerable morbidity⁽²²⁾. The mechanics of these fractures indicate critical differences from typical osteoporotic fractures^(23,24). Association with low loads indicates AFFs result from repetitive (fatigue) loading rather than a single traumatic incident. The transverse nature of the fractures suggests altered material properties with tissue becoming more brittle.

Bisphosphonates are the most common therapy prescribed for osteoporosis treatment, but other treatments exist. Selective Estrogen Receptor Modulators (SERM) reduce osteoporotic vertebral fracture risk by 30-50%⁽²⁵⁾. SERMs bind to the estrogen receptors with an affinity similar to estradiol⁽²⁶⁾. Teriparatide (PTH) has been beneficial in patients who experience AFFs by inducing increased bone remodeling, removal of older more fully mineralized tissue and replacement with new less fully mineralized tissue⁽²⁷⁾. Mechanical property data for SERM and PTH treatments of bone have focused on monotonic failure properties and have not included fatigue.

The purpose of this study was to examine the fatigue and fracture properties of bone tissue after different osteoporosis treatments using a sheep model of osteopenia to determine if a correlation exists between fatigue life and treatment type. Osteopenia was induced in sheep and followed by an osteoporosis treatment or vehicle. Beams of known geometry created from the femoral diaphysis of these sheep were loaded in four-point bending fatigue to failure. Given the inhibition of remodeling, and increased mineralization and collagen maturity reported with bisphosphonate treatment, we theorized that a shorter fatigue life will occur with bisphosphonate treatment.

3.2 Materials and Methods

3.2.1 Animal Model

Samples used in this study were from remaining femur tissue from previously published and in progress studies⁽²⁸⁾. For all studies we fed a metabolic acidosis (MA) diet to skeletally mature sheep to induce osteopenia⁽²⁹⁾. In the first study, sheep fed a normal diet served as healthy controls for the experiment (C, n=6). In the second study, sheep were fed the MA diet for 12 months and given Alendronate (ALN; n=2), Raloxifene (RAL; n=2) or a vehicle (MA1; n=3) treatment during months 7-12. The low sample sizes were not planned and reflect factors beyond our control in the experiment. To further examine bisphosphonate treatment, a third experiment was performed with sheep fed a MA diet for 8 months followed by 6 months of treatment with Zoledronate (Reclast, ZOL; n=6) or vehicle (MA2; n=6) while continuing the MA diet. The longer initial MA term in experiment three was due a delay in procuring the zoledronate. In the second study, alendronate (0.15 mg/kg) and raloxifene (0.8 mg/kg) were administered daily via a cannula placed into the duodenum, whereas zoledronate (5 mg/sheep) was administered as a single intravenous injection. This schedule replicates the clinical dosing in which alendronate is

taken orally daily or weekly and zoledronate is administered intravenously once a year^(30,31). All animal procedures were reviewed and approved by the Colorado State University IACUC and the Hospital for Special Surgery IACUC.

Table 3.1: Samples used were four different studies: [1] Age-matched control sheep fed a normal diet (Control); [2] Sheep were fed a metabolic acidosis (MA) diet for six months followed by the MA diet and twelve months of MA diet and treated by vehicle (MA1), raloxifene (RAL) or alendronate (ALN); [3] Sheep were fed an MA diet for eight months followed by six months of the MA diet combined with vehicle (MA2) or zoledronate (ZOL); [4] Sheep had an ovariectomy and were fed an MA diet for a year, followed by a year of the MA diet and vehicle (MA3+OVX) or parathyroid hormone (PTH). Control, MA1, RAL and ALN were euthanized after 12 months, MA2 and ZOL at 14 months and MA3+OVX and PTH at 24 months.

	n	Month																							
		1	2	3	4	5	6	7	8	9	10	11	12	13	14	15	16	17	18	19	20	21	22	23	24
Control	6	Normal Diet																							
MA1	3	MA Diet						MA + Vehicle																	
RAL	2	MA Diet						MA + Raloxifene																	
ALN	2	MA Diet						MA + Alendronate																	
MA2	6	MA Diet								MA + Vehicle															
ZOL	6	MA Diet								MA + Zoledronate															
MA3+OVX	6	MA Diet + OVX												MA + OVX + Vehicle											
PTH	6	MA Diet + OVX												MA + OVX + PTH											

A fourth set of skeletally mature sheep were fed an MA diet for one year after ovariectomy, which has been shown to induce osteopenia⁽³²⁾. The sheep were then maintained on the MA diet and were administered teriparatide (PTH, n=6) or vehicle (MA3+OVX, n=6) for one year. Treatment was administered daily via subcutaneous injection (5 mcg/kg). All animal procedures were reviewed and approved by the University of Minnesota IACUC and the Hospital for Special Surgery IACUC.

3.2.2 Sample Preparation

Sheep were euthanized at the end of the specified treatment period. Femurs were removed and stored at -20°C in saline-soaked gauze until the time of sample preparation. Beams were cut out of the medial diaphysis of the femurs using a low speed diamond saw (Buehler Isomet; Lake Bluff, IL, USA). Beams were then polished using 15, 5 and 1 micron lapping films with ethylene glycol used as a lubricant to prevent mineral leaching^(33,34). Samples were polished to a final size of 2 x 2 x 25 mm. After polishing, samples were stored at -20°C in hydroxyapatite-buffered saline-soaked gauze until testing.

3.2.3 Fatigue Testing

Beams were tested in four-point bending fatigue^(35,36) (Bose Electroforce LM-1, Eden Prairie, Minnesota, USA). The bottom supports were placed 20 mm apart, and the top loading points placed 5 mm apart (Figure 3.2). These positions created a constant bending moment between the loading points and limited the effects of crushing at the load points⁽³⁷⁾. Preconditioning was completed by 20 cycles of loading from 2 to 20 N. These values were chosen through preliminary testing that demonstrated that these loads induced normal surface strains below the 2500 $\mu\epsilon$ necessary to create microdamage and alter fatigue life⁽¹⁰⁾. The initial flexural modulus was measured from the 10th cycle and calculated using the assumptions of linear elastic beam theory. Initial modulus values were used to calculate the force necessary to achieve desired values of strain of 400 to 4000 $\mu\epsilon$ on the tensile and compressive surfaces. Samples were loaded in force control from 400 to 4000 $\mu\epsilon$ ($R=0.1$) to failure with peak-to-peak force and displacement measured at each cycle. Cycles-to-failure, N_f , was defined as the number of cycles experienced before the sample broke. Modulus loss at failure was defined as the

percent change in modulus from the 10th cycle to N_f , and was calculated with linear elastic beam theory⁽³⁸⁾. All testing was completed at physiologic temperature (37°C) in hydroxyapatite-buffered PBS (1g HA added per 1L PBS and allowed to sit overnight until solution was supersaturated) with temperature monitored continuously.

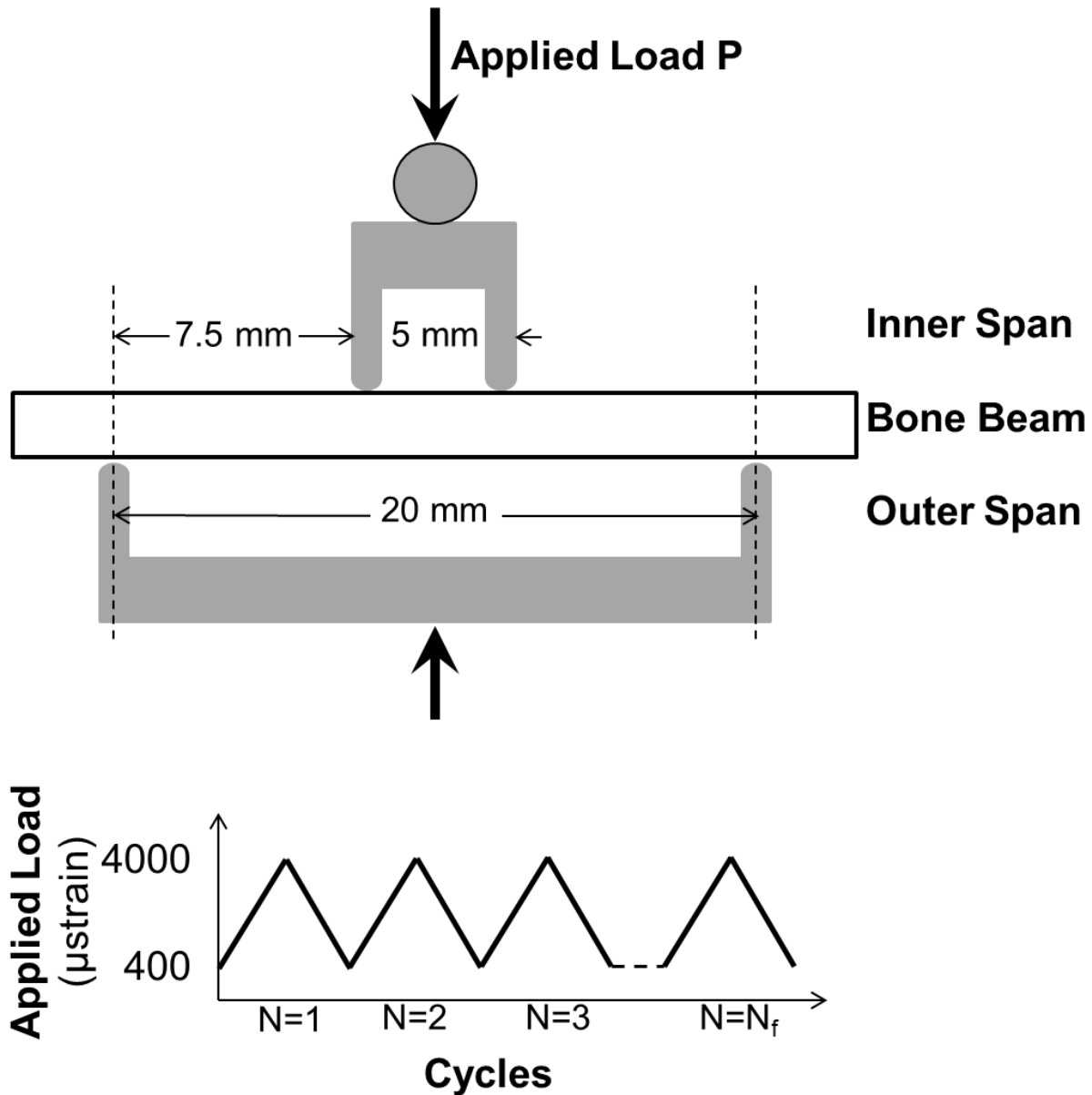


Figure 3.2: Set up for four point bending fatigue loading. P = applied load. The span between the inner supports was 5 mm, and for the outer supports 20 mm. A cyclic load was applied to failure with strain levels between 400 and 4000 μ strain.

3.2.4 Microcomputed Tomography (microCT)

Tissue mineral density (TMD) was measured with microCT at a 50 micron voxel size (eXplore CT 120, GE Healthcare, Waukesha, WI, USA). A mineral phantom was used for calibration with analysis completed in Microview (version ABA 2.2, GE Healthcare, Waukesha, WI, USA).

3.2.5 Statistical Analysis

The purpose of the experiment was to determine differences in N_f among the different treatment groups and correlate the differences to TMD data. A standard least squares analysis was used to compare each group to the grand mean of the data. The four separate experiments limited the ability to compare data across experiments. A log transform was performed on the cycles-to-failure data to meet the assumption of equal variance between groups.

Different treatments and durations of MA controls can influence the results. Low sample sizes also limited comparisons among groups. For comparison of the MA1, raloxifene and alendronate groups, a Students t-test was used to compare each group with a Bonferroni post hoc correction applied. A Students t-test was completed also for the MA2 and zoledronate data, MA3+OVX data and PTH. The Bonferroni correction and t-test comparisons were necessary due to low sample sizes and not meeting the assumptions for an ANOVA.

3.3 Results

An increase in the initial flexural modulus was seen in the MA3+OVX and PTH groups as compared to the grand mean of all groups (Figure 3.3).

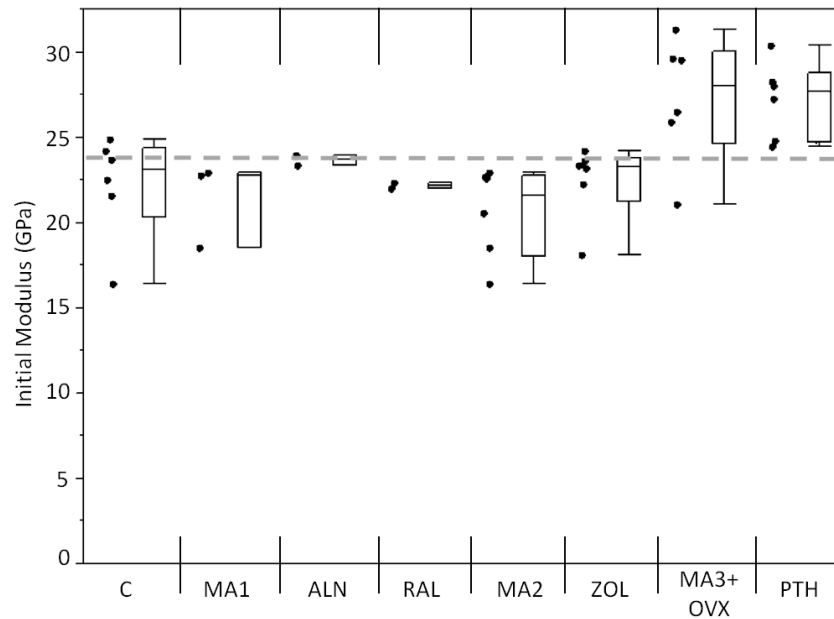


Figure 3.3: Initial modulus values for each group. MA3+OVX and PTH had higher initial moduli than the other groups. Markers to the left represent individual sample data points. Box and whisker plots on right show the minimum, maximum, mean, and 25th and 75th quartiles for each group. Dashed line is the grand mean.

Samples treated with alendronate had a significantly lower N_f compared to the grand mean of all groups ($p < 0.01$), while PTH samples had significantly greater N_f compared to the grand mean ($p < 0.01$; Figure 3.4).

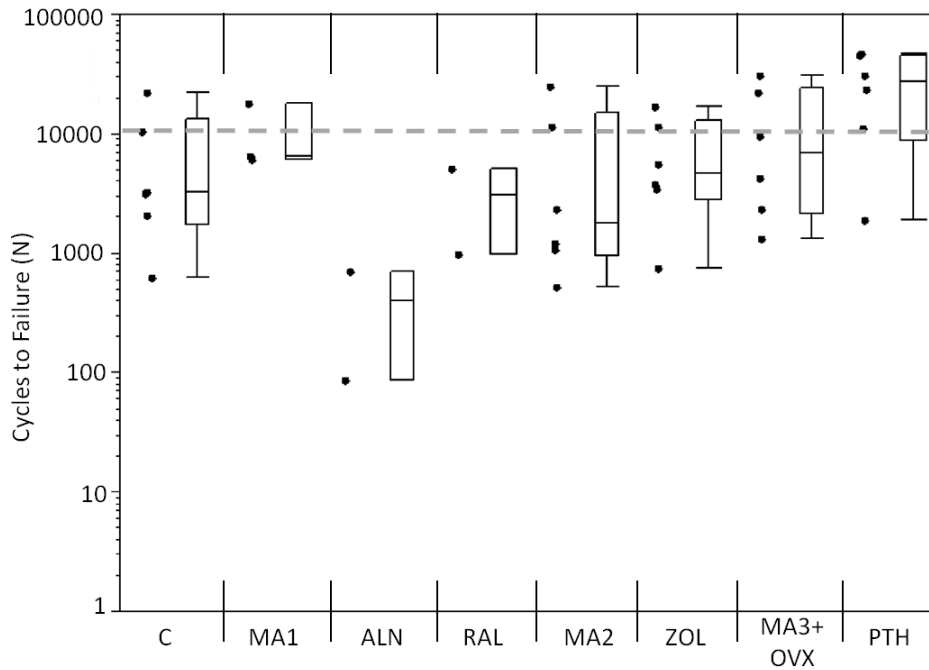


Figure 3.4: Cycles to failure for each group. Alendronate (ALN) had fewer cycles to failure compared to the grand mean ($p < 0.01$). Teriparatide (PTH) had more cycles to failure compared to the grand mean ($p < 0.01$). Markers to the left represent individual sample data points. Box and whisker plots on the right show the minimum, maximum, mean, and 25th and 75th quartiles. Dashed line represents the grand mean.

A loss of fatigue life occurred between alendronate (ALN) and its metabolic acidosis control (MA1; $p < 0.01$). Modulus loss at failure was significantly lower in the alendronate-treated groups compared to the grand mean ($p < 0.05$; Figure 3.5).

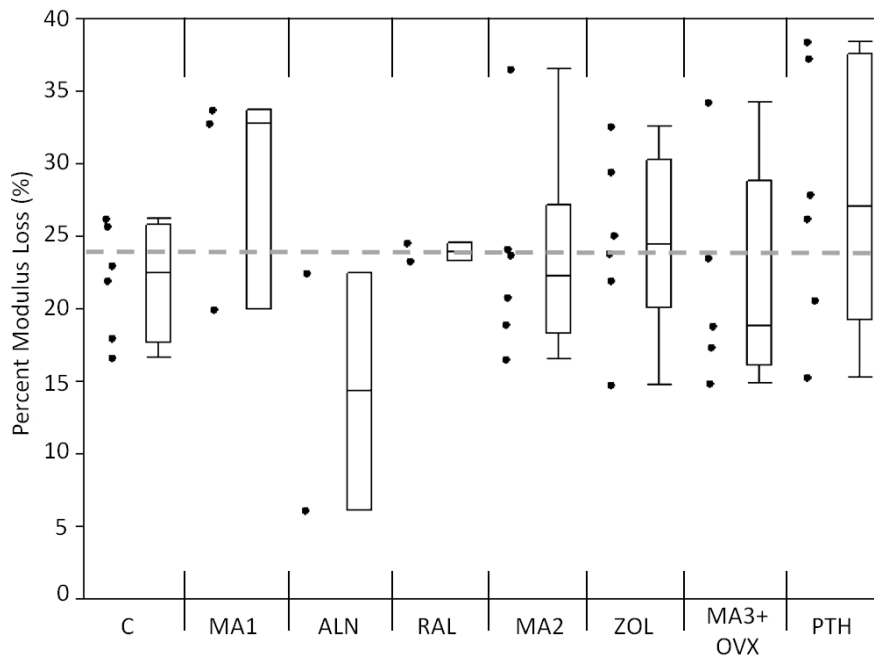


Figure 3.5: Modulus loss at failure for each group. Alendronate had a lower modulus loss at failure compared to the grand mean ($p < 0.05$). Markers to the left represent individual sample data points. Box and whisker plots on the right show the minimum, maximum, mean, and 25th and 75th quartiles. Dashed line represents the grand mean.

Mineralization measures (TMD) did not account for the differences in fatigue behavior.

Control samples had a lower TMD compared to the grand mean, while raloxifene raised the TMD above the grand mean ($p < 0.05$; Figure 3.6).

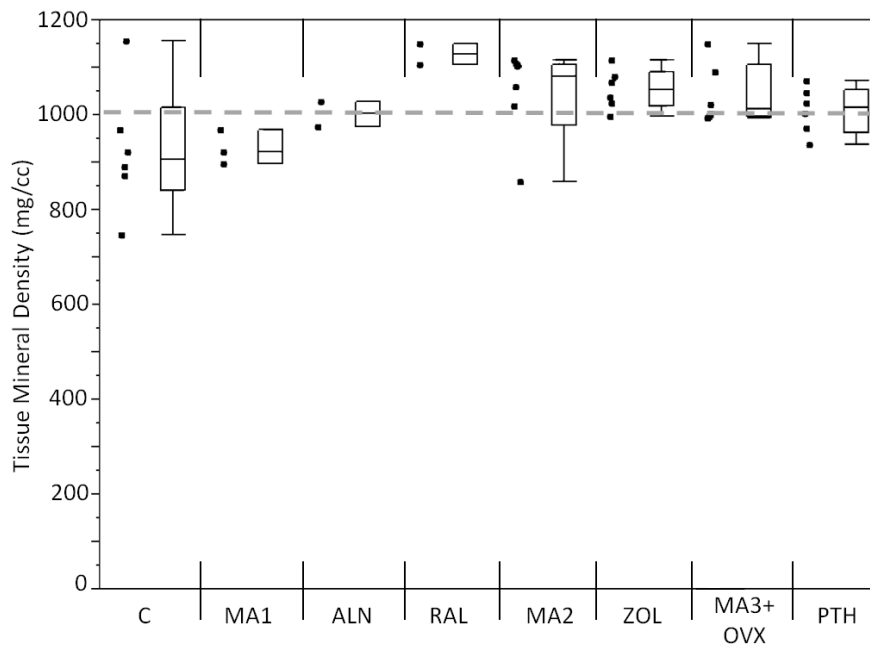


Figure 3.6: Mineralization measure for each group. Control samples had a lower TMD as compared to the grand mean while raloxifene samples had increased TMD as compared to the grand mean ($p < 0.05$). Markers to the left represent individual sample data points. Box and whisker plots on the right show the minimum, maximum, mean, and 25th and 75th quartiles. Dashed line represents the grand mean.

3.4 Discussion and Conclusions

Fatigue properties were examined in cortical bone tissue from sheep treated by anti-resorptive drugs after induction of osteoporosis. Four-point bending fatigue testing to failure was completed at physiologic temperature on bone beams created from the femoral diaphysis.

Osteoporosis treatments had differing effects on the fatigue life of cortical bone tissue.

Alendronate treatment caused a significant loss in fatigue life as compared to the grand mean and its MA control; however, zoledronate-treated specimens did not experience any change in fatigue life from the grand mean or MA control. Greater changes might be expected with zoledronate than alendronate given zoledronate's greater binding affinity and potency⁽³⁹⁾. Alendronate has a relative potency of $1-2 \times 10^3$, whereas zoledronate has a relative potency of 10^4 compared to

etidronate⁽⁴⁰⁾. Raloxifene did not change the fatigue life of the tissue while PTH increased fatigue life over the grand mean of the data. Differences in the fatigue life indicate material property changes caused by binding affinity, dosing, chemical structure or collagen changes.

Differences in the administration of the bisphosphonates may contribute to the altered fatigue properties. Alendronate was administered daily via cannula while zoledronate was given once over the course of the experiment via intravenous injection following clinical dosing regimens^(30,31). With daily dosing of alendronate the bisphosphonate is present in the serum continuously affecting biomarkers of bone turnover, whereas a single dose of zoledronate may allow the serum biomarker levels to return to pre-treatment homeostasis. Serum CTX is known to be reduced with bisphosphonate dosing and increase with time since last administration^(41,42). Increased collagen maturity occurs with bisphosphonate treatment, and suppression of serum biomarkers such as CTX may indicate differences between the two bisphosphonate types.

Bisphosphonate molecular structure and distribution throughout the tissue are also theorized to have an effect on the tissue properties. Regions of higher mineralization were surface-based on trabeculae with zoledronate treatment⁽²⁸⁾, which supports the idea that zoledronate has a more surface-based effect. Distribution of bisphosphonates throughout cortical bone tissue has only been reported with the use of ibandronate and differences in distribution between proximal and distal cortices were noted⁽⁴³⁾. Higher-affinity bisphosphonates have less diffusion into the bone, which could cause differences between alendronate and zoledronate⁽⁴⁴⁾.

Alendronate-treated samples had lower modulus loss at failure indicating a more brittle material. Microdamage quantities in these samples were not analyzed, so differences in this parameter among groups are unknown. Microdamage is associated with fatigue loading, and increased microdamage is correlated to loss of modulus in trabecular bone⁽⁴⁵⁾. Greater

microdamage created by activities of daily living occurs in both cortical and cancellous tissues with alendronate treatment compared to untreated control tissues^(14,16).

In this study, applied loads created maximum normal strains from 400 to 4000 $\mu\epsilon$. In laboratory fatigue conditions in bending, damage creation starts at 2500 $\mu\epsilon$ in regions under tension; however, greater than 4000 $\mu\epsilon$ is necessary in the regions under compression⁽¹⁰⁾. The 4000 $\mu\epsilon$ applied in our study would, therefore, create damage in the tensile region with the compressive region receiving little damage. Greater damage in the tensile region is similar to AFF progression, in which the stress fracture develops from the lateral cortex that is under tension during normal weight-bearing activities.

Results of this study are limited by several factors including the underpowered sample sizes for both alendronate and raloxifene treatments. As previously stated, small sample sizes were unplanned and due to factors beyond our control in the experiment; however, recent studies in a different animal model have also demonstrated a reduction in fatigue life with alendronate treatment⁽¹⁹⁾. The lack of fatigue life change with raloxifene treatment may indicate fatigue life preservation; however, this result may be due to lack of power from a small sample size. SERM therapies also have the side effect of increased risk of thromboembolic problems⁽⁴⁶⁾ indicating that an increased fatigue life alone may not make this therapy more appropriate. Four-point bending fatigue is not a typical method for fatigue measurements. Tensile and compressive fatigue are more commonly used for material characterization^(10,11); however, limited tissue from repurposed samples prevented the possibility of analyzing tissues by this method. Finally, although having samples from four separate studies enhanced our ability to make comparisons, this situation was less than ideal as sheep are known to experience seasonal differences in

BMD⁽⁴⁷⁾. Nevertheless, we did include untreated control samples to compare with treatment group samples.

In this study fatigue life differences with osteoporosis treatments depended on both the class of treatment, type of drug, and mode of delivery. Alendronate caused a reduction in bone tissue fatigue life while PTH caused an increase in fatigue life. Raloxifene and zoledronate did not change fatigue life. Material property alterations may be due to differences in chemical structure, mechanisms of actions of these drugs, or dosing regimens by which the drugs are administered. Under the confines of this study, drug uptake or the effect of dosing regimen were not possible to examine; however, these variables are avenues for future research that may help explain the occurrence of AFF.

3.5 References:

1. Burge R, Dawson-Hughes B, Solomon DH, Wong JB, King A, Tosteson A. Incidence and Economic Burden of Osteoporosis-Related Fractures in the United States, 2005–2025. *J. Bone Miner. Res.* 2007;22(3):465–75.
2. Cummings SR, Karpf DB, Harris F, Genant HK, Ensrud K, LaCroix AZ, Black DM. Improvement in spine bone density and reduction in risk of vertebral fractures during treatment with antiresorptive drugs. *Am. J. Med.* 2002 Mar;112:281–9.
3. Liberman UA, Weiss SR, Broll J, Minne HW, Quan H, Bell NH, Rodriguez-portales JA, Downs RW, Dequeker J, Favus MJ, Seeman E, Recker RR, Capizzi T, Santora AC, Lombardi A, Shah R V., Hirsch LJ, Karpf DB. Effect of Oral Alendronate on Bone Mineral Density and the Incidence of Fractures in Postmenopausal Osteoporosis. *N. Engl. J. Med.* 1995;333(22):1437–43.
4. Allen MR, Burr DB. Bisphosphonate effects on bone turnover, microdamage, and mechanical properties: what we think we know and what we know that we don't know. *Bone.* Elsevier Inc.; 2011 Jul;49(1):56–65.
5. Taylor D, Hazenberg JG, Lee TC. Living with cracks: damage and repair in human bone. *Nat. Mater.* 2007 Apr;6(4):263–8.

6. Donnelly E, Meredith DS, Nguyen JT, Gladnick BP, Rebolledo BJ, Shaffer AD, Lorich DG, Lane JM, Boskey AL. Reduced cortical bone compositional heterogeneity with bisphosphonate treatment in postmenopausal women with intertrochanteric and subtrochanteric fractures. *J. bone Miner. Res.* 2012 Mar;27(3):672–8.
7. Bala Y, Depalle B, Farlay D, Douillard T, Meille S, Follet H, Chapurlat R, Chevalier J, Boivin G. Bone micromechanical properties are compromised during long-term alendronate therapy independently of mineralization. *J. bone Miner. Res.* 2012 Apr;27(4):825–34.
8. Paschalis EP, Mendelsohn R, Boskey AL. Infrared assessment of bone quality: a review. *Clin. Orthop. Relat. Res.* 2011 Aug;469(8):2170–8.
9. Roschger P, Paschalis EP, Fratzl P, Klaushofer K. Bone mineralization density distribution in health and disease. *Bone.* 2008 Mar;42(3):456–66.
10. Pattin CA, Caler WE, Carter DR. Cyclic mechanical property degradation during fatigue loading of cortical bone. *J. Biomech.* 1996 Jan;29(1):69–79.
11. Carter DR, Hayes WC. Fatigue life of compact bone-I: Effects of stress amplitude, temperature and density. *J. Biomech.* 1976 Jan;9(1):27–34.
12. Carter DR, Hayes WC, Schurman DJ. Fatigue life of compact bone-II. Effects of microstructure and density. *J. Biomech. Eng.* 1976;9:211–8.
13. Reszka AA, Rodan GA. Bisphosphonate mechanism of action. *Curr. Rheumatol. Rep.* 2003 Feb;5(1):65–74.
14. Mashiba T, Hirano T, Turner CH, Forwood MR, Johnston CC, Burr DB. Suppressed bone turnover by bisphosphonates increases microdamage accumulation and reduces some biomechanical properties in dog rib. *J. Bone Miner. Res.* 2000 Apr;15(4):613–20.
15. Yamagami Y, Mashiba T, Iwata K, Tanaka M, Nozaki K, Yamamoto T. Effects of minodronic acid and alendronate on bone remodeling, microdamage accumulation, degree of mineralization and bone mechanical properties in ovariectomized cynomolgus monkeys. *Bone.* Elsevier Inc.; 2013 May;54(1):1–7.
16. Mashiba T, Turner CH, Hirano T, Forwood MR, Johnston CC, Burr DB. Effects of suppressed bone turnover by bisphosphonates on microdamage accumulation and biomechanical properties in clinically relevant skeletal sites in beagles. *Bone.* 2001 May;28(5):524–31.
17. Allen MR, Burr DB. Mineralization , Microdamage , and Matrix : How Bisphosphonates Influence Material Properties of Bone. *BoneKEy-Osteovision.* 2007;4(2):49–60.

18. Gourion-Arsiquaud S, Allen MR, Burr DB, Vashishth D, Tang SY, Boskey AL. Bisphosphonate treatment modifies canine bone mineral and matrix properties and their heterogeneity. *Bone*. Elsevier Inc.; 2010 Mar;46(3):666–72.
19. Bajaj D, Geissler JR, Allen MR, Burr DB, Fritton JC. The resistance of cortical bone tissue to failure under cyclic loading is reduced with alendronate. *Bone*. Elsevier Inc.; 2014 Apr 1;64:57–64.
20. Isaacs JD, Shidiak L, Harris IA, Szomor ZL. Femoral insufficiency fractures associated with prolonged bisphosphonate therapy. *Clin. Orthop. Relat. Res.* 2010 Dec;468(12):3384–92.
21. Schilcher J, Michaelsson K, Aspenberg P. Bisphosphonate Use and Atypical Fractures of the Femoral Shaft. *N. Engl. J. Med.* 2011;364(18):1728–37.
22. Lo JC, Huang SY, Lee G a, Khandelwal S, Khandewal S, Provus J, Ettinger B, Gonzalez JR, Hui RL, Grimsrud CD. Clinical correlates of atypical femoral fracture. *Bone*. Elsevier Inc.; 2012 Jul;51(1):181–4.
23. Shane E, Burr D, Ebeling PR, Abrahamsen B, Adler R a, Brown TD, Cheung AM, Cosman F, Curtis JR, Dell R, Dempster D, Einhorn T a, Genant HK, Geusens P, Klaushofer K, Koval K, Lane JM, McKiernan F, McKinney R, Ng A, Nieves J, O’Keefe R, Papapoulos S, Sen HT, van der Meulen MCH, Weinstein RS, Whyte M. Atypical subtrochanteric and diaphyseal femoral fractures: report of a task force of the American Society for Bone and Mineral Research. *J. Bone Miner. Res.* 2010 Nov;25(11):2267–94.
24. Shane E, Burr D, Abrahamsen B, Adler R a, Brown TD, Cheung AM, Cosman F, Curtis JR, Dell R, Dempster DW, Ebeling PR, Einhorn T a, Genant HK, Geusens P, Klaushofer K, Lane JM, McKiernan F, McKinney R, Ng A, Nieves J, O’Keefe R, Papapoulos S, Howe T Sen, van der Meulen MC, Weinstein RS, Whyte MP. Atypical subtrochanteric and diaphyseal femoral fractures: second report of a task force of the american society for bone and mineral research. *J. Bone Miner. Res.* 2014 Jan;29(1):1–23.
25. Ettinger B, Black DM, Mitlak BH, Knickerbocker RK, Nickelsen T, Genant HK, Christiansen C, Stakkestad J, Glu CC, Krueger K, Cohen FJ, Eckert S, Avioli L V. Reduction of Vertebral Fracture Risk in Postmenopausal Women with Osteoporosis Treated with Raloxifene Results From a 3-Year Randomized Clinical Trial. *J. Am. Ceram. Soc.* 1999;282(7):637–45.
26. Rey JRC, Cervino EV, Rentero ML, Crespo EC, Alvaro AO, Casillas M. Raloxifene: mechanism of action, effects on bone tissue, and applicability in clinical traumatology practice. *Open Orthop. J.* 2009 Jan;3:14–21.

27. Chiang CY, Zebaze RMD, Ghasem-Zadeh A, Iuliano-Burns S, Hardidge A, Seeman E. Teriparatide improves bone quality and healing of atypical femoral fractures associated with bisphosphonate therapy. *Bone*. Elsevier B.V.; 2013 Jan;52(1):360–5.
28. Burket JC, Brooks DJ, MacLeay JM, Baker SP, Boskey AL, van der Meulen MCH. Variations in nanomechanical properties and tissue composition within trabeculae from an ovine model of osteoporosis and treatment. *Bone*. Elsevier Inc.; 2013 Jan;52(1):326–36.
29. MacLeay JM, Olson JD, Enns RM, Les CM, Toth CA, Wheeler DL, Turner AS. Dietary-induced metabolic acidosis decreases bone mineral density in mature ovariectomized ewes. *Calcif. Tissue Int.* 2004 Nov;75:431–7.
30. Bone HG, Adami S, Rizoli R, Favus M, Ross PD, Santora A, Prahalada S, Daifotis A, Orloff J, Yates J. Weekly Administration of Alendronate: Rationale and Plan for Clinical Assessment. *Clin. Ther.* 2000;22(1):15–28.
31. Black DM, Delmas PD, Eastell R, Reid IR, Boonen S, Cauley JA, Cosman F, Lakatos P, Leung PC, Man Z, Mautalen C, Mesenbrink P, Hu H, Caminis J, Tong K, Rosario-jansen T, Krasnow J, Hue TF, Sellmeyer D, Eriksen EF, Sc DM, Cummings SR. Once-Yearly Zoledronic Acid for Treatment of Postmenopausal Osteoporosis. *N. Engl. J. Med.* 2007;356(18):1809–22.
32. Macleay JM, Olson JD, Turner AS. Effect of dietary-induced metabolic acidosis and ovariectomy on bone mineral density and markers of bone turnover. *J. Bone Miner. Metab.* 2004 Jan;22(6):561–8.
33. Donnelly E, Baker SP, Boskey AL, van der Meulen MCH. Effects of surface roughness and maximum load on the mechanical properties of cancellous bone measured by nanoindentation. *J. Biomed. Mater. Res.* 2006 May;77A(2):426–35.
34. Brock GR, Kim G, Ingraffea AR, Andrews JC, Pianetta P, van der Meulen MCH. Nanoscale examination of microdamage in sheep cortical bone using synchrotron radiation transmission x-ray microscopy. *PLoS One.* 2013 Jan;8(3):e57942.
35. Boyce TM, Fyhrie DP, Glotkowski MC, Radin EL, Schaffler MB. Damage type and strain mode associations in human compact bone bending fatigue. *J. Orthop. Res.* 1998 May;16(3):322–9.
36. Diab T, Vashishth D. Effects of damage morphology on cortical bone fragility. *Bone.* 2005 Jul;37(1):96–102.
37. Zhai T, Xu YG, Martin JW, Wilkinson AJ, Briggs GAD. A self-aligning four-point bend testing rig and sample geometry effect in four-point bend fatigue. *Int. J. Fatigue.* 1999;21:889–94.

38. Beer FP, Johnston ER, DeWolf JT. *Mechanics of Materials*. 4th ed. New York, NY: McGraw Hill; 1996. p. 308–63.
39. Russell RGG, Watts NB, Ebtino FH, Rogers MJ. Mechanisms of action of bisphosphonates: similarities and differences and their potential influence on clinical efficacy. *Osteoporos. Int.* 2008 Jun;19(6):733–59.
40. Shaw NJ, Bishop NJ. Bisphosphonate treatment of bone disease. *Arch. Dis. Child.* 2005 May;90(5):494–9.
41. Rosen HN, Moses AC, Garber J, Iloputaife ID, Ross DS, Lee SL, Greenspan SL. Serum CTX: a new marker of bone resorption that shows treatment effect more often than other markers because of low coefficient of variability and large changes with bisphosphonate therapy. *Calcif. Tissue Int.* 2000 Feb;66(2):100–3.
42. Marx RE, Cillo JE, Ulloa JJ. Oral bisphosphonate-induced osteonecrosis: risk factors, prediction of risk using serum CTX testing, prevention, and treatment. *J. Oral Maxillofac. Surg.* 2007 Dec;65(12):2397–410.
43. Smith SY, Recker RR, Hannan M, Müller R, Bauss F. Intermittent intravenous administration of the bisphosphonate ibandronate prevents bone loss and maintains bone strength and quality in ovariectomized cynomolgus monkeys. *Bone.* 2003 Jan;32(1):45–55.
44. Nancollas GH, Tang R, Phipps RJ, Henneman Z, Gulde S, Wu W, Mangood a, Russell RGG, Ebtino FH. Novel insights into actions of bisphosphonates on bone: differences in interactions with hydroxyapatite. *Bone.* 2006 May;38(5):617–27.
45. Lambers FM, Bouman AR, Rimnac CM, Hernandez CJ. Microdamage caused by fatigue loading in human cancellous bone: relationship to reductions in bone biomechanical performance. *PLoS One.* 2013 Jan;8(12):e83662.
46. Gennari L, Merlotti D, Valleggi F, Martini G, Nuti R. Selective estrogen receptor modulators for postmenopausal osteoporosis: current state of development. *Drugs Aging.* 2007 Jan;24(5):361–79.
47. Arens D, Sigrist I, Alini M, Schawalder P, Schneider E, Egermann M. Seasonal changes in bone metabolism in sheep. *Vet. J.* 2007 Nov;174(3):585–91.

Chapter 4

Nanoscale Examination of Microdamage in Sheep Cortical Bone Using Synchrotron Radiation Transmission X-Ray Microscopy¹

4.1 Introduction

Bone tissue has a load bearing hierarchical structure comprised of many levels [1] in which damage occurs through activities of daily living [2], reducing the strength, stiffness and energy dissipation of the whole bone [3]. This damage, referred to as microdamage, typically consists of small cracks or bone structure damage that are subsequently repaired through remodeling. Microdamage often occurs around lacunae, and the osteocytes within the lacunae are thought to signal the remodeling process when microcracks occur [4,5]. Examination of these mechanisms is difficult given that the majority of visualization techniques have resolutions that do not resolve the edges of lacunae and canaliculi. Current nanoscale methods only visualize damage on surfaces [6]. A method for microdamage visualization at the nanoscale with a larger depth of focus would be useful for further examining damage mechanisms and remodeling processes. Visualization of microdamage is typically accomplished through fluorochrome, basic fuchsin or x-ray negative staining [6-11]. With these staining techniques, microcracks are visualized as 2D discrete cracks, diffuse damage or cross-hatching. Discrete microcracks typically occur in interstitial bone and are larger than canaliculi but smaller than the vascular canals [12]. Diffuse damage is characterized as a large region of staining in which cracks may or may not be apparent at the scale of observation [13]. Cross-hatch microdamage involves patterned cracks occurring in the bone [14].

¹Reprinted from: Brock GR, Kim G, Ingraffea AR, Andrews JC, Pianetta P, van der Meulen MCH (2013) Nanoscale examination of microdamage in bone using synchrotron radiation transmission x-ray microscopy. PLoS One 8(3):e57942

Uranyl acetate and barium sulfate have been used as x-ray negative stains (i.e. with high x-ray absorption) for microdamage visualization in bone [6;15-18]. Microdamage visualization using these methods has been completed with SEM and micro-CT; however, limitations exist for the region viewed and the resolution. SEM can image at the nanoscale but is only able to visualize the surface material of a sample. Micro-CT typically uses voxel sizes of 10 μm or larger [15-18]. Methods have also been developed with stains such as gold nanoparticles [19] or terbium nanoparticles [20] to gain higher resolution and view damage at a smaller scale. Confocal microscopy has also been used on fluorochrome-stained slices to visualize microdamage in three dimensions [21].

Transmission X-Ray Microscopy (TXM) uses monochromatic hard x-rays from synchrotron radiation to create x-ray transmission and absorption images with a resolution of 30 nanometers [22]. Bone features, such as osteocyte lacunae and canalicular networks, are visible with TXM (Figure 4.1). Tomography can also be acquired on small volumes with nanoscale voxel sizes. Stains with strong x-ray absorption can be used to indicate damage by binding to damage present in bone. Differences in attenuation can indicate damage and differentiate stained microdamage from bone and its structures.

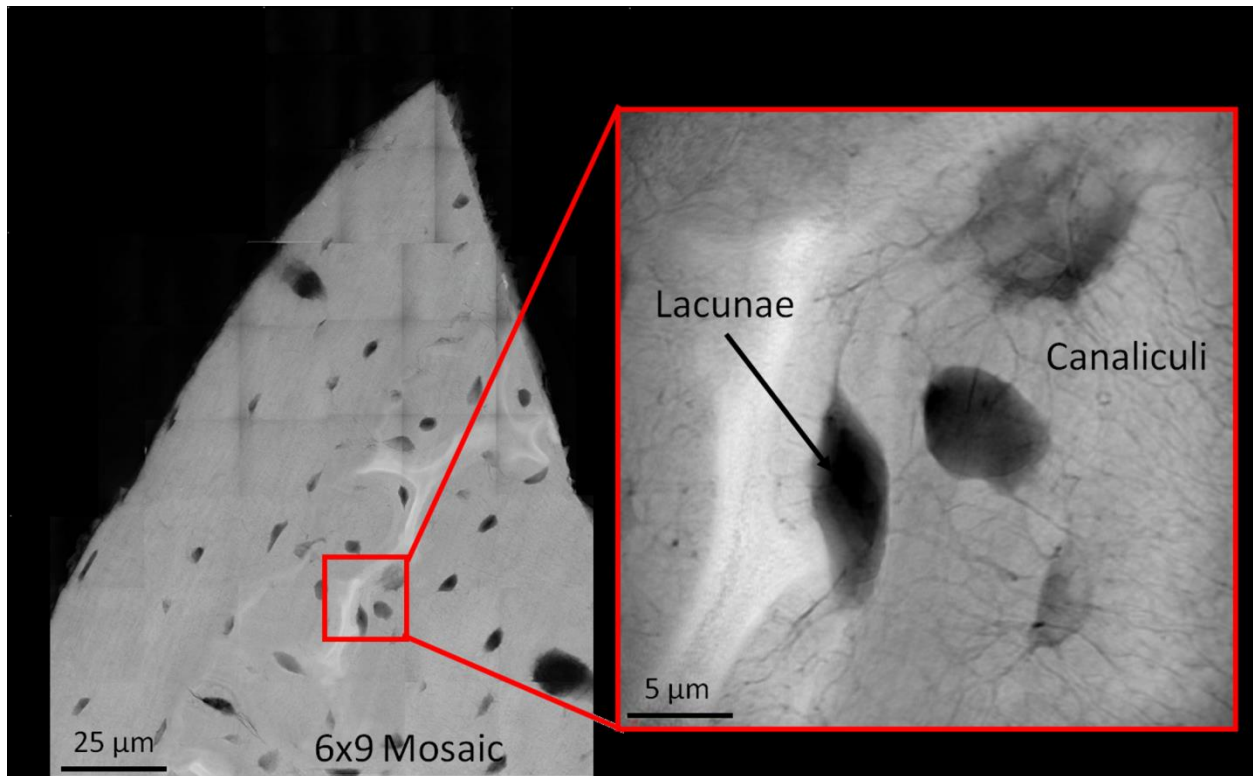


Figure 4.1: Representative TXM image: Representative TXM absorption contrast image (acquired at 7.1 keV) illustrating lacunae and canaliculi present in rat cortical bone (slices 50 microns thick) with grey areas indicating bone, and black areas indicating background, lacunae and canaliculi. Left figure, 6x9 mosaic of low resolution images; right figure, single high resolution image of region. No staining is present in this image; grey-scale variation represents attenuation differences in the tissue.

This paper describes a method for nanoscale visualization of microdamage in cortical bone tissue using x-ray negative staining and synchrotron-based x-ray imaging. After staining bone with lead-uranyl acetate, samples were imaged using TXM. Analysis of sections loaded in three- and four- point bending demonstrated the sensitivity of the method to detect differences between monotonic and fatigue loading. This method has many future applications for visualization of damage at the nanoscale, leading to increased knowledge about skeletal damage mechanisms.

4.2 Materials and Methods

Three sets of cortical bone beams with different applied loading were used to examine microdamage: (Set 1) intact beams loaded in three point bending, (Set 2) intact beams loaded in four point bending fatigue, and (Set 3) notched beams loaded in three point bending. For all beams, three millimeter wide sections of bone were removed from the cranial portion of the diaphysis of sheep femurs using a low speed diamond saw (Buehler Corp., Lake Bluff, IL). The femurs were obtained from skeletally mature sheep used in a study approved by the Colorado State University Institutional Animal Care and Use Committee. Sheep of this age have previously been shown to have mainly plexiform cortical bone [23]. Sections were then polished using a grinding wheel at 200 rpm using 15, 5 and 1 micron lapping films with ethylene glycol to a final dimension of 2x2x20 mm. Ethylene glycol was used to lubricate between the sample and lapping film to prevent mineral leaching [24].

Beams were loaded monotonically or in fatigue to produce different quantities of damage. The first set of beams (n=13) was loaded in three-point bending with a preload of 5 N to ensure contact with the sample followed by a 0.25 mm displacement (approx. equivalent to 135 MPa maximum normal stress, 7,500 $\mu\epsilon$ maximum normal strain). Monotonically loaded un-notched beams were used to examine whether microdamage from a single loading cycle could be viewed with TXM. The second set of beams (n=26) was loaded in four-point bending fatigue from 4.8 to 48 N (approx. equivalent to 10 to 90 MPa maximum normal stress, 555 to 5,000 $\mu\epsilon$ maximum normal strain) at 2Hz for 20,000 cycles. Beams were tested in hydroxyapatite buffered saline at room temperature. Fatigue loaded beams were used to examine microdamage formed through repetitive loading. The third set of beams (n=23) had a 200 micron deep notch applied to the center of the periosteal side using a razor blade. Samples were then loaded monotonically in three-point bending to a force of 25 N (approx. equivalent to 94 MPa maximum normal stress,

5,200 $\mu\epsilon$ maximum normal strain) such that the notched side was in tension. Notched samples were used to localize damage to a specific region to compare damage morphologies. The entire notch region was considered the tensile region and was not further subdivided, while the compressive region was the side opposite of the notch. Differing number of samples in each set was due to acquisition time with the TXM and limited availability of the instrument. Statistical comparisons accounted for these differences.

Previously established procedures for uranyl acetate staining with micro-CT and SEM were used to indicate microdamage after loading [6,16,25]. Bulk sections of length 5 mm were removed from the center of the beam and stained in a solution of equal parts 8% uranyl acetate in 70% acetone and 20% lead (II) acetate in 70% acetone for one week. After one week the samples were placed in a 1% ammonium sulfide in 70% acetone solution for one week with the solution changed at 3 days. Post staining, thick sections were removed and polished using a precision grinding wheel (Allied High Tech, Rancho Dominguez, CA) to approximately 50 micron thickness using 15, 5, and 1 micron lapping films with ethylene glycol as a lubricant. Sections of monotonically-loaded unnotched beams (Set 1) were created at the point of loading for samples in the region of highest loading in the transverse plane of the bone. Fatigue sections (Set 2) were taken from the center of the beam in the region of highest load and created in both the transverse and longitudinal planes of the bone. Sections of notched beams (Set 3) were taken longitudinally to view localized damage around the notch. This orientation was perpendicular to the direction examined in the unnotched samples and aligned with the axis of the osteons to better capture regions of damage with loading.

Samples were imaged at the Stanford Synchrotron Radiation Lightsource (Menlo Park, CA) using the Transmission X-ray Microscope (Beamline 6-2c, Xradia; Pleasanton, CA).

Absorption images were acquired with an energy of 7.1 keV (2048x2048 pixels, 10.4 nm (monotonic loading) or 13.98 nm (fatigue loading) pixel size, 1 sec exposure). Images were taken along the axis of loading in the compressive, tensile and neutral axis regions of the cortical bone beams. To characterize tissue morphology and staining, both low resolution and high resolution images were taken. Low resolution images used frame averaging of two images for each field of view. Neighboring images were stitched, aligned and smoothed to create larger mosaics (11x11 tiles) of each region [26]. High resolution images were taken in areas with microdamage by frame averaging 10 separate images of the same area to form a single image. Analysis to examine microdamage was then performed on the low resolution mosaics and high resolution.

Comparisons were made between monotonic and fatigue loaded unnotched specimens through damage quantification. Regions corresponding to tensile and compressive normal stresses were identified based on the continuum level loading applied to the beams. Staining was identified and quantified for these tensile and compressive regions. First, to threshold uranyl acetate from bone each pixel in every large mosaic was counted and binned using a histogram with a thousand bins (Matlab, Mathworks, Natick, MA). A triangle method was used to threshold the bone from the uranyl acetate [27]. This method involves representing the image data as a histogram with a Gaussian peak representing the attenuation of the bone and a higher attenuation tail representing uranyl acetate. Total counts for uranyl acetate and bone were then summed, and the lead-uranyl acetate counts were normalized by the total bone counts. Stain totals in monotonically loaded samples were compared to fatigue loaded samples using a Student's t-test (JMP, SAS, Cary NC). This comparison was only completed on images in the tensile and compressive regions. The lack of staining in the neutral axis region with monotonic loading

precluded statistical comparisons. Damage was expected at the neutral axis only in the fatigue samples, given the change in the position of the neutral axis as damage accumulates, because the modulus changes differently in the tensile and compressive regions.

To compare this new approach with a more established technique, notched sections were imaged by microcomputed tomography (micro-CT) prior to imaging with TXM. Sections were imaged at a 3.5 micron voxel size with micro-CT (Scanco Medical μ CT 35 system, Scanco Medical, Brüttisellen Switzerland). Images were thresholded to separate bone from background using a linear attenuation coefficient (μ , 1/cm) value of 2.5. The lead-uranyl acetate (UA) staining was then thresholded from the bone using an attenuation coefficient value of 6. Images were rotated such that an edge view was present, and the UA staining was overlaid to create a 2D micro-CT image similar to that of TXM. Corresponding TXM images of the same region were binned to match the voxel size used for micro-CT (MATLAB, Mathworks, Natick, MA). Thresholds were used to separate the background, bone and UA by placing the binned pixels into a histogram and fitting the peaks for background, bone and UA. Given the small field of view with TXM, no measures could be calculated with micro-CT; however, observations about damage morphology and distribution were drawn through image visualization and qualitative comparison.

4.3 Results

Unnotched samples from both monotonic and fatigue loading demonstrated the ability of TXM to image microdamage. Unnotched samples with a monotonic load (Set 1) had staining of bone structures. Staining was typically localized to areas of maximum stress and not present at the neutral axis. Staining was solely present in existing bone structures such as lacunae and canaliculi; no stain was evident in tissue outside of bone structures in either the tensile and

compressive regions. For samples with fatigue loading (Set 2) staining of the bone tissue was present in existing bone structures in all samples (26 of 26 samples imaged) and to new surfaces outside of bone structures in some samples (6 of 26 samples imaged). Repetitive loading increased the amount of stain present in the bone tissue compared to monotonic loading (Figure 4.2).

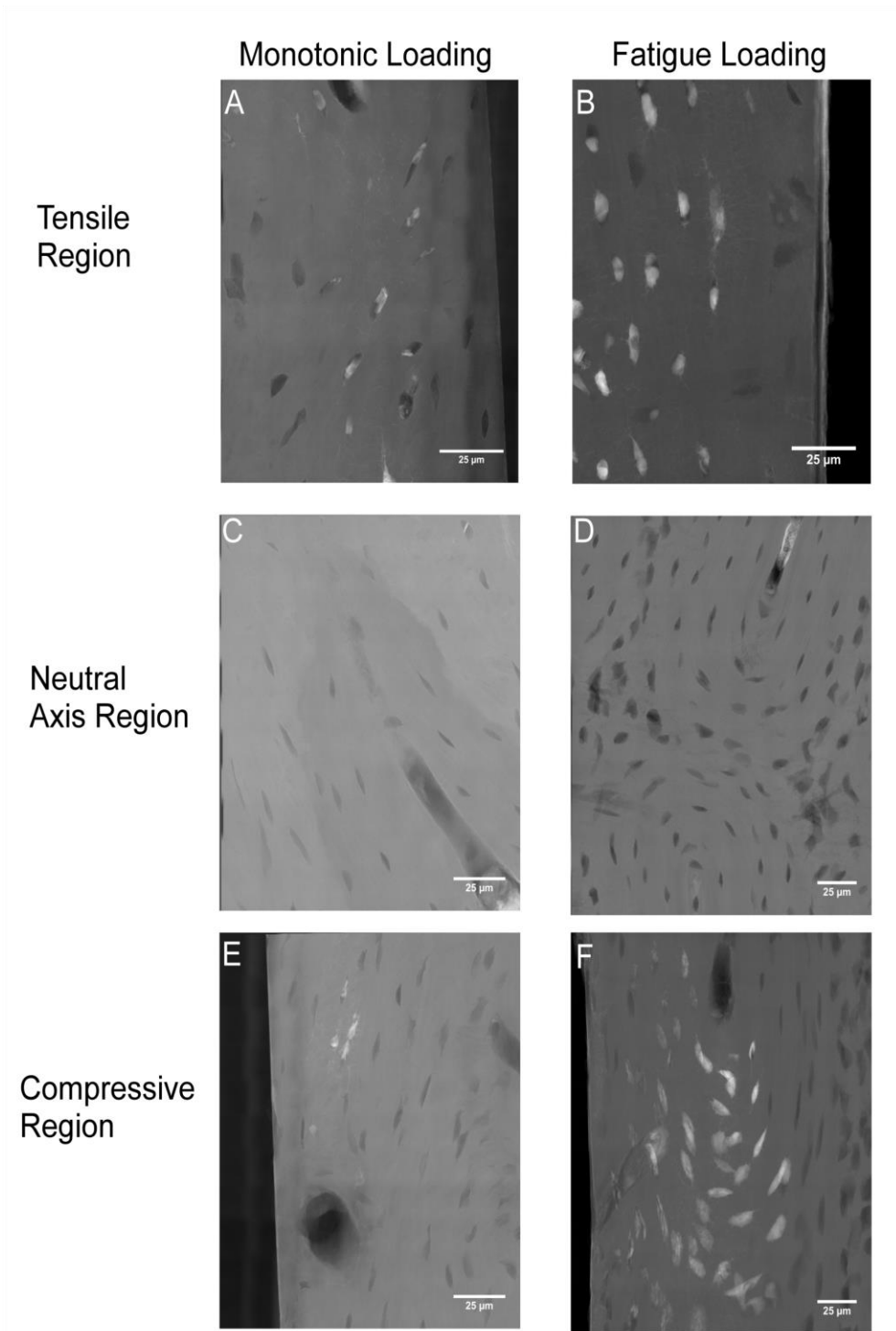


Figure 4.2: Monotonic and fatigue stain comparison: Staining of the tensile (A), neutral axis (C), and compressive (E) regions of monotonically loaded samples. Staining of the tensile (B), neutral axis (D), and compressive (F) regions of fatigue loaded samples. Images shown in transmission mode; white indicates high attenuating lead-uranyl acetate staining, grey indicates bone, and black indicates background. All scale bars are 25 microns.

The percent stained tissue area was greater ($p < 0.0001$) in the fatigue loaded sections as compared to the monotonically loaded sections (Figure 4.3). Greater stain presence in fatigue loaded sections illustrated that lead-uranyl acetate staining is an indicator of microdamage presence in bone, as more damage would be expected to occur in repetitively loaded tissue.

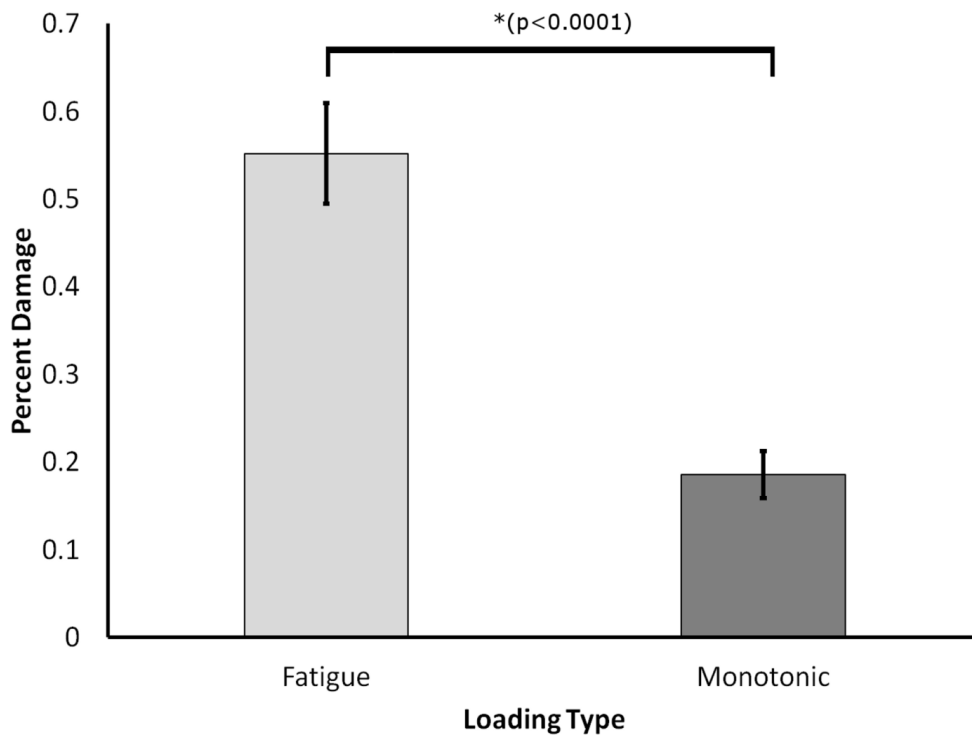


Figure 4.3: Increased stain uptake in fatigue loaded samples: Summary of total staining in images for cortical bone sections following fatigue and monotonic loading with both compressive and tensile regions pooled. Fatigue loading produced significantly more stain, indicating repeated loading creates greater damage formation allowing for increased uptake of the stain into bone tissue.

Microdamage in notched samples (Set 3) occurred in three forms: staining of existing bone features, cross-hatching damage, and discrete cracks. The most common form was staining of lacunae and canaliculi in the tensile and compressive regions (Figure 4.4 A, B; Figure 4.5). Cross-hatching microdamage occurred around the notch tip in 10 of 23 samples tested (Figure 4.4 C, D; Figure 4.5). Samples with cross-hatch damage occasionally also had stained bone

structures (lacunae and canaliculi) adjacent to the cross-hatching. A single sample had a crack propagating from the notch tip (Figure 4.4 E, F; Figure 4.5). No staining occurred in the neutral axis region in 22 of 23 notched samples (Figure 4.5).

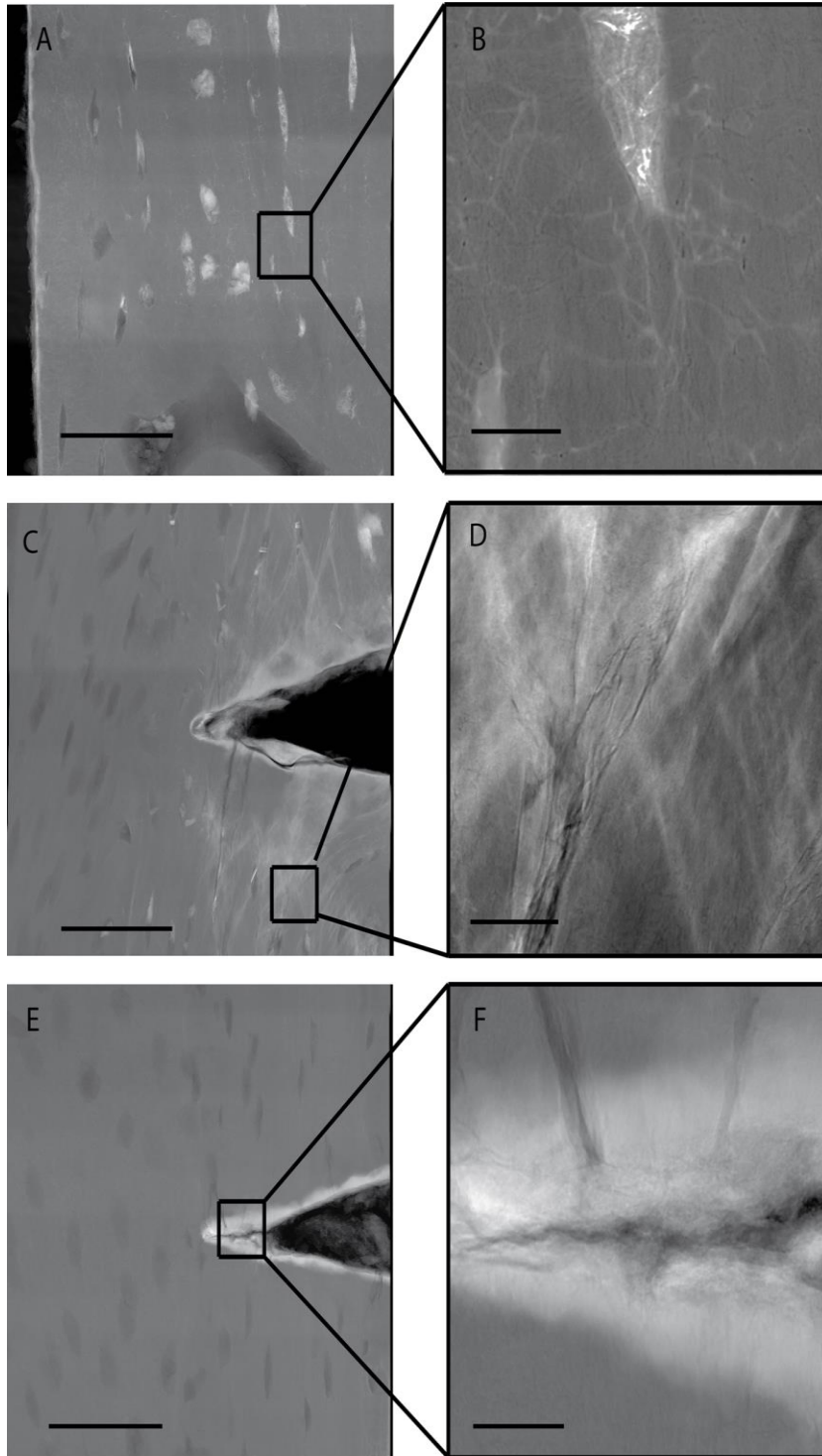


Figure 4.4: Different damage morphologies in notched samples: (A, B) Staining of lacunae and canaliculi in the compressive region seen in 20 of the 23 samples; (C, D) Cross hatching damage around notch tip in the tensile region observed in 10 of 23 samples; (E, F) Crack propagating from notch tip in the tensile region in a single sample. Staining appears white due to high

attenuation of lead-uranyl acetate, with bone tissue appearing grey and voids black. Scale bar: A,C,E = 50 μm ; B,D,F = 5 μm . Sample created in the longitudinal plane of the bone.

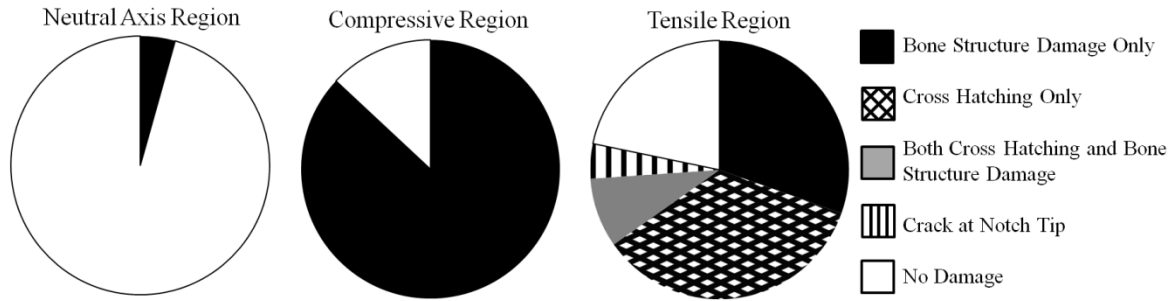


Figure 4.5: Summary of damage morphologies imaged in notched specimens: Summary of damage morphologies observed in the notched samples in each loading region (n=23 samples total). The majority of samples had staining of bone structures in the compressive region, and damage occurred at the neutral axis in only one sample. The tensile microdamage was mainly staining of bone structures or cross hatching in the notched samples with a single sample having a propagated crack. Damage in the unnotched samples consisted only of bone structure staining.

Differences in damage morphology were evident between micro-CT and TXM images. In the micro-CT reconstruction (Figure 4.6A) staining at the microscale appeared to cover a larger region of the sample due to partial volume effects of the x-ray negative stain. The micro-CT voxels were also larger than the bone structures, that were visible with TXM, and therefore micro-CT was not able to resolve the damage morphologies present in the bone tissue. Binning and thresholding of the TXM image to create pixels at the same scale as the micro-CT voxels (Figure 4.6B) reduced the stain area from micro-CT. Finally, the localized nature of the stain was evident in the full-scale, high resolution TXM image (Figure 4.6C).

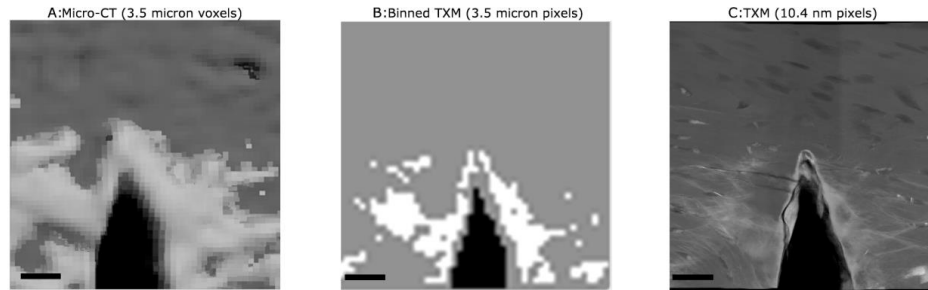


Figure 4.6: Comparison of TXM with micro-CT: Comparison of micro-CT with TXM images of notched cortical beam samples. In all images white areas indicate high attenuating lead uranyl acetate, grey represents bone and black represents background. First image, A, indicates micro-CT of staining, second, B, is of binned TXM to same pixel size as micro-CT and third, C, is of TXM. These images illustrate differences in damage morphology and partial volume effect that occur between micro-CT and TXM. Staining of bone structures and nanoscale damage is not visible using micro-CT; scalebar = 25 microns

4.4 Discussion and Conclusions

A method to examine microdamage with nanoscale resolution creating an x-ray projection image is presented using previously published staining techniques [6,16]. This method demonstrated nanoscale damage morphologies including staining of existing bone features, cross-hatching, and a discrete crack in a single specimen (Figure 4.4; Figure 4.5). Lead-uranyl acetate staining occurred in the regions of highest stress where damage would be expected and not in regions of low stress, indicating the lead-uranyl acetate was correlated with the higher stress regions where microdamage would be expected.

Previously microdamage was reported at the neutral axis of bone beams loaded in bending fatigue [13]. Here staining did not occur at the neutral axis of samples with monotonic loading but did occur in the fatigue loaded samples. UA is therefore able to move to the interior of a sample, which may reflect more transport paths in fatigue loaded sections allowing the stain to penetrate further into the interior of the sample. Prior studies have demonstrated different morphologies in compressive and tensile stress regions, with compressive regions having more

microcracks and tensile regions having more diffuse damage [13]. Results from this study showed similar morphologies of stained bone structures in both compressive and tensile regions. This difference may reflect that the bone structures visualized here are not visible with techniques used in prior studies. Limitations of the techniques and samples used should be noted for examining differences in the damage evident. Fatigue samples used in this study were loaded to a fixed number of cycles and may not have experienced equal degrees of stiffness loss, contributing to different damage formation. Prior studies focused on osteonal bone whereas plexiform cortical bone was used for this study. Damage in plexiform bovine cortical bone loaded in four point bending fatigue is dominated by viscoplastic creep [28], a limitation of the specimens and loading mechanisms used in this study. Comparisons of the percentage of stained tissue indicated a significantly greater area of staining in the fatigue-loaded samples. If transport of the stain into the bone had solely been by diffusion, differences would not have been present between the monotonic and fatigue loaded samples. Therefore, damage to the tissue must occur to create more paths for the stain to penetrate the tissue. This increased permeability was primarily through the existing lacunar-canalicular network.

Comparison with micro-CT (Figure 4.6) demonstrated differences in damage morphology and area. Partial volume effects and beam hardening will affect the damage imaged with micro-CT, with the stained region appearing larger than with TXM. Quantification and direct comparison between TXM and micro-CT was not possible due to the limited field of view of TXM. For the equivalent tissue area, micro-CT images contained 2,260 voxels total whereas TXM images contained 250 million pixels. Damage morphologies also appeared different at the different scales with binning and thresholding of the TXM image illustrating similarities between TXM and micro-CT. Damage viewed with micro-CT and x-ray negative stains may, therefore,

overestimate the damage regions when damage morphology is below the micro-CT resolution [15-18].

This study could not determine the mechanism of increased staining with fatigue loading. Uranyl acetate binds to phosphate groups in cell membranes [29]. The addition of the ammonium sulfide immobilizes the metal, blocking further penetration of the stain. The mechanism of the stain presence is believed to be a combination of binding to hydroxyapatite crystals and space filling within the bone structures. The additional staining in the fatigue loaded specimens likely reflects increased channels caused by damage to the tissue that permit the stain to penetrate further into the bone. Without this additional damage, the stain amounts would be similar for fatigue and monotonic loading, given that all samples were stained post-loading. The uranyl acetate staining may, therefore, be a transport-driven phenomenon, wherein more paths are created with increased loading.

Images viewed in this study differed from prior SEM studies in that samples were viewed as projections sampled through the thickness, rather than surface images [6]. SEM studies are unable to resolve damage more than a few microns below the surface of the sample. TXM allows damage to be viewed throughout a 50 micron thick section of the sample without sputtercoating of surfaces with gold or carbon. While not performed in this study, TXM also has the capability to create a tomography with 10 nm voxels for three dimensional nanoscale microdamage visualization and quantification on samples with depth and widths at or below 50 microns [22]. Lead-uranyl acetate staining has been used previously to create tomographic reconstructions of cancellous bone samples using micro-CT [16]. These tomographies had voxel sizes of 10 micrometers, in comparison to voxel sizes of 10.4 nanometers with TXM. Synchrotron micro-CT without staining has been used for three-dimensional visualization of microdamage and cracks in

human cancellous bone using a 1.4 micrometer linear voxel size [30]. Synchrotron radiation micro-CT has also been used to examine crack propagation in murine cortical bone with a 700 nm resolution [31]. TXM with lead-uranyl acetate stain has the potential to build on this knowledge by creating three-dimensional reconstructions of microdamage with 10nm voxels.

Studies in cortical bone demonstrated that damage will arrest at or move along cement lines or lamellae before moving through osteons [32-34]. Damage in the current study occurred in structures around and along lamella in the bone tissue, consistent with regions in which damage is typically observed at the microscale [35]. The low level of loading applied in the notched samples may account for only a single sample having a crack propagate from the notch. The damage observed may, therefore, be a precursor to larger discrete cracks. Diffuse damage in fatigue loaded, notched samples was believed to be damage to bone features during the early stages of the damage process; however, these features were not visible with fluorochrome staining and the image resolution used [36]. Resolution limits associated with confocal microscopy prevented the determination of whether microcracks penetrated lacunar walls in a study examining microdamage around osteocyte lacunae in tensile loaded cortical bone [4]. TXM visualized not only osteocyte lacunae, but also damage to the canaliculi, allowing for an understanding of the role of nanoscale bone structures in microdamage [22].

TXM for microdamage analysis has several important limitations. The sample must be no more than 50 microns thick and have a smooth surface. Therefore, sample preparation is time consuming and intensive. For tomographies, x-ray paths through the sample are limited to 50 microns for all vectors through the sample. Recent advances also allow for larger samples to be imaged using an extended depth of focus [37]. Viewing large areas requires stitching of individual images to create mosaics which are computationally intensive as well as time

consuming to acquire. Finally, even when images are combined, the total field of view with a mosaic is small, on the order of hundredths of a square millimeter. Given the small areas viewed, quantification of tissue properties and microdamage analysis may be difficult to generalize.

To our knowledge, TXM with lead-uranyl acetate staining is the first method to create a projection image of microdamage in bone at the nanoscale. Staining occurred primarily in bone structures in the lacunar canalicular network, not on new surfaces, regions below the resolutions of other microdamage imaging modalities. Nano-CT using synchrotron x-rays of damaged samples and examination of additional loading conditions will allow for a greater understanding of microdamage mechanisms and precursors.

4.5 References

1. Lakes R (1993) Materials with structural hierarchy. *Nature* 361:511-515.
2. Muir P, Johnson KA, Ruaux-Mason CP (1999) In Vivo Matrix Microdamage in a Naturally Occurring Canine Fatigue Fracture. *Bone* 25: 571–576.
3. Burr D (2003) Microdamage and bone strength. *Osteoporosis International*. 14 Suppl 5: S67–72.
4. Reilly GC (2000) Observations of microdamage around osteocyte lacunae in bone. *Journal of Biomechanics* 33: 1131–1134.
5. Herman BC, Cardoso L, Majeska RJ, Jepsen KJ, Schaffler MB (2010) Activation of bone remodeling after fatigue: differential response to linear microcracks and diffuse damage. *Bone* 47: 766–772.
6. Schaffler MB, Pitchford WC, Choi K, Riddle JM (1994) Examination of compact bone microdamage using back-scattered electron microscopy. *Bone* 15: 483–488.

7. Ebacher V, Wang R (2009) Materials Research Society Symposium Proc. Vol. 1187: 6–11.
8. Lee TC, Mohsin S, Taylor D, Parkesh R, Gunnlaugsson T, et al. (2003) Detecting microdamage in bone. *Journal of Anatomy* 203: 161–172.
9. O'Brien F, Taylor D, Lee TC (2003) Microcrack accumulation at different intervals during fatigue testing of compact bone. *Journal of Biomechanics* 36: 973–980.
10. Portero-Muzy NR, Chavassieux PM, Arlot ME, Chapurlat RD (2011) Staining procedure for the detection of microcracks: Application to ewe bone. *Bone* 49: 917–919.
11. Vashishth D, Koontz J, Qiu SJ, Lundin-Cannon D, Yeni YN, et al. (2000) In vivo diffuse damage in human vertebral trabecular bone. *Bone* 26: 147–152.
12. Burr DB, Stafford T (1990) Validity of the Bulk Staining Technique to Separate Artifactual from In Vivo Bone Microdamage. *Clinical Orthopaedics and Related Research* 260: 305-308.
13. Boyce TM, Fyhrie DP, Glotkowski MC, Radin EL, Schaffler MB (1998) Damage type and strain mode associations in human compact bone bending fatigue. *Journal of Orthopaedic Research* 16: 322–329.
14. Wenzel TE, Schaffler MB, Fyhrie, DP (1996) In vivo trabecular microcracks in human vertebral bone. *Bone*, 19: 88-95.
15. Leng H, Wang X, Ross RD, Niebur GL, Roeder RK (2008) Micro-computed tomography of fatigue microdamage in cortical bone using a barium sulfate contrast agent. *Journal of the Mechanical Behavior of Biomedical Materials* 1: 68–75.
16. Tang SY, Vashishth D (2007) A non-invasive in vitro technique for the three-dimensional quantification of microdamage in trabecular bone. *Bone* 40: 1259 - 1264.

17. Tang SY, Vashishth D (2010) Non-enzymatic glycation alters microdamage formation in human cancellous bone. *Bone* 46: 148–154.
18. Wang X, Masse DB, Leng H, Hess KP, Ross RD, et al. (2007) Detection of trabecular bone microdamage by micro computed tomography. *Journal of Biomechanics* 40: 397-403.
19. Zhang Z, Ross RD, Roeder RK (2010) Preparation of functionalized gold nanoparticles as a targeted X-ray contrast agent for damaged bone tissue. *Nanoscale* 2: 582–586.
20. McMahan BK, Mauer P, McCoy CP, Lee TC (2011) Luminescent Terbium Contrast Agent for Bone Microdamage Detection. *Australian Journal of Chemistry* 64: 600–603.
21. Fazzalari NL, Forwood MR, Manthey BA, Smith K, Kolesik P (1998) Three-dimensional confocal images of microdamage in cancellous bone. *Bone* 23: 373–378.
22. Andrews JC, Almeida E, van der Meulen MCH, Alwood JS, Lee C, et al. (2010) Nanoscale X-ray microscopic imaging of mammalian mineralized tissue. *Microscopy and Microanalysis* 16: 327–336.
23. Reichert JC, Saifzadeh S, Wullschleger ME, Epari DR, Schütz M a, et al. (2009) The challenge of establishing preclinical models for segmental bone defect research. *Biomaterials* 30: 2149–2163.
24. Donnelly E, Baker SP, Boskey AL, van der Meulen MCH (2006) Effects of surface roughness and maximum load on the mechanical properties of cancellous bone measured by nanoindentation. *Journal of Biomedical Materials Research Part A* 77: 426–435.
25. Gimenez-Martin G, Risueno MC (1967) A simple staining technique for electron microscopy with lead–uranyl acetate. *Separatum Experientia* 23:316–318.

26. Liu Y, Meirer F, Williams PA, Wang J, Andrews JC, et al. (2012) TXM-Wizard: a program for advanced data collection and evaluation in full-field transmission X-ray microscopy. *Journal of Synchrotron Radiation* 19:281-287.
27. Zack GW, Rogers WE, Latt SA. (1977) Automatic measurement of sister chromatid exchange frequency. *Journal of Histochemistry & Cytochemistry* 25: 741–753.
28. Landrigan MD, Roeder RK (2009) Systematic error in mechanical measures of damage during four-point bending fatigue of cortical bone. *Journal of Biomechanics* 42: 1212–1217.
29. Hayat MA (2000) *Principles and Techniques of Electron Microscopy: Biological Applications*. Cambridge, Cambridge University Press. 543 p.
30. Larrue A, Rattner A, Peter Z-A, Olivier C, Laroche N, et al. (2011) Synchrotron radiation micro-CT at the micrometer scale for the analysis of the three-dimensional morphology of microcracks in human trabecular bone. *PLoS ONE* 6: e21297.
31. Voide R, Schneider P, Stauber M, Wyss P, Stampanoni M, et al. (2009) Time-lapsed assessment of microcrack initiation and propagation in murine cortical bone at submicrometer resolution. *Bone* 45: 164–173.
32. Burr DB, Schaffler MB, Frederickson RG (1998) Composition of the cement line and its possible mechanical role as a local interface in human compact bone. *Journal of Biomechanics* 21:939-945.
33. Jepsen KJ, Davy DT, Krzypow DJ (1999) The role of the lamellar interface during torsional yielding of human cortical bone. *Journal of Biomechanics* 32: 303–310.

34. O'Brien F, Taylor D, Lee TC (2007) Bone as a composite material: The role of osteons as barriers to crack growth in compact bone. *International Journal of Fatigue* 29: 1051–1056.
35. Schaffler MB, Choi K, Milgrom C (1995) Aging and matrix microdamage accumulation in human compact bone. *Bone* 17: 521–525.
36. Parsamian GP, Norman TL (2001) Diffuse damage accumulation in the fracture process zone of human cortical bone specimens and its influence on fracture toughness. *Journal of Materials Science Materials in Medicine* 12: 779–783.
37. Liu Y, Wang J, Hong Y, Wang Z, Zhang K, et al. (2012) Extended depth of focus for transmission x-ray microscope. *Optics Letters* 37: 3708–3710.

Chapter 5

Lacunar-Canalicular Network is Comprised Mainly of Canaliculi near the Trabecular Surface

5.1 Introduction

Bone is a hierarchical structure comprised of many levels of scale and function that combine to give bone its strength and stiffness⁽¹⁾. At the nanoscale the bone cells are present in lacunae that are linked through a lacunar-canalicular network^(2,3). The lacunar-canalicular network is the method for solute transport throughout bone tissue and is believed to be critical for osteocyte survival⁽⁴⁾. Through osteocyte apoptosis, bone is able to remodel and repair damaged tissue⁽⁵⁾. Shear stresses on the osteocytes and processes within this network are theorized to serve as a method for mechanosensory transduction within the bone⁽⁶⁻⁸⁾. Pulsed fluid flow across osteocytes inhibited osteoclast formation when tested in vitro, indicating fluid flow is important for remodeling of bone tissue⁽⁹⁾.

Fluid flow in bone is dependent on the nanoscale porosity. Studies examining fluid flow rely on estimates of volumes and dimensions for lacunae and canaliculi^(4,7). Simulations of fluid flow have indicated alterations in fluid velocities with a fatigue microcrack being present, indicating how small structural changes can have far reaching effects on the overall tissue⁽¹⁰⁾. Examinations of this network are typically completed on cortical bone tissue, with few studies examining trabecular bone microstructures. Despite the vast importance of osteocyte lacunar-canalicular network, our knowledge of this network is limited by visualization techniques that can capture the nanoscale structure.

Visualization of the lacunar canalicular network is difficult due to the small size of lacunae and canaliculi. Lacunae typically have a diameter of 10-20 μm ⁽¹¹⁾, while the canaliculi that extend out of the lacunae have diameters between 200-500 nm⁽¹²⁾. Three-dimensional measurements of the lacunar-canalicular network are typically made by three methods: serial sectioning with imaging, confocal imaging or synchrotron methods. Serial image measurements of the lacunar canalicular network have been created by combining scanning electron microscopy imaging with focused ion beam sectioning; however, this process requires access to microscopy equipment and is destructive⁽¹³⁾. The three dimensional network has been visualized using confocal microscopy with staining methods and illustrated the ellipsoidal lacunae shape⁽¹⁴⁾. However, the resolution limit of confocal microscopy is on the order of hundreds of nanometers. Finally, lacunar-canalicular networks can also be imaged using synchrotron tomography techniques^(11,15-17). Using synchrotron techniques lacunae have been shown to be ellipsoidal with lacunar geometry depending on the specific mouse strain^(11,18). The lacunar-canalicular network in human cortical bone has been characterized using a synchrotron-based focused ion beam⁽¹⁹⁾. All synchrotron studies are limited by long acquisition times or larger voxel sizes.

Transmission x-ray microscopy (TXM) is a synchrotron imaging technique using hard x-rays with 30 nm resolution⁽²⁰⁾. Two-dimensional images taken while rotating the sample of interest can be combined using tomographic reconstruction techniques to create 3D images. By altering the focal plane, one can also image larger samples through an extended depth of focus⁽²¹⁾. X-ray negative microdamage stains have been used in conjunction with TXM to demonstrate increased stain penetration in the lacunar-canalicular network with fatigue loaded samples when compared to monotonically loaded samples⁽²²⁾. Imaging of the lacunar network of mice that experienced microgravity indicated increased lacunar area, perimeter and canaliculi

diameter as compared to control mice illustrating the ability of TXM to visualize nanoscale changes⁽²³⁾.

The purpose of this study was to examine and quantify the lacunar-canalicular network within single trabeculae. Single trabeculae were excised from the distal femurs of ewes given an osteoporosis model followed by treatment. Samples were imaged using TXM with projection images taken at intervals around the sample. Projection images were used to reconstruct sample slices and create a 3D model of the trabeculae. Thresholds were then applied to determine the lacunar-canalicular network from bone tissue. Quantification of the lacunar-canalicular network was completed to determine the structure amounts and the total nanoscale porosity present within the tissue. Localization of the network was then examined to determine if the lacunar canalicular network had a gradient across trabeculae. We hypothesized that the localization of the lacunae and canaliculi would vary systematically throughout a trabeculae.

5.2 Methods

Bone tissue used in this study was obtained from previously published studies⁽²⁴⁾. Skeletally mature sheep femurs were used from two separate studies in which sheep were fed a metabolic acidosis diet followed by an anti-resorptive osteoporosis treatment (Table 5.1). A metabolic acidosis diet serves as an osteoporosis model through reduced bone mineral density, inducing osteopenia in ewes^(25,26). In the first study, metabolic acidosis (MA) diet was administered for six months⁽²⁵⁾ followed by six months of MA diet and treatment with alendronate (ALN, n=3 with 2 trabeculae from the same animal, 0.15 mg/kg), raloxifene (RAL, n=4; 0.8 mg/kg), or vehicle (MA1, n=2). ALN and RAL were administered daily via cannula into the duodenum following clinical dosing regimens⁽²⁷⁾. In a second study ewes were given a MA diet for eight months followed by administration of zoledronate (ZOL, n=3, 5 mg/sheep) or

vehicle (MA2, n=3). ZOL was administered once via sub-cutaneous injection following the clinical dosing regimen⁽²⁸⁾. A final group of control sheep were fed a normal sheep diet (C, n=2).

Table 5.1: Experimental design for treatment groups showing experimental duration. Samples were taken from two separate studies. In the first study, sheep were given a metabolic acidosis diet for six months followed by six months treatment with alendronate (ALN; n=3, 2 trabeculae taken from same sheep), raloxifene (RAL; n=4) or vehicle (MA1; n=2). A fourth group served as control (C; n=2) and was fed a normal sheep diet. In the second experiment sheep were given the metabolic acidosis diet for eight months followed by six months of treatment with zoledronate (ZOL; n=3) or vehicle (MA2; n=3).

	n	Month													
		1	2	3	4	5	6	7	8	9	10	11	12	13	14
Control	2	Normal Diet												X	X
MA1	2	MA Diet						MA + Vehicle						X	X
ALN	3	MA Diet						MA + Alendronate						X	X
RAL	4	MA Diet						MA + Raloxifene						X	X
MA2	3	MA Diet						MA + Vehicle							
ZOL	3	MA Diet						MA + Zoledronate							

Post-euthanasia, femurs were excised from the sheep. Sections of the distal condyles were removed with a low speed diamond saw (Buehler Isomet; Lake Bluff, IL). Marrow was removed using HA-buffered PBS with a high pressure water jet. Samples were then stored in 100% ethanol for one week. Single trabeculae were excised from the preserved trabecular bone under a dissection microscope with tweezers and a scalpel. Care was taken to ensure that the center of the trabeculae, which would be imaged, was not touched by the tools. Prior to imaging, samples were mounted on a 45/90 SEM stub (Ted Pella, Redding, CA) with carbon tape. Each individual trabecula was mounted vertically such that tomographic reconstructions would create transverse sections.

Trabeculae were imaged at the Stanford Synchrotron Radiation Lightsource (SSRL) using the transmission x-ray microscopy instrument (Xradia TXM, Pleasanton, CA; Beamline 6-2c)^(20,22). Prior to imaging, 1 μm gold fiduciary markers were attached to the samples to allow for

image alignment. Imaging was completed with energy of 8.1 keV. Single image tiles contained 1024x1024 pixels with a pixel edge length of 31.6 nm. Tiles were stitched together to create mosaic images across the entire width of the trabeculae with a 30% overlap ratio, consistent with prior studies⁽²²⁾. Final-stitched mosaic images imaged an area the entire width by 32 μm height. Mosaic images were taken at 3 degree intervals from -90 to 90 degrees. Slices reconstructed in regions with a gold marker were removed from the analysis due to beam hardening concerns.

Projection images were reconstructed into slices using the TXM Wizard⁽²⁹⁾. The size of the projection images was reduced using a 5x5 bin (voxels of 162 nm edge length). Binning was necessary due to computational limitations during image reconstruction. Sinograms were created for each slice in the section and then reconstructed using an Algebraic Reconstruction Technique (ART) method⁽²⁹⁾. Use of the ART method allowed for clearer visualization of the lacunar-canalicular network, at the expense of greater computational time.

Post-reconstruction image analysis was completed using Matlab (Mathworks Inc., Natick MA). Images were thresholded with a Gaussian fit. The region containing the peak corresponding to bone was selected and fit to a Gaussian curve, with the lower threshold set to 3 standard deviations below the mean attenuation value and the upper threshold to 4 standard deviations above the mean value. The upper threshold was selected to eliminate the gold fiducial beads used for alignment, while maintaining the bone tissue volume.

The total porosity was defined as the total canalicular and lacunar volume within the tissue divided by the total trabecular volume. Lacunar density was calculated from a central reconstructed slice and defined as the total number of lacunae per bone tissue volume (no./mm³). To investigate differences between the surface and interior of the trabecula, the porosity was measured within five-micron rings from the surface to a depth of 40 microns using an eroding

algorithm. The eroded depth of 40 microns was based on the depth of a resorption cavity on a rod-like trabecula in human bone⁽³⁰⁾.

Treatment groups were compared using an ANOVA followed by a Tukey Kramer post-hoc test. Porosity was examined as a function of depth from surface by an ANCOVA with a Tukey post-hoc test, focusing on porosity at each depth, treatment group and their interaction. In all tests $p < 0.05$ indicated significance.

5.3 Results

The lacunar volume comprised approximately 1.5-3.7% of the trabeculae volume (Figure 5.1A). Canalicular volume was approximately twice the volume ($p < 0.0001$) of the lacunae comprising 3.6-9.8% of the trabeculae porosity (Figure 5.1B). The total lacunar-canalicular porosity was approximately 5.5-12.6% of the trabeculae volume (Figure 5.1C). Greater porosity due to canaliculi than lacunae was consistent across all treatment groups.

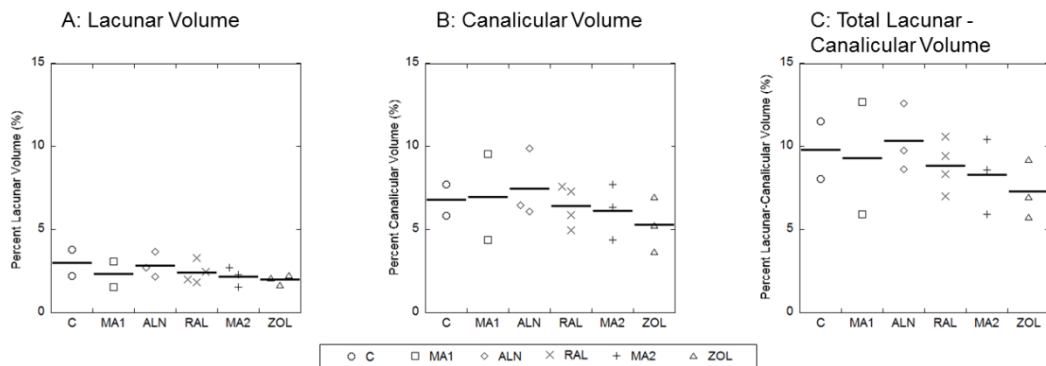


Figure 5.2: Lacunar-Canalicular volumes within trabeculae. A. Lacunar volumes varied between 1.5-3.7% of the overall trabecular volume; B. Canalicular volumes varied between 3.6-9.8% of the overall trabecular volume; C. Overall Lacunar-Canalicular volumes varied between 5.5-12.6% of the trabecular volume. Canalicular volume was greater than lacunar volume ($p < 0.0001$). Raw data points for each sample are shown, with lines representing the mean value for the treatment groups.

Lacunar density varied between 18,600 and 75,900 lacunae per mm^3 (mean across groups = 39,900 mm^3 ; Figure 5.2).

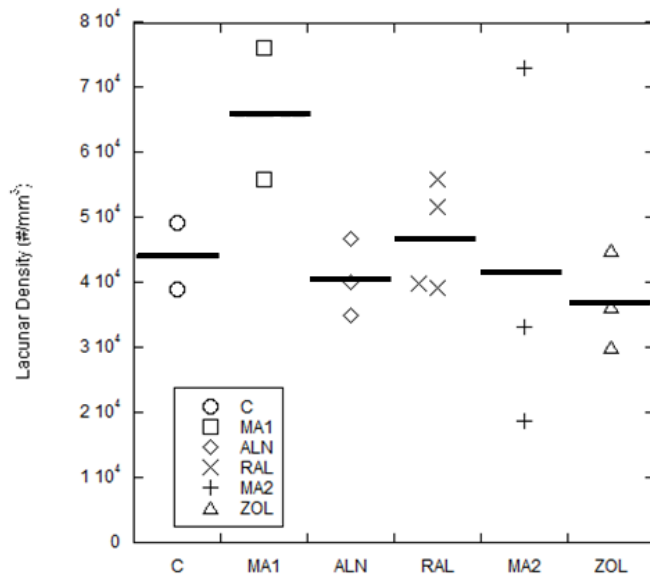


Figure 5.2: Lacunar density varied between 18,574 and 75,921 lacunae per cubic millimeter. No differences were present between treatment groups. Raw data points for each sample are shown, with lines representing the mean value for the treatment groups.

The volume of each osteocyte lacuna varied between 202 and 894 μm^3 (mean across groups = 623 μm^3 ; Figure 5.3).

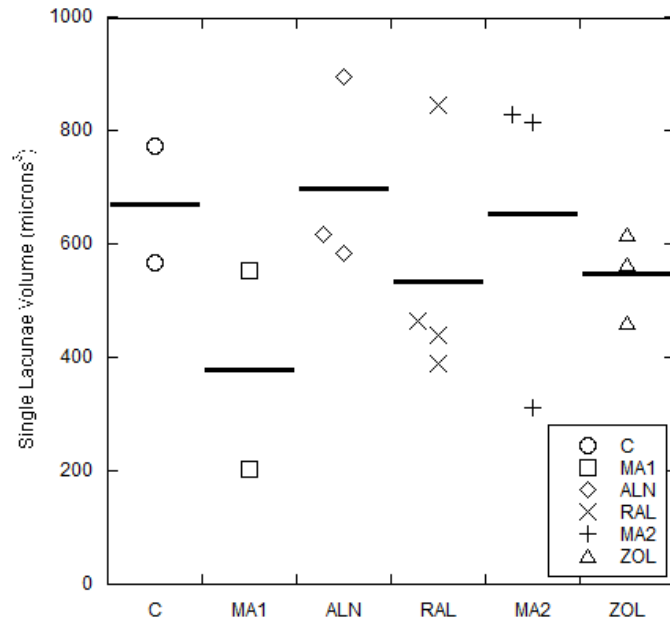


Figure 5.3: Volume of a single lacunae varied between 202 and 894 cubic microns. No differences occurred between groups. Raw data points for each sample are shown, with lines representing the mean value for the treatment groups.

When the porosity was examined as a function of depth from the trabecular surface, the greatest porosity occurred in the outer 5 μm (Figure 5.4).

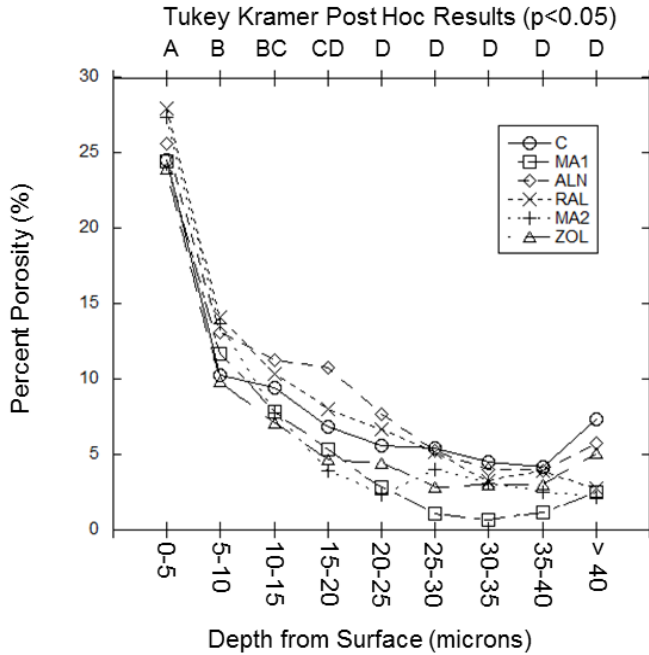


Figure 5.4: Lacunar-canalicular porosity as a function of depth from surface for each treatment group. Greater porosity was present at the surface and porosity decreased until a depth of 20 microns from the surface. Results of post-hoc comparisons are presented at the top with letters illustrating significant differences between depths, A > B > C > D.

The porosity was constant in the interior tissue located beyond 20 μm from the surface.

Slice-by-slice examination of images indicated a large number of lacunae located within the exterior tissue of the trabeculae, likely contributing to the increased porosity near the surface (Figure 5.5). Lacunar shape was noted to vary and was not always ellipsoidal (Figure 5). For all measures examined, differences were not present between treatment groups.

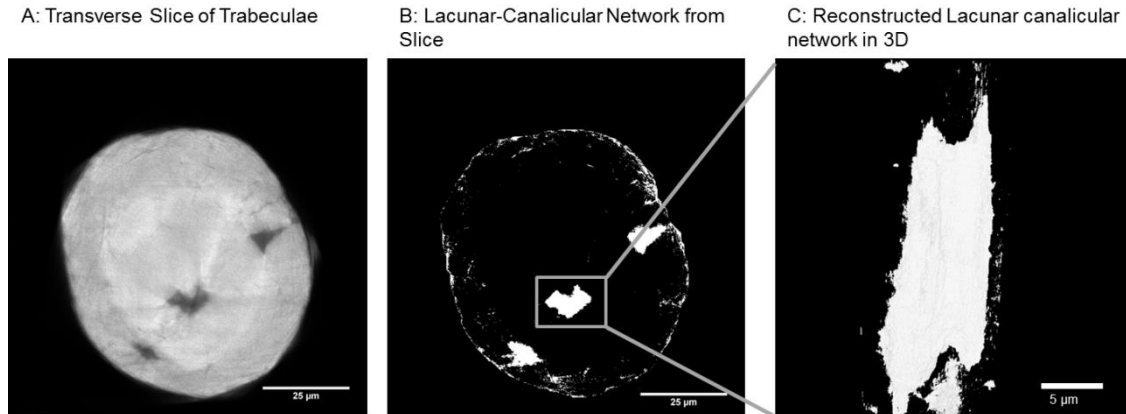


Figure 5.5: Illustrations of lacunar morphology. A: Transverse slice of a trabecula showing two osteocyte lacunae near the surface of the sample and one interior; B: Image from (a) with threshold applied to separate the lacunar-canalicular network. The canalicular density is greatest near the edge of the sample. Within this section, the lacunar shape is not elliptical; C: Three-dimensional reconstruction of interior lacuna and canaliculi again illustrates the complex, non-elliptical shape, suggesting the fusion of two lacunae.

5.4 Discussion

Individual trabeculae were imaged from sheep given different osteoporosis treatments with lacunar canalicular geometry being measured using synchrotron radiation TXM. Across all groups the lacunar-canalicular porosity was composed of approximately two thirds canaliculi and one third lacunae. The majority of the lacunar-canalicular network exists within the first 20 microns from the surface of the trabeculae. Reconstruction of the lacunar-canalicular network indicated lacunae present around the edge of the trabeculae, likely increasing the porosity near the surface of the trabeculae.

Comparisons of the overall lacunar-canalicular volumes indicated porosities between 5.5 to 12.6 percent (mean of 8.6% across all groups) with canalicular volume making up a greater portion than lacunae. Weight measures of bone tissue have indicated lacunar-canalicular volumes of approximately 8%⁽³¹⁾. In cortical bone the vascular network comprised 4% of the porosity while the lacunar-canalicular network comprised 5% leading to an overall porosity of 9%⁽³²⁾. The

range of porosities presented in this paper illustrate that there is variability in the porosity throughout a trabeculae, however the overall average is similar to values found in cortical bone tissue.

Lacunae density measurements indicated between 18,600 and 75,900 lacunae per cubic millimeter with an average across groups of 39,900 lacunae per cubic millimeter (standard deviation of 14,600). Lacunar density has not been measured in sheep previously, however studies have shown a large difference in osteocyte density depending on animal type⁽³³⁾. Rats have a lacunar density of 93,200 while bovine bone was 31,900⁽³³⁾. Osteocyte density has shown dependence on age in humans in trabecular bone which also makes comparison difficult, as sheep in our study were given an osteoporosis model and treatment⁽³⁴⁾. Cortical bone area studies have found densities between 400-1000 lacunae per square millimeter⁽³⁵⁾ depending on age of human patients. Examination of the lacunar densities from trabeculae in this study in 2D fell in the same range of 400-900 lacunae per square millimeter. It should be noted that these values are extracted from the region imaged, which was only a small region of a single trabeculae, well below a cubic millimeter, which may account for the high standard deviation. Variability along the trabeculae could also not be examined due to the small region analyzed.

Volumes of single lacunae were between 202 and 894 cubic microns with an average across groups of 623 (standard deviation of 201). Human lacunae from femoral trabeculae measured by confocal microscopy had a mean volume of 476 (standard deviation of 224)⁽³⁶⁾. Data across species for lacunar volume is limited; however results presented in this study appear consistent with other studies in human models. Lacunae size as a function of location within the trabeculae was not analyzed, however this is a future avenue that would be interesting to explore.

Porosity measures indicated the greatest porosity at the surface of the samples. Analysis of the sections indicated a ring of lacunae that tended to be near to the surface of the trabeculae, as well as canaliculi which bridged the surface. This presence of lacunae may serve as a signaling method within the bone to communicate between the interior and exterior of the bone tissue. Lacunae also appeared to not be ellipsoidal, but rather took on a variety of shapes and sizes. Different shapes and sizes would impact the fluid flow throughout bone tissue and could ultimately have different effects for bone signaling in trabeculae.

There are limitations with this novel imaging technique and comparison of groups. Imaging artifacts may still be present and influence results; however use of the algebraic reconstruction technique should reduce artifacts present. Artifacts can be further reduced at the cost of repeated angle exposures greatly increasing imaging time in future studies. Thresholds were chosen by fitting a Gaussian peak to the attenuation data. This thresholding method can have the disadvantage of including low mineralized bone and excluding canaliculi with a higher attenuation. Partial volume effects can also have an effect on the data. Finally data binning was necessary due to computational limitations. Future advances in technology can allow for higher resolution scans and clearer images of the lacunar-canalicular network.

Results from this study are limited as to the comparison between groups. Single trabeculae from the distal portion of the femur were imaged for each sheep. Trabeculae were chosen to be rod like for ease of imaging, and to ensure the x-ray path through the sample was minimized. The orientation of these trabeculae with respect to the direction of loading within the bone tissue is unknown. Imaging single trabeculae from each sheep greatly diminishes any possibility of comparing drug treatments as alterations would be expected to be less than the

variability due to low sample size. Never-the-less our results were consistent across groups, indicating robustness of the methods we used for determining lacunar canalicular properties.

Results presented in this study are among the first lacunar-canalicular porosity measurements within trabeculae at this scale. During a 72 hour beam time we were able to examine the nanoscale porosity from 17 samples. Previous studies at similar resolutions have typically imaged only a few samples during a similar time span. With continued computational development it is believed that post-processing speeds should decrease allowing for quick imaging and analysis of the nanoscale structures of the bone. This data can be applied to examine alterations through pharmacologic treatments to better aid in disease treatment.

In conclusion, we have demonstrated that osteocyte lacunae are mainly located near the surface of trabeculae within 20 microns of depth from the surface. The overall porosity of the lacunar-canalicular network was comprised mainly of canaliculi, which bridge between lacunae and the surface of the sample. Based on these results canaliculi play a major role in bone signaling and solute transport between lacunae. In the future, the TXM methods used for these measurements can be applied to further examine this network and determine its mechanisms of communication.

5.5 References:

1. Liebschner MA., Wettergreen MA. Optimization of Bone Scaffold Engineering for Load Bearing Applications. In: Waris T, Ashammakhi N, editors. *Top. Tissue Eng.* 2003. p. 1–39.
2. Nordin M, Frankel VH. *Biomechanics of Bone. Basic Biomech. Musculoskelet. Syst. Second.* Malvern, Pennsylvania, USA: Lee & Febiger; 1989. p. 3–29.
3. Jacobs CR, Temiyasathit S, Castillo AB. Osteocyte mechanobiology and pericellular mechanics. *Annu. Rev. Biomed. Eng.* 2010 Aug 15;12:369–400.

4. Wang L, Wang Y, Han Y, Henderson SC, Majeska RJ, Weinbaum S, Schaffler MB. In situ measurement of solute transport in the bone lacunar-canalicular system. *Proc. Natl. Acad. Sci. U. S. A.* 2005 Aug 16;102(33):11911–6.
5. Verborgt O, Gibson GJ, Schaffler MB. Loss of osteocyte integrity in association with microdamage and bone remodeling after fatigue in vivo. *J. Bone Miner. Res.* 2000 Jan;15(1):60–7.
6. Cowin SC, Weinbaum S, Zeng Y. A Case of Bone Canaliculi as the Anatomical Site of Strain Generated Potentials. *J. Biomech.* 1995;28(11):1281–97.
7. Weinbaum S, Cowin SC, Zeng Y. A model for the excitation of osteocytes by mechanical loading-induced bone fluid shear stresses. *J. Biomech.* 1994 Mar;27(3):339–60.
8. Turner CH, Forwood MR, Otter MW. Mechanotransduction in bone: do bone cells act as sensors of fluid flow? *FASEB J.* 1994;8:875–8.
9. Tan SD, de Vries TJ, Kuijpers-Jagtman AM, Semeins CM, Everts V, Klein-Nulend J. Osteocytes subjected to fluid flow inhibit osteoclast formation and bone resorption. *Bone.* 2007 Nov;41(5):745–51.
10. Galley S a, Michalek DJ, Donahue SW. A fatigue microcrack alters fluid velocities in a computational model of interstitial fluid flow in cortical bone. *J. Biomech.* 2006 Jan;39(11):2026–33.
11. Dong P, Hauptert S, Hesse B, Langer M, Gouttenoire P-J, Bousson V, Peyrin F. 3D osteocyte lacunar morphometric properties and distributions in human femoral cortical bone using synchrotron radiation micro-CT images. *Bone.* Elsevier Inc.; 2014 Mar;60:172–85.
12. You L-D, Weinbaum S, Cowin SC, Schaffler MB. Ultrastructure of the osteocyte process and its pericellular matrix. *Anat. Rec. A. Discov. Mol. Cell. Evol. Biol.* 2004 Jun;278(2):505–13.
13. Schneider P, Meier M, Wepf R, Müller R. Serial FIB/SEM imaging for quantitative 3D assessment of the osteocyte lacuno-canalicular network. *Bone.* Elsevier Inc.; 2011 Aug;49(2):304–11.
14. Ciani C, Doty SB, Fritton SP. An effective histological staining process to visualize bone interstitial fluid space using confocal microscopy. *Bone.* Elsevier Inc.; 2009 May;44(5):1015–7.
15. Varga P, Hesse B, Langer M, Schrof S, Männicke N, Suhonen H, Pacureanu A, Pahr D, Peyrin F, Raum K. Synchrotron X-ray phase nano-tomography-based analysis of the lacunar–canalicular network morphology and its relation to the strains experienced by

- osteocytes in situ as predicted by case-specific finite element analysis. *Biomech. Model. Mechanobiol.* 2014 Jul 11;(July):1–16.
16. Pacureanu A, Langer M, Boller E, Tafforeau P, Peyrin F. Nanoscale imaging of the bone cell network with synchrotron X-ray tomography: optimization of acquisition setup. *Med. Phys.* 2012;39(4):2229–38.
 17. Hesse B, Männicke N, Pacureanu A, Varga P, Langer M, Maurer P, Peyrin F, Raum K. Accessing osteocyte lacunar geometrical properties in human jaw bone on the submicron length scale using synchrotron radiation μ CT. *J. Microsc.* 2014 Jun 8;49:1–11.
 18. Schneider P, Stauber M, Voide R, Stampanoni M, Donahue LR. Ultrastructural Properties in Cortical Bone Vary Greatly in Two Inbred Strains of Mice as Assessed by Synchrotron Light Based Micro- and Nano-CT. *J. Bone Miner. Res.* 2007;22(10):1557–70.
 19. Dierolf M, Menzel A, Thibault P, Schneider P, Kewish CM, Wepf R, Bunk O, Pfeiffer F. Ptychographic X-ray computed tomography at the nanoscale. *Nature.* Nature Publishing Group; 2010 Sep 23;467(7314):436–9.
 20. Andrews JC, Almeida E, van der Meulen MCH, Alwood JS, Lee C, Liu Y, Chen J, Meirer F, Feser M, Gelb J, Rudati J, Tkachuk A, Yun W, Pianetta P. Nanoscale X-ray microscopic imaging of mammalian mineralized tissue. *Microsc. Microanal.* 2010 Jun;16:327–36.
 21. Liu Y, Wang J, Hong Y, Wang Z, Zhang K, Williams PA, Zhu P, Andrews JC, Pianetta P, Wu Z. Extended depth of focus for transmission x-ray microscope. *Opt. Lett.* 2012;37(17):3708–10.
 22. Brock GR, Kim G, Ingrassia AR, Andrews JC, Pianetta P, van der Meulen MCH. Nanoscale examination of microdamage in sheep cortical bone using synchrotron radiation transmission x-ray microscopy. *PLoS One.* 2013 Jan;8(3):e57942.
 23. Blaber E a, Dvorochkin N, Lee C, Alwood JS, Yousuf R, Pianetta P, Globus RK, Burns BP, Almeida E a C. Microgravity induces pelvic bone loss through osteoclastic activity, osteocytic osteolysis, and osteoblastic cell cycle inhibition by CDKN1a/p21. *PLoS One.* 2013 Jan;8(4):e61372.
 24. Burket JC, Brooks DJ, MacLeay JM, Baker SP, Boskey AL, van der Meulen MCH. Variations in nanomechanical properties and tissue composition within trabeculae from an ovine model of osteoporosis and treatment. *Bone.* Elsevier Inc.; 2013 Jan;52(1):326–36.
 25. MacLeay JM, Olson JD, Enns RM, Les CM, Toth CA, Wheeler DL, Turner AS. Dietary-induced metabolic acidosis decreases bone mineral density in mature ovariectomized ewes. *Calcif. Tissue Int.* 2004 Nov;75:431–7.

26. Macleay JM, Olson JD, Turner AS. Effect of dietary-induced metabolic acidosis and ovariectomy on bone mineral density and markers of bone turnover. *J. Bone Miner. Metab.* 2004 Jan;22(6):561–8.
27. Bone HG, Adami S, Rizoli R, Favus M, Ross PD, Santora A, Prahalada S, Daifotis A, Orloff J, Yates J. Weekly Administration of Alendronate: Rationale and Plan for Clinical Assessment. *Clin. Ther.* 2000;22(1):15–28.
28. Black DM, Delmas PD, Eastell R, Reid IR, Boonen S, Cauley JA, Cosman F, Lakatos P, Leung PC, Man Z, Mautalen C, Mesenbrink P, Hu H, Caminis J, Tong K, Rosario-jansen T, Krasnow J, Hue TF, Sellmeyer D, Eriksen EF, Sc DM, Cummings SR. Once-Yearly Zoledronic Acid for Treatment of Postmenopausal Osteoporosis. *N. Engl. J. Med.* 2007;356(18):1809–22.
29. Liu Y, Meirer F, Williams P a, Wang J, Andrews JC, Pianetta P. TXM-Wizard: a program for advanced data collection and evaluation in full-field transmission X-ray microscopy. *J. Synchrotron Radiat. International Union of Crystallography*; 2012 Mar;19(Pt 2):281–7.
30. Goff MG, Slyfield CR, Kummari SR, Tkachenko E V, Fischer SE, Yi YH, Jekir MG, Keaveny TM, Hernandez CJ. Three-dimensional characterization of resorption cavity size and location in human vertebral trabecular bone. *Bone.* 2012 Jul;51(1):28–37.
31. Robinson RA. Physiochemical Structure of Bone. *Clin. Orthop. Relat. Res.* 1975;112(October):263–315.
32. Zhang D, Weinbaum S, Cowin SC. Estimates of the Peak Pressures in Bone Pore Water. *J. Biomech. Eng.* 1998;120:697–703.
33. Mullender MG, Huiskes R, Versleyen H, Buma P. Osteocyte Density and Histomorphometric Parameters in Cancellous Bone of the Proximal Femur in Five Mammalian Species. *J. Orthop. Res.* 1996;14:972–9.
34. Mullender MG, van der Meer DD, Huiskes R, P L. Osteocyte Density Changes in Aging and Osteoporosis. *Bone.* 1996;18(2):109–13.
35. Vashishth D, Verborgt O, Divine G, Schaffler MB, Fyhrie DP. Decline in osteocyte lacunar density in human cortical bone is associated with accumulation of microcracks with age. *Bone.* 2000 Apr;26(4):375–80.
36. McCreadie BR, Hollister SJ, Schaffler MB, Goldstein S a. Osteocyte lacuna size and shape in women with and without osteoporotic fracture. *J. Biomech.* 2004 Apr;37(4):563–72.

Chapter 6

Summary and Future Directions

6.1 Discussion and Summary

Osteoporosis treatments reduce fracture risk ^(1,2) and provide a major step forward in patient quality of life. The occurrence of atypical femoral fractures (AFF), while rare, indicates that unknowns exist with bisphosphonate treatments that need to be examined⁽³⁾. In previous studies, mechanical property changes with bisphosphonate treatments have been examined using mainly monotonic, whole bone testing techniques ⁽⁴⁾. Alterations to material properties, including increased collagen maturity, occur with bisphosphonate treatment⁽⁵⁻⁸⁾. These alterations typically have been measured at the microscale; however, bone tissue contains a nanoscale canalicular network, which may influence tissue properties with treatment.

The cortical bone fatigue data for osteoporosis treatments (presented in Chapter 3) have implications for clinical treatment of osteoporosis. AFFs have features that indicate fatigue is likely the failure mechanism⁽⁹⁾. We found that cortical samples from sheep treated with alendronate had a shorter fatigue life as compared to the grand mean of the data, yet cortical tissue treated with zoledronate had no change in fatigue life. The fatigue life difference was surprising and unexpected given zoledronate's higher binding affinity^(10,11). This result indicates that dosing, method of administration, binding affinity and chemical structure may affect the fatigue properties of treated bone tissue. PTH treatment increased fatigue life of cortical bone and may, therefore, present a mechanism for aiding in AFF recovery. This study presents the first data comparing fatigue life of tissue treated with different bisphosphonates and PTH.

Using synchrotron imaging with lead uranyl acetate to label new surfaces, we showed that nanoscale damage morphologies differ from the microscale (Chapter 4). Increased staining present within the lacunar-canalicular network indicated that the bone microstructure could be playing a role in damage formation. Staining also took different forms in notched samples, showing cross-hatch patterns forming below typical microdamage resolutions. Comparison of TXM with microCT showed that quantification by microCT overestimated the stained tissue area and demonstrated different damage morphology compared to TXM. The effect of osteoporosis treatments on alterations to the lacunar-canalicular network is unknown. If alterations from treatment do exist, different damage propensities to the tissue may result at the nanoscale.

TXM imaging of individual trabeculae showed the vast network of lacunae and canaliculi which exist as porosity within trabeculae. The majority of the network occurred at the trabecular surface, with canaliculi comprising approximately twice the volume as lacunae. No differences occurred between any bisphosphonate treatment groups; however, in all groups greater porosity was present at the surface and the contribution to the volume from canaliculi was greater. This result indicates that the nanoscale network exists mainly within regions known to be altered with bisphosphonate treatments. While differences due to treatment did not occur in this study, the groundwork has been laid for further examination and determination of nanoscale tissue alterations with treatment. The lack of differences between groups was also not unexpected, as the sample size for each group was small due to the use of synchrotron imaging, which is not a high throughput technique.

Synchrotron TXM results should be viewed in comparison to typical bone imaging technology. While nanoscale resolutions are possible, using the TXM to image bone tissue proved highly

labor and time intensive. This imaging technique requires a synchrotron source and specialized equipment to achieve the exquisite resolution. Data reconstruction from these techniques was time intensive and necessitated binning of the data. Full reconstruction of the three-dimensional tomographies with 32 nm voxel size from this thesis were estimated to require more than a decade to complete; hence the data were binned and reconstructed at a lower resolution.

Synchrotron systems cannot be applied in the clinical setting, as the radiation dosages are large.

A recent study imaged mouse bone in vivo with synchrotron tomography; however, the voxel size in this setting was 11.7 microns, and radiation exposure was noted as a limitation⁽¹²⁾.

Despite the previously mentioned limitations, the benefits from synchrotron technology are immense. As computers and technology continue to advance, reconstructions will take fractions of their current time. Increased use of nanoscale X-Ray CT systems will expand our current knowledge and measures of the lacunar-canalicular network and create more consistent metrics for describing their geometry. The lack of nanoscale measurement techniques has led to a variety of metrics to describe lacunar morphology including measures of length, width and depth, fitting with ellipsoids, and relative comparisons of axis length of the lacunae⁽¹³⁻¹⁷⁾. Synchrotron systems cannot be used clinically; however, synchrotron systems can be used to understand the changes that osteoporosis treatments are creating at the basic science level. The use of synchrotron-based imaging techniques to examine new osteoporosis therapies may help predict whether a drug is likely to cause undesired side effects many years down the road.

The three studies presented in this thesis combine to raise a fundamental question: do we understand the changes that are occurring at the nanoscale in bone? The first project indicates that, despite similar mechanisms of action, osteoporotic treatments can have different effects on

the fatigue life of cortical bone, demonstrating material property changes that are not found through monotonic testing methods. The second project indicates that damage occurs within cortical bone structures at scales below levels typically viewed for microdamage. The third project builds on this finding to show that porosity differences are not consistent throughout single trabeculae and gradients in porosity exist from the surface. Damage may, therefore, not be consistent across trabeculae, as greater porosity exists at the surface. Continued research into the material and structural property changes with bisphosphonate treatment can yield important information about treatment mechanisms.

6.2 Future Directions

The methods and results developed in the prior chapters lend themselves to several research avenues. Expansion on current results can help determine the occurrence of AFFs and explain differences between treatment groups. Continued synchrotron imaging can also better illustrate porosity and mineralization alterations to the tissue. New research paths can also be created with the use of TXM.

6.2.1 Continued Research Avenues

6.2.1.1 Osteoporosis Treatment Analysis

Continuation of the fatigue testing using tensile and compressive fatigue loading modes is a logical next step and may indicate differences in tissue properties for each loading condition. The use of four-point bend fatigue testing is not optimal and has been stated to be a creep driven effect⁽¹⁸⁾. Four-point bend fatigue creates concurrent tensile and compressive surfaces, which could both initiate failures within the tissue. AFFs begin as a stress fracture on the lateral cortex

of the femur⁽³⁾, which experiences a tensile load, suggesting that AFFs are the result of a tensile failure. Tensile and compressive fatigue testing could not be completed for the samples presented in Chapter 3, as the samples were created from limited remaining tissue from previously published and to-be-published studies⁽¹⁹⁾. Variation in the strain levels to create S-N curves is also a possible next step; however, more tissue is again needed. Fracture toughness testing could also yield important results, as this testing has never been completed on bisphosphonate-treated tissue.

6.2.1.2 Continued Synchrotron Imaging

The results presented using synchrotron imaging illustrates novel avenues of research to be explored. Synchrotron analysis methods developed for bone tissue in Chapters 4 and 5 can now be applied to further samples to examine damage, mineralization, and lacunar-canalicular geometry. TXM has the ability to determine how osteoporotic treatments affect the lacunar canalicular network, which could impact whole bone mechanics. This type of analysis was attempted (Chapter 5); however, low sample sizes due to limited time on a shared instrument prevented the possibility of analysis between osteoporosis treatments. Continued imaging of more samples, with longer exposure times and smaller angles between individual tomographs, can yield more knowledge into the nanoscale porosity of bone tissue. Computational limitations will no longer exist with advancing technology allowing for higher resolution images of the bone tissue to be completed. The damage visualization results presented for cortical bone in Chapter 4 were completed on two-dimensional sections. Having a nanoscale three-dimensional image of a microcrack could start to answer the question of where in the tissue a crack initiates. The role of the lacunar-canalicular network in crack formation could then be examined to determine if cracks follow the nanoscale porosity of the bone tissue. Repeating the imaging experiments in

Chapters 4 and 5 with higher resolution and in three dimensions could answer many questions about damage formation and tissue alterations with osteoporosis treatments.

6.2.1.3 Continued AFF Analysis

AFFs are likely caused by a combination of material property changes and geometry, which alters the stresses experienced within the cortical tissue. The femoral geometry in patients with AFFs is not well understood, and a percentage of the population may be predisposed to having these fractures due to their lower limb morphology. The bi-lateral nature of fractures indicates a geometric component that could be altering the stress state on the lateral side of the bone. Finite element modeling was attempted to understand how stress distributions occur in femurs with AFF, however difficulties in procuring scans and ensuring consistent loading prevented determining if the stress state is different. Using a consistent collection of scans, one could model the stresses experienced within the bone and determine if the stress state on the lateral cortex in patients with an AFF is different from the stress state in age-controlled non-AFF patients. Determining the applied stresses, in combination with fatigue properties, could also indicate a risk of fracture for patients who are receiving bisphosphonate treatment. Continued analysis of tissue properties in patients with an AFF could yield important results, as fatigue properties of fractured tissue and the tissue fracture toughness are unknown.

6.2.2 New Research Avenues

6.2.2.1 New Osteoporosis Treatment Testing

The altered fatigue life data with osteoporosis treatment, presented in Chapter 3, opens up many new research avenues. The question of how do different bisphosphonates affect remodeling, and

what impact does this altered remodeling have on the material properties of the tissue needs to be answered. Differences in the fatigue life of the cortical bone tissue could not be explained through the limited material measurements examined within the study. Bisphosphonates are known to alter tissue properties and increase collagen maturity⁽⁵⁻⁸⁾. Serum CTX, a marker of bone resorption, changes with time from last bisphosphonate treatment^(20,21); however, no published studies have examined material property changes for cortical bone as a function of bisphosphonate dosing amount, time and type. Completing a study using an animal model with various dosing methods could greatly improve our knowledge of the nanoscale effects of bisphosphonates on bone tissue. Collecting serum measures and analyzing bone turnover, and recovery of measures to pre-treatment homeostasis, would indicate if treatments could have alternative side effects influencing AFFs. Additionally, one could include PTH therapy after bisphosphonate treatment and determine whether bone remodeling is recovered by treatment. A study of this nature would also produce bone tissue samples that could be used for nanoscale FTIR to determine if every treatment creates the same mineralization distribution across cortical and cancellous bone tissue. While difficult, fatigue analyses could also be attempted and fracture toughness determined. Recently, whole bone three-point bend testing of mouse femora with a notch applied to the cortical diaphysis was reported, with fracture toughness and work at fracture measured as a function of the crack extension⁽²²⁾. Results of this nature could indicate, for the first time, how remodeling rates affect the fatigue and fracture properties with bisphosphonate treatment. Clinically the results may indicate different optimal dosing times and amounts for preservation of the fatigue and fracture properties.

Application of composite beam theory mechanics to the nanomechanical bone could also explain the large reduction of fracture risk. Mechanical testing measures of bone are typically

completed at continuum scales, not accounting for variation in nanoscale tissue properties. Bisphosphonates are known to create up to a 50% reduction in fracture risk through a more modest 0-8% increase in BMD at corticocancellous sites^(1,2,23). This change indicates that alterations likely occur to the material properties of the tissue. Nanoindentation on single trabeculae has indicated surface-based changes in indentation modulus and hardness with zoledronate treatment⁽¹⁹⁾. Spatial differences with treatments could alter the stress state within the tissue. Applying knowledge of composite beam theory could explain this large change in fracture risk. Using synchrotron imaging on bisphosphonate-treated samples; one could analyze the distribution of mineralization changes at the nanoscale. Through this measure, the density weighted moment of inertia could be calculated, in the overall cortical diaphysis tissue, or within single trabeculae⁽²⁴⁾. Changes to the stress and strain states of the bone could then be calculated. Composite beam theory may indicate that, while the BMD changes are modest, the surface-based nature of the bone mass changes increases the density weighted moment thereby decreasing the stresses occurring within tissue. The implication from this result is that an osteoporosis treatment that has greater surface effects may have a larger fracture risk reduction than one with more centralized tissue changes.

6.2.2.1 New Synchrotron Imaging Methods

The methods developed with the TXM can be applied to a variety of bone tissues. Measuring the lacunar canalicular porosity of knockout mice could produce important results for examining how alterations to specific signaling pathways alter the nanoscale bone porosity. Bone material properties are often altered in knockout mice, however if these changes are due to the collagen/mineral or to the porosity is unknown. Sample preparation techniques must be improved such that smaller samples, with no damage artifacts from preparation, are created. Using micro-mills

machining small sections of bone may be possible, which could be imaged with nanoscale resolution. The TXM facility at SSRL has a resolution of 30 nm⁽²⁵⁾, whereas the closest published study indicating lacunar and canalicular networks was at 65 nm voxel size⁽¹⁵⁾. Tomography imaging tissue with long exposure times and a greater number of projection images, taken at smaller increments, could produce important information as bone tissue has not been viewed in three dimensions at this scale. The smaller voxel size with TXM may allow visualization of an even more distributed canalicular network within the bone tissue, with vasculature evident at scales never before imaged.

In conclusion, the results presented in this thesis pose many interesting questions. Fatigue life was altered differently by alendronate and zoledronate treatments despite similar methods of action. Different dosing frequency, method of administration, binding affinity or chemical structure may cause these fatigue property difference. Synchrotron radiation TXM was used to illustrate that repetitive loading creates increased microdamage stain presence in cortical bone tissue. This result suggests that damage initiation occurs at the nanoscale, within the lacunar canalicular network. Finally, TXM was used to visualize the lacunar canalicular network in 3D indicating nanoscale porosity exists mainly at the surface of trabeculae, and is comprised mostly of canaliculi.

6.3 References

1. Cummings SR, Karpf DB, Harris F, Genant HK, Ensrud K, LaCroix AZ, Black DM. Improvement in spine bone density and reduction in risk of vertebral fractures during treatment with antiresorptive drugs. *Am. J. Med.* 2002 Mar;112:281–9.
2. Ettinger B, Black DM, Mitlak BH, Knickerbocker RK, Nickelsen T, Genant HK, Christiansen C, Stakkestad J, Glu CC, Krueger K, Cohen FJ, Eckert S, Avioli L V. Reduction of Vertebral Fracture Risk in Postmenopausal Women With Osteoporosis

- Treated With Raloxifene: Results From a 3-Year Randomized Clinical Trial. *J. Am. Med. Assoc.* 1999;282(7):637–45.
3. Shane E, Burr D, Abrahamsen B, Adler RA, Brown TD, Cheung AM, Cosman F, Curtis JR, Dell R, Dempster DW, Ebeling PR, Einhorn TA, Genant HK, Geusens P, Klaushofer K, Lane JM, McKiernan F, McKinney R, Ng A, Nieves J, O’Keefe R, Papapoulos S, Howe T Sen, van der Meulen MC, Weinstein RS, Whyte MP. Atypical subtrochanteric and diaphyseal femoral fractures: second report of a task force of the american society for bone and mineral research. *J. Bone Miner. Res.* 2014 Jan;29(1):1–23.
 4. Allen MR, Burr DB. Mineralization , Microdamage , and Matrix : How Bisphosphonates Influence Material Properties of Bone. *BoneKEy-Osteovision.* 2007;4(2):49–60.
 5. Donnelly E, Meredith DS, Nguyen JT, Gladnick BP, Rebolledo BJ, Shaffer AD, Lorich DG, Lane JM, Boskey AL. Reduced cortical bone compositional heterogeneity with bisphosphonate treatment in postmenopausal women with intertrochanteric and subtrochanteric fractures. *J. bone Miner. Res.* 2012 Mar;27(3):672–8.
 6. Bala Y, Depalle B, Farlay D, Douillard T, Meille S, Follet H, Chapurlat R, Chevalier J, Boivin G. Bone micromechanical properties are compromised during long-term alendronate therapy independently of mineralization. *J. bone Miner. Res.* 2012 Apr;27(4):825–34.
 7. Paschalis EP, Mendelsohn R, Boskey AL. Infrared assessment of bone quality. *Clin. Orthop. Relat. Res.* 2011 Aug;469(8):2170–8.
 8. Roschger P, Paschalis EP, Fratzl P, Klaushofer K. Bone mineralization density distribution in health and disease. *Bone.* 2008 Mar;42(3):456–66.
 9. Van der Meulen MC, Boskey AL. Atypical subtrochanteric femoral shaft fractures: role for mechanics and bone quality. *Arthritis Res. Ther.* 2012 Aug 29;14(220):1–8.
 10. Shaw NJ, Bishop NJ. Bisphosphonate treatment of bone disease. *Arch. Dis. Child.* 2005 May;90(5):494–9.
 11. Reszka AA, Rodan GA. Bisphosphonate mechanism of action. *Curr. Rheumatol. Rep.* 2003 Feb;5:65–74.
 12. Matsumoto T, Nishikawa K, Tanaka M, Uesugi K. In vivo CT quantification of trabecular bone dynamics in mice after sciatic neurectomy using monochromatic synchrotron radiation. *Calcif. Tissue Int.* 2011 May;88(5):432–41.
 13. Pacureanu A, Langer M, Boller E, Tafforeau P, Peyrin F. Nanoscale imaging of the bone cell network with synchrotron X-ray tomography: optimization of acquisition setup. *Med. Phys.* 2012;39(4):2229–38.

14. Schneider P, Stauber M, Voide R, Stampanoni M, Donahue LR. Ultrastructural Properties in Cortical Bone Vary Greatly in Two Inbred Strains of Mice as Assessed by Synchrotron Light Based Micro- and Nano-CT. *J. Bone Miner. Res.* 2007;22(10):1557–70.
15. Dierolf M, Menzel A, Thibault P, Schneider P, Kewish CM, Wepf R, Bunk O, Pfeiffer F. Ptychographic X-ray computed tomography at the nanoscale. *Nature* 2010 Sep 23;467(7314):436–9.
16. Larrue A, Rattner A, Peter Z-A, Olivier C, Laroche N, Vico L, Peyrin F. Synchrotron Radiation Micro-CT at the Micrometer Scale for the Analysis of the Three-Dimensional Morphology of Microcracks in Human Trabecular Bone. Brechbiel MW, editor. *PLoS One*. 2011 Jul 7;6(7):e21297.
17. Kazakia GJ, Burghardt a. J, Cheung S, Majumdar S. Assessment of bone tissue mineralization by conventional x-ray microcomputed tomography: Comparison with synchrotron radiation microcomputed tomography and ash measurements. *Med. Phys.* 2008;35(7):3170.
18. Landrigan MD, Roeder RK. Systematic error in mechanical measures of damage during four-point bending fatigue of cortical bone. *J. Biomech.* 2009 Jun 19;42(9):1212–7.
19. Burket JC, Brooks DJ, MacLeay JM, Baker SP, Boskey AL, van der Meulen MCH. Variations in nanomechanical properties and tissue composition within trabeculae from an ovine model of osteoporosis and treatment. *Bone*. 2013 Jan;52(1):326–36.
20. Rosen HN, Moses AC, Garber J, Iloputaife ID, Ross DS, Lee SL, Greenspan SL. Serum CTX: a new marker of bone resorption that shows treatment effect more often than other markers because of low coefficient of variability and large changes with bisphosphonate therapy. *Calcif. Tissue Int.* 2000 Feb;66(2):100–3.
21. Marx RE, Cillo JE, Ulloa JJ. Oral bisphosphonate-induced osteonecrosis: risk factors, prediction of risk using serum CTX testing, prevention, and treatment. *J. Oral Maxillofac. Surg.* 2007 Dec;65(12):2397–410.
22. Carriero A, Zimmermann E a, Paluszny A, Tang SY, Bale H, Busse B, Alliston T, Kazakia G, Ritchie RO, Shefelbine SJ. How tough is brittle bone? Investigating osteogenesis imperfecta in mouse bone. *J. Bone Miner. Res.* 2014 Jun;29(6):1392–401.
23. Liberman UA, Weiss SR, Broll J, Minne HW, Quan H, Bell NH, Rodriguez-portales JA, Downs RW, Dequeker J, Favus MJ, Seeman E, Recker RR, Capizzi T, Santora AC, Lombardi A, Shah R V., Hirsch LJ, Karpf DB. Effect of Oral Alendronate on Bone Mineral Density and the Incidence of Fractures in Postmenopausal Osteoporosis. *N. Engl. J. Med.* 1995;333(22):1437–43.

24. Kim G, Boskey AL, Baker SP, van der Meulen MCH. Improved prediction of rat cortical bone mechanical behavior using composite beam theory to integrate tissue level properties. *J. Biomech.* 2012 Nov 15;45(16):2784–90.
25. Andrews JC, Almeida E, van der Meulen MCH, Alwood JS, Lee C, Liu Y, Chen J, Meirer F, Feser M, Gelb J, Rudati J, Tkachuk A, Yun W, Pianetta P. Nanoscale X-ray microscopic imaging of mammalian mineralized tissue. *Microsc. Microanal.* 2010 Jun;16:327–36.

Chapter 7

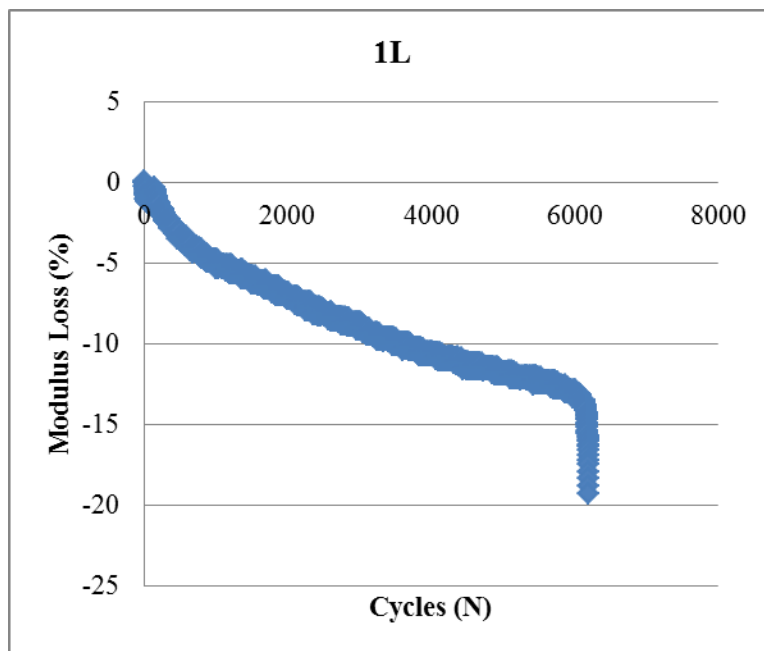
Appendix A: Chapter 3 Data

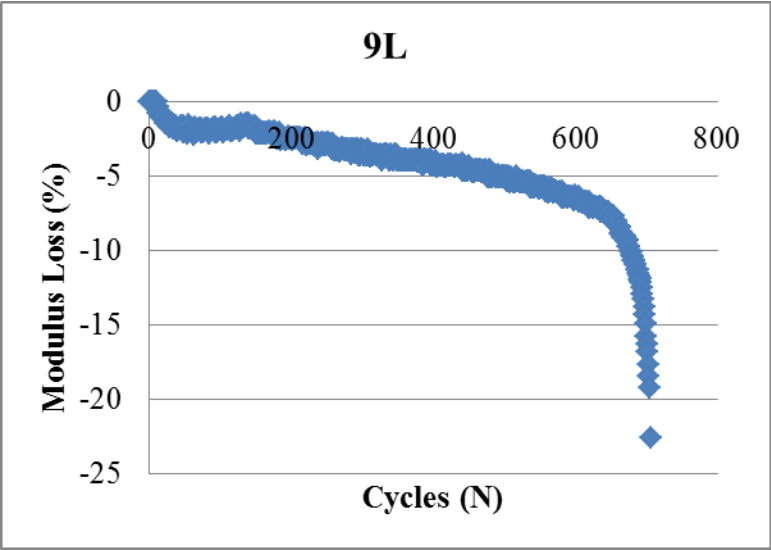
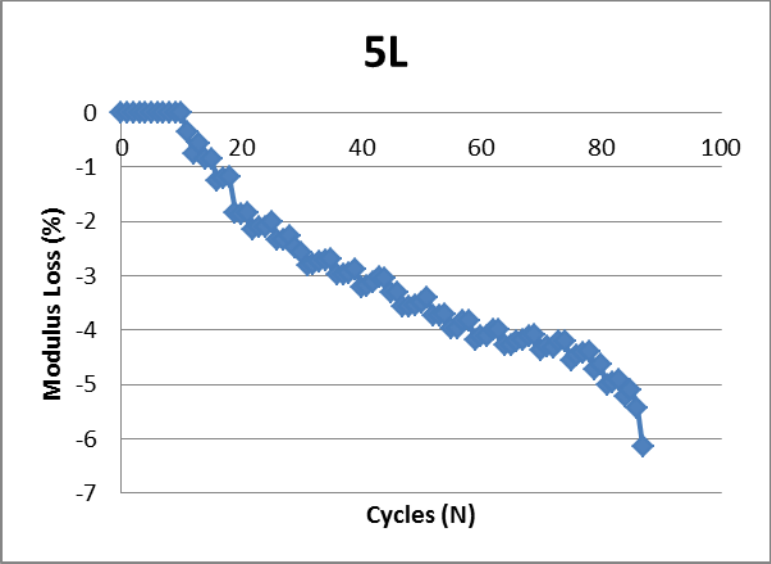
Below are the final overall results for the Bisphosphonate and PTH data:

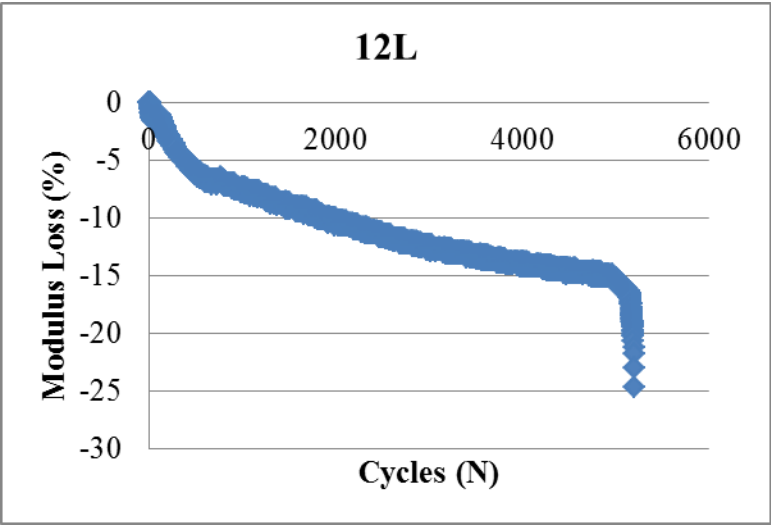
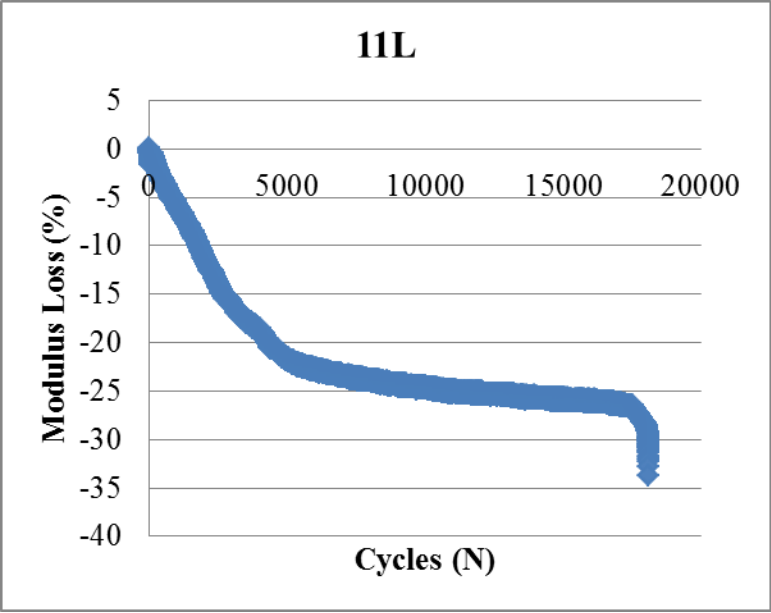
Sample ID	Group	Initial Modulus (Gpa)	Cycles to failure (N)	Modulus Loss at Failure	TMD (mg/cc)	Log of Cycles to Failure
11L	MA1	22.75	18103	33.7	897.8905	4.257751
12L	RAL	22.03	5195	24.62	1106.007	3.715586
13L	MA1	18.55	6537	32.79	968.9422	3.815378
19L	RAL	22.32	1003	23.35	1151.225	3.001301
1L	MA1	22.92	6203	19.97	923.0781	3.792602
5L	ALN	23.97	87	6.15	975.319	1.939519
9L	ALN	23.38	706	22.55	1028.8	2.848805
C10R	C	24.86	630	16.7	968.4504	2.799341
C1L	C	24.17	2094	22.97	923.0703	3.320977
C2L	C	23.72	3311	21.97	872.495	3.519959
C4R	C	21.62	10509	25.69	890.9542	4.021561
C5R	C	22.5	3218	18.05	746.8194	3.507586
C7R	C	16.46	22052	26.26	1155.35	4.343448
JM10L	ZOL	18.09	3824	23.81	1080.893	3.582518
JM12L	MA2	16.38	11693	20.88	1017.789	4.067926
JM13L	MA2	22.71	1212	18.94	1104.849	3.083503
JM1L	ZOL	23.15	17070	29.5	1025.573	4.232234
JM2L	MA2	18.53	25459	23.75	1116.544	4.405841
JM3L	ZOL	23.58	3486	14.74	997.5657	3.542327
JM4L	MA2	20.57	2385	36.55	858.2776	3.377488
JM5L	ZOL	23.32	764	21.94	1070.195	2.883093
JM6L	MA2	22.56	524	16.52	1103.401	2.719331
JM7L	ZOL	24.23	11492	32.59	1115.858	4.060396
JM8L	ZOL	22.25	5697	25.12	1036.113	3.755646
JM9L	MA2	22.96	1097	24.13	1058.07	3.040207
3049 (5209410)	MA3+OVX	29.59	9629	34.27	992.82	3.983581
3085 (5209310)	PTH	28.26	1908	15.29	1073.13	3.280578
3080 (5217610)	PTH	27.26	45447	37.31	1003.85	4.657505
No Tag (5209810)	MA3+OVX	29.5	2390	17.42	1150.11	3.378398
3048 (5217910)	PTH	28.01	23819	38.45	1025.72	4.376924
3089 (5217710)	MA3+OVX	31.29	1338	18.87	998.08	3.126456

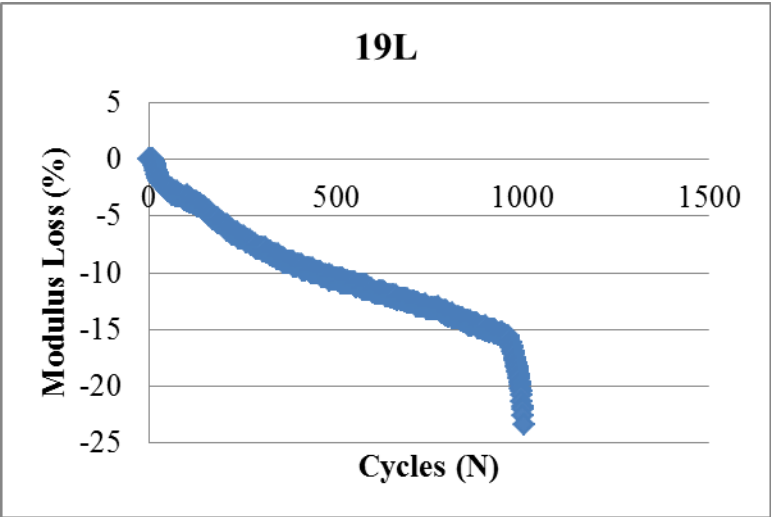
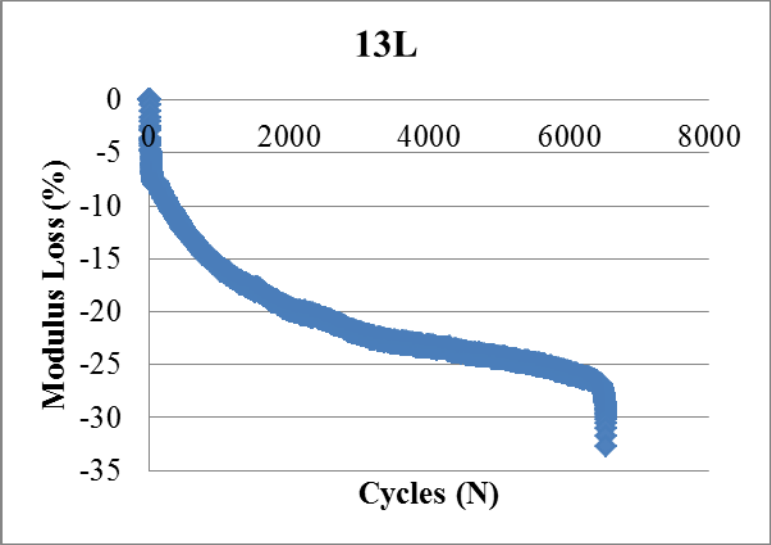
3072 (5209510)	PTH	24.44	47314	27.94	970.33	4.67499
3076 (5209710)	PTH	30.36	11159	20.58	938.34	4.047625
3073 (5217510)	MA3+OVX	25.86	31351		1001.84	4.496251
3078 (5209210)	MA3+OVX	26.5	4270	14.89	1020.4	3.630428
3086 (5217810)	PTH	24.79	31501	26.3	1048.28	4.498324
2339 (5209610)	MA3+OVX	21.04	22006	23.49	1091.91	4.342541

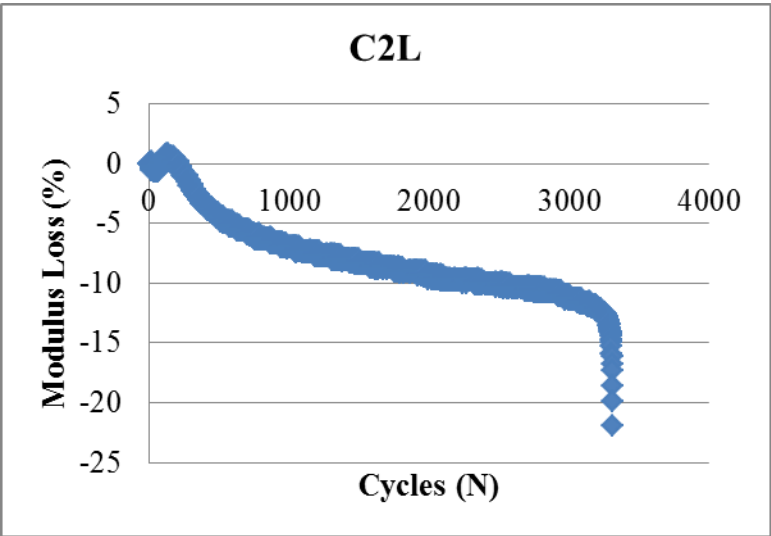
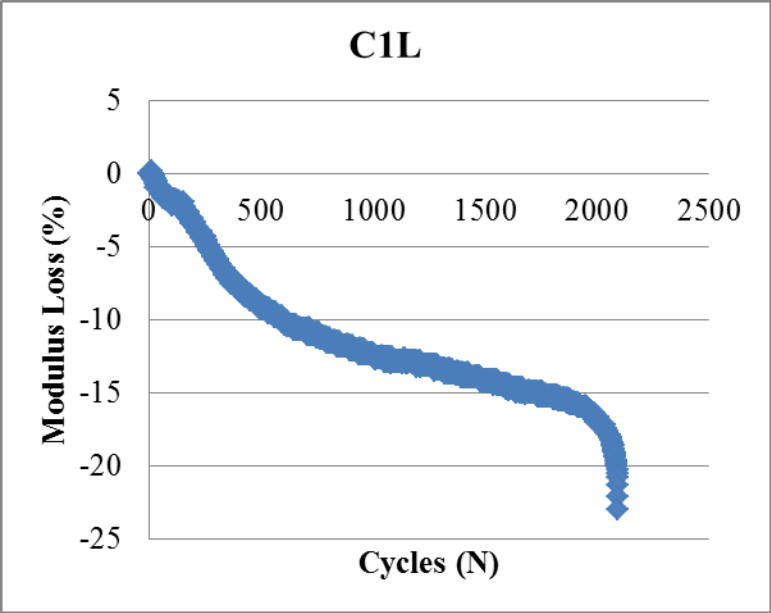
Below are the Modulus Loss by Cycles fatigue curves for the Bisphosphonate data. Curves for the PTH data were calculated by Julia Chen.

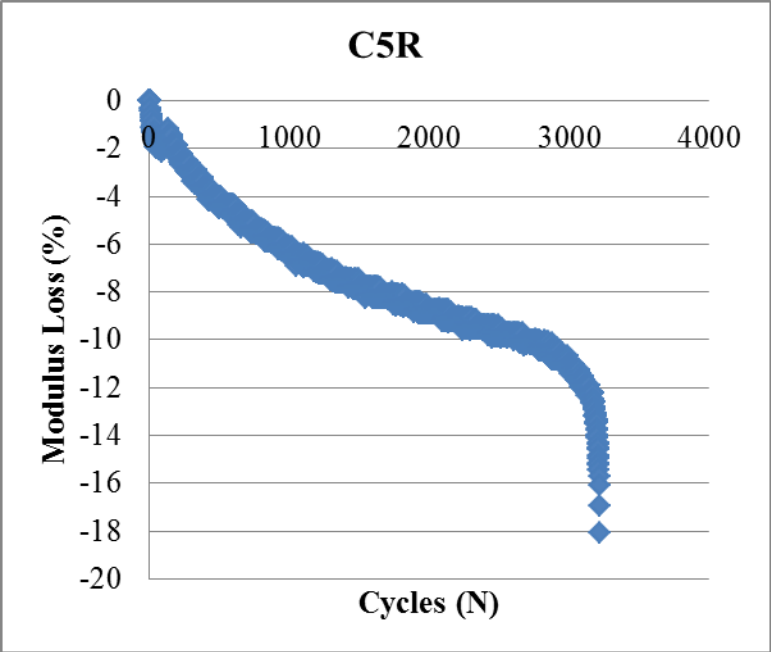
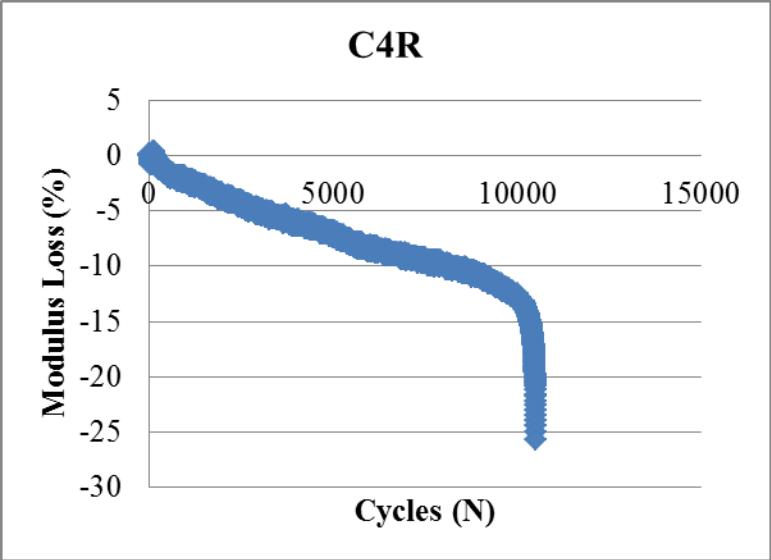


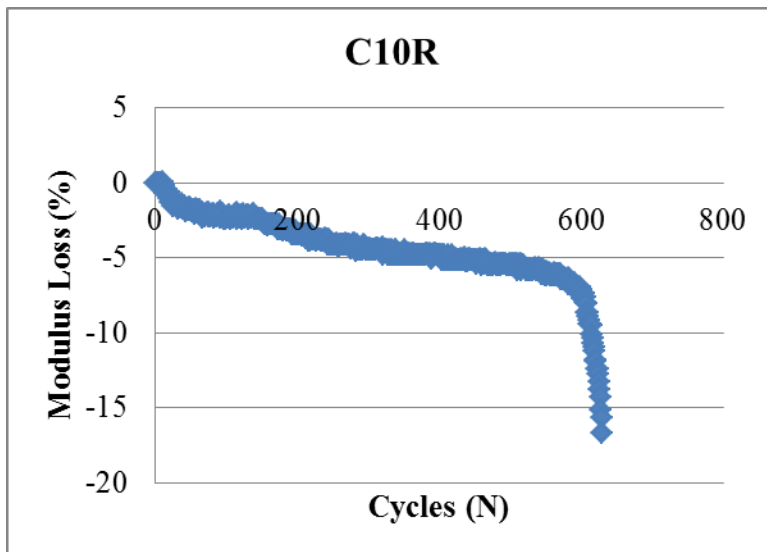
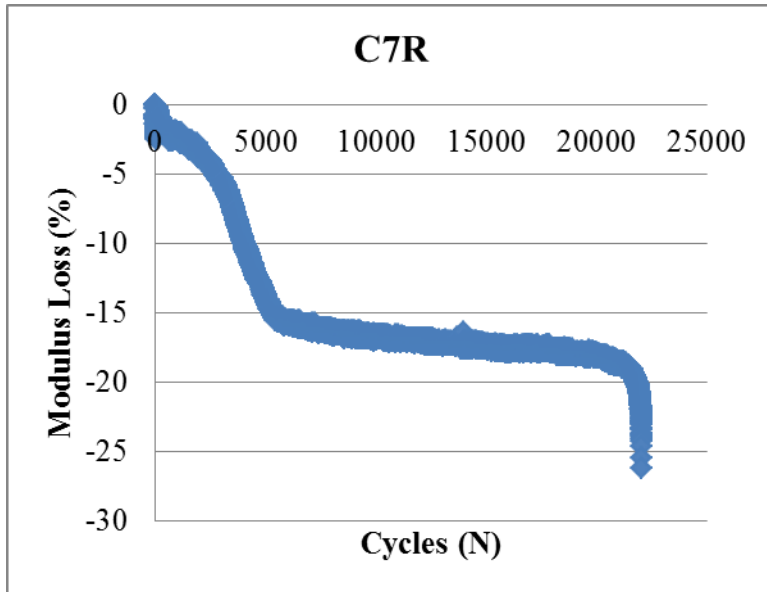


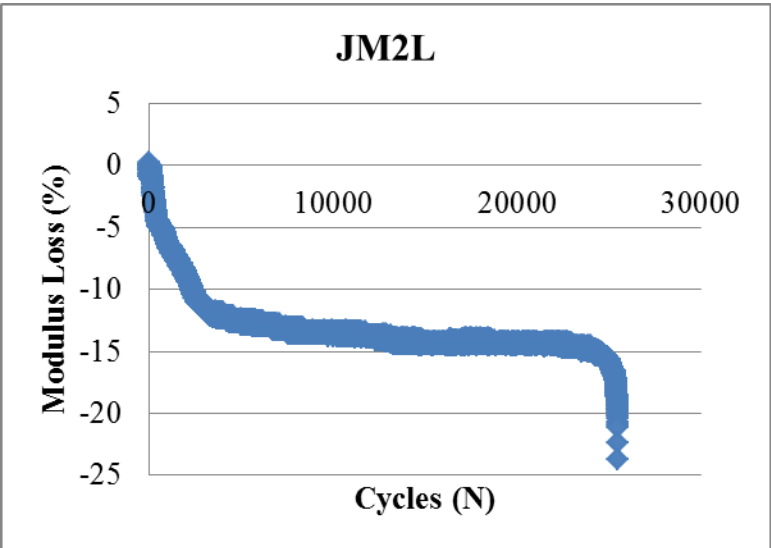
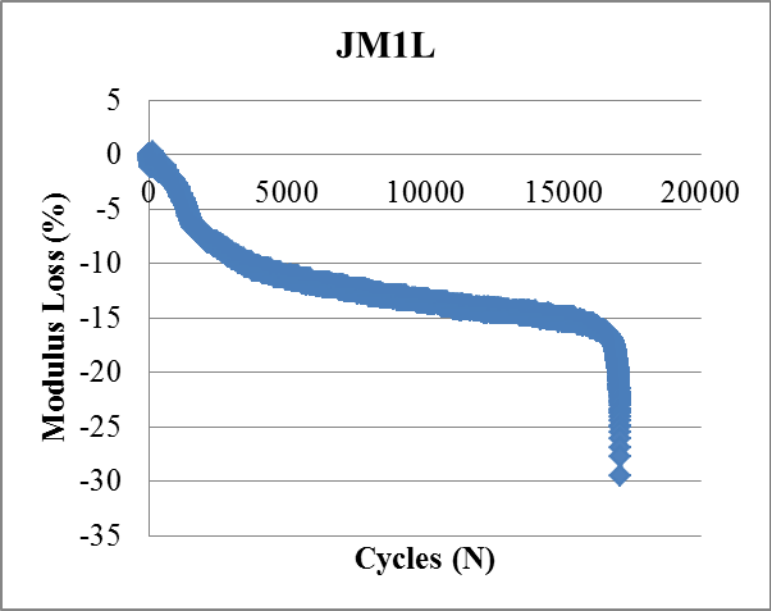


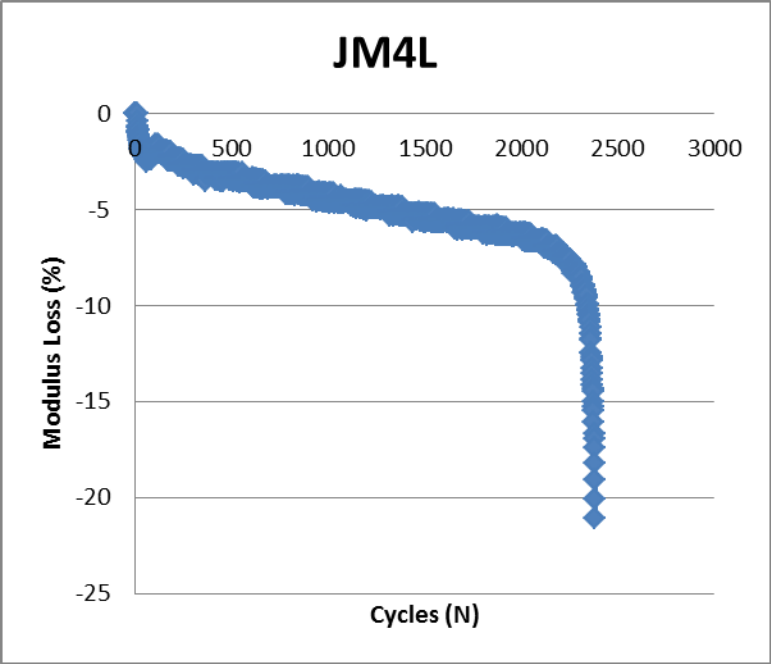
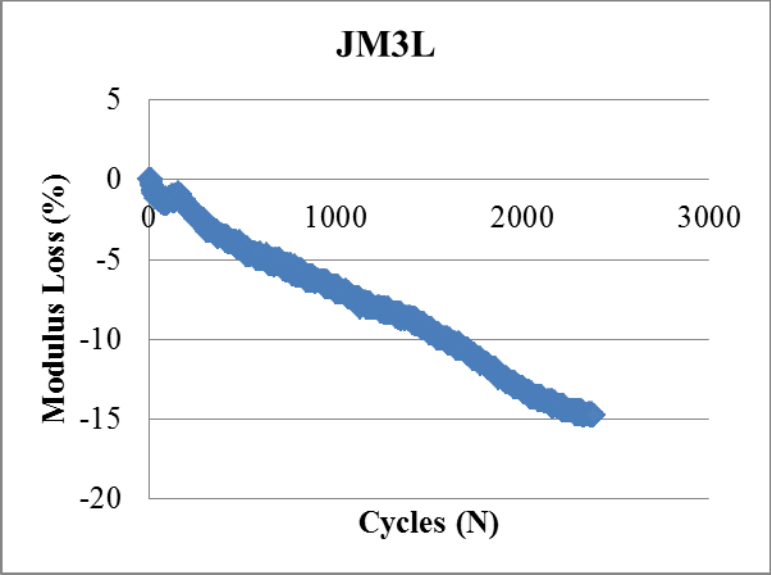


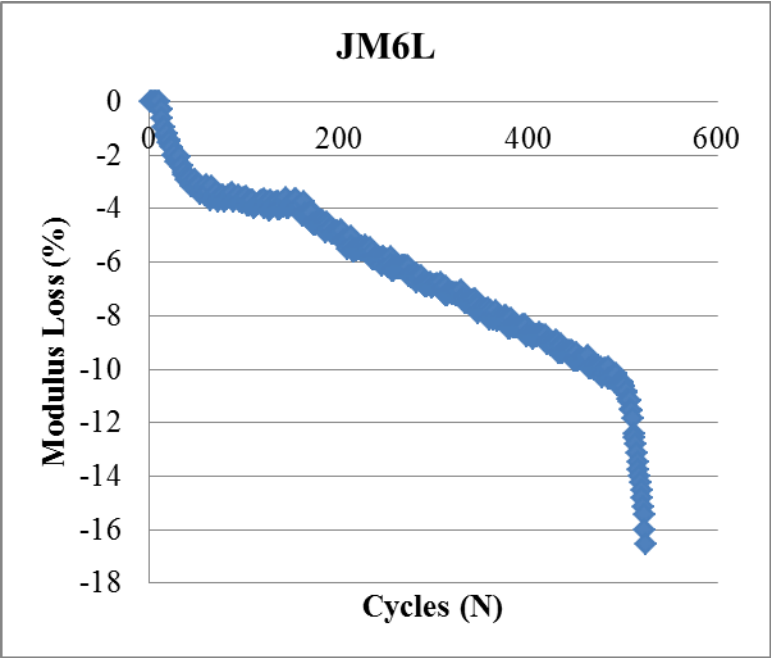
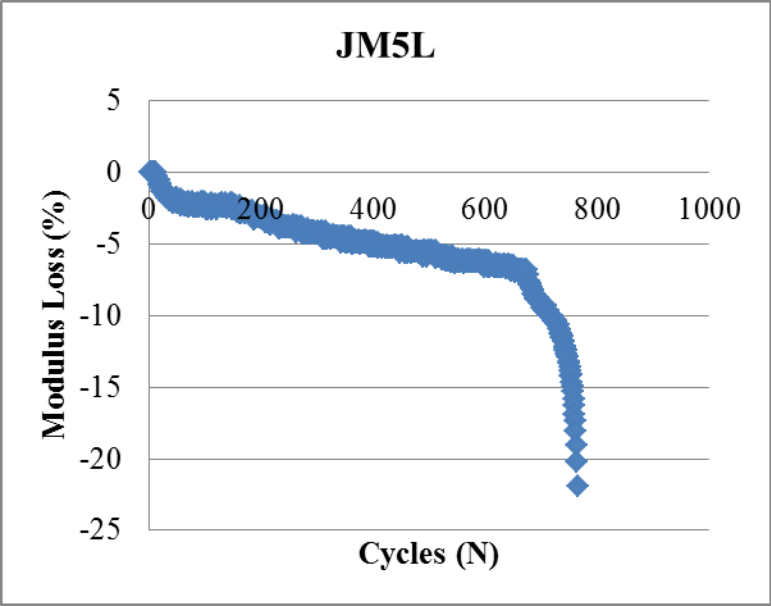


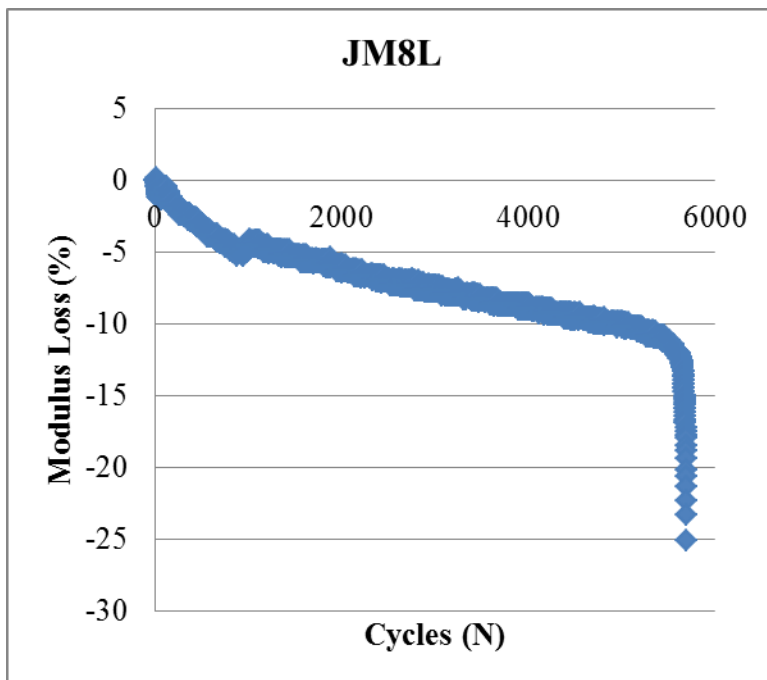
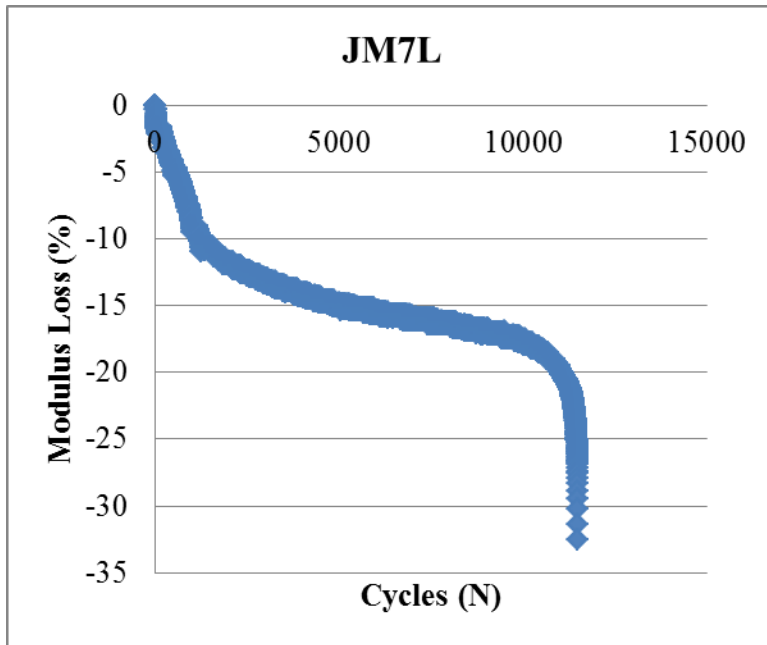


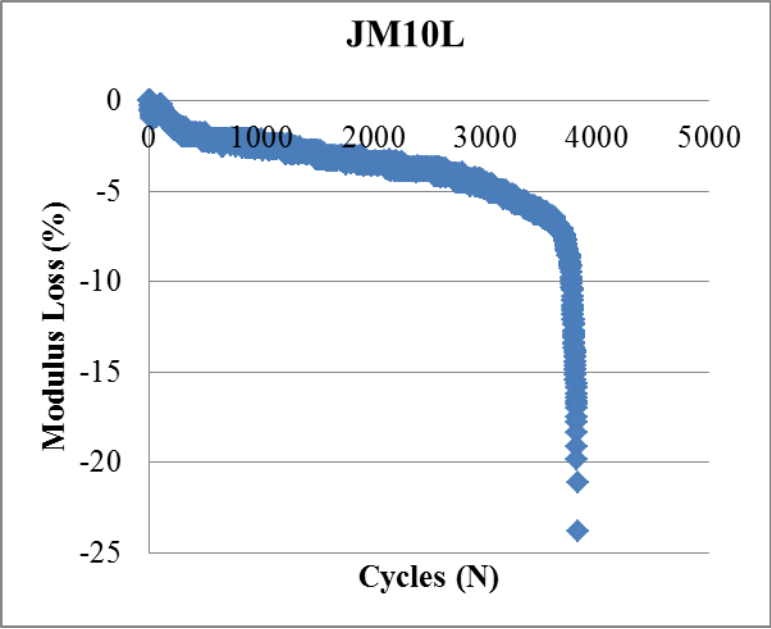
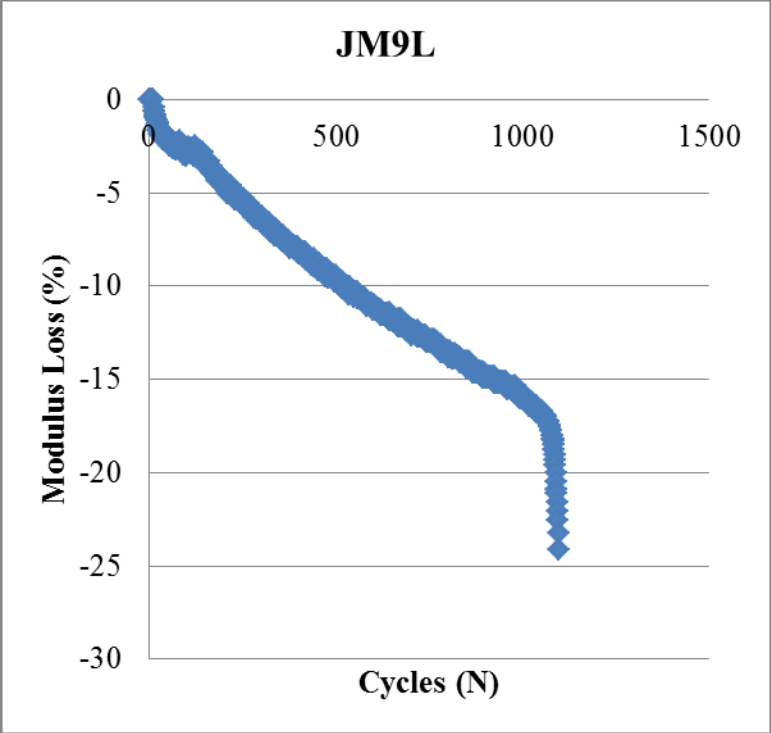


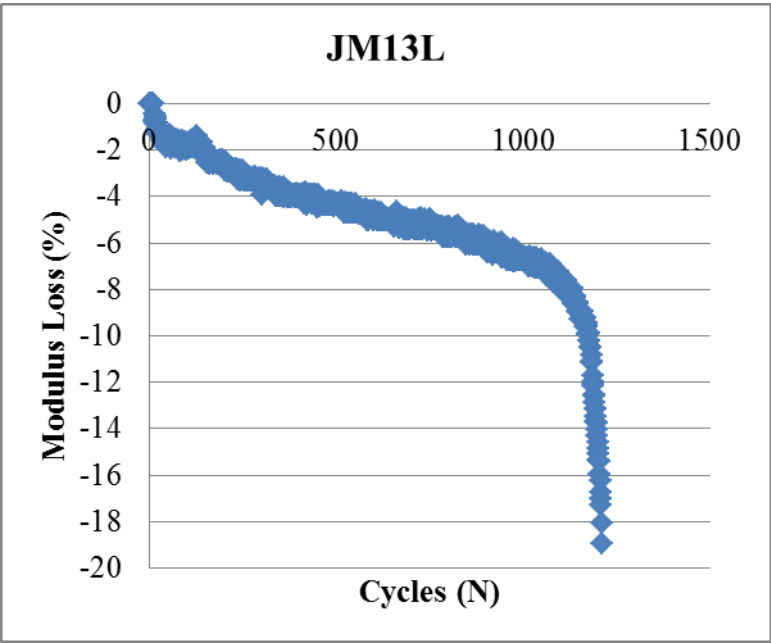
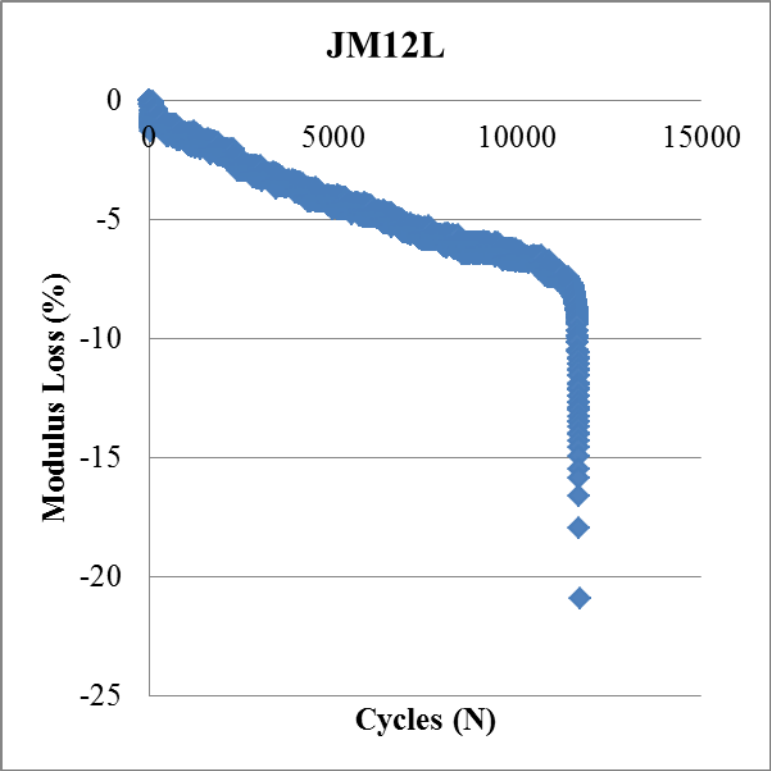












Chapter 8

Appendix B: Chapter 4 Data

Below is the group assignments for the samples measured:

Filenname	Test Type	Group	Loading
MedianAvg_000001_1L_Trans_C_angle_001_X_001_Y_001_01of03.xrm.bim.bim.bin	F	MA1	E
MedianAvg_000001_1L_Trans_NA_angle_001_X_001_Y_001_01of03.xrm.bim.bim.bin	F	MA1	NA
MedianAvg_000001_1L_Trans_T_angle_001_X_001_Y_001_01of03.xrm.bim.bim.bin	F	MA1	E
MedianAvg_000001_5L_Long_C_angle_001_X_001_Y_001_01of03.xrm.bim.bim.bin	F	ALE	E
MedianAvg_000001_5L_Long_NA_angle_001_X_001_Y_001_01of03.xrm.bim.bim.bin	F	ALE	NA
MedianAvg_000001_5L_Long_T_angle_001_X_001_Y_001_01of03.xrm.bim.bim.bin	F	ALE	E
MedianAvg_000001_9L_Long_C_angle_001_X_001_Y_001_01of03.xrm.bim.bim.bin	F	ALE	E
MedianAvg_000001_9L_Long_NA_angle_001_X_001_Y_001_01of03.xrm.bim.bim.bin	F	ALE	NA
MedianAvg_000001_9L_Long_T_angle_001_X_001_Y_001_01of03.xrm.bim.bim.bin	F	ALE	E
MedianAvg_000001_9L_Trans_C_angle_001_X_001_Y_001_01of03.xrm.bim.bim.bin	F	ALE	E
MedianAvg_000001_9L_Trans_C_Corner_CrossHatch_angle_001_X_001_Y_001_01of03.xrm.bim.bim.bin	F	ALE	E
MedianAvg_000001_9L_Trans_NA_angle_001_X_001_Y_001_01of03.xrm.bim.bim.bin	F	ALE	NA
MedianAvg_000001_9L_Trans_T_angle_001_X_001_Y_001_01of03.xrm.bim.bim.bin	F	ALE	E
MedianAvg_000001_9L_Trans_T_Possible_Crack_angle_001_X_001_Y_001_01of03.xrm.bim.bim.bin	F	ALE	E
MedianAvg_000001_11L_Long_C_angle_001_X_001_Y_001_01of03.xrm.bim.bim.bin	F	MA1	E
MedianAvg_000001_11L_Long_NA_angle_001_X_001_Y_001_01of03.xrm.bim.bim.bin	F	MA1	NA
MedianAvg_000001_11L_Long_T_angle_001_X_001_Y_001_01of03.xrm.bim.bim.bin	F	MA1	E
MedianAvg_000001_11L_trans_C_angle_001_X_001_Y_001_01of03.xrm.bim.bim.bin	F	MA1	E
MedianAvg_000001_11L_trans_NA_angle_001_X_001_Y_001_01of03.xrm.bim.bim.bin	F	MA1	NA
MedianAvg_000001_11L_trans_T_angle_001_X_001_Y_001_01of03.xrm.bim.bim.bin	F	MA1	E
MedianAvg_000001_12L_Long_C_angle_001_X_001_Y_001_01of03.xrm.bim.bim.bin	F	RAL	E

MedianAvg_000001_12L_Long_NA_angle_001_X_001_Y_001_01of03.xrm.bim.bim.bin	F	RAL	NA
MedianAvg_000001_12L_Long_T_angle_001_X_001_Y_001_01of03.xrm.bim.bim.bin	F	RAL	E
MedianAvg_000001_13L_Long_C_angle_001_X_001_Y_001_01of03.xrm.bim.bim.bin	F	MA1	E
MedianAvg_000001_13L_Long_NA_angle_001_X_001_Y_001_01of03.xrm.bim.bim.bin	F	MA1	NA
MedianAvg_000001_13L_Long_T_angle_001_X_001_Y_001_01of03.xrm.bim.bim.bin	F	MA1	E
MedianAvg_000001_13L_Trans_C_angle_001_X_001_Y_001_01of03.xrm.bim.bim.bin	F	MA1	E
MedianAvg_000001_13L_Trans_NA_angle_001_X_001_Y_001_01of03.xrm.bim.bim.bin	F	MA1	NA
MedianAvg_000001_13L_Trans_T_angle_001_X_001_Y_001_01of03.xrm.bim.bim.bin	F	MA1	E
MedianAvg_000001_15L_Long_C_angle_001_X_001_Y_001_01of03.xrm.bim.bim.bin	F	MA1	E
MedianAvg_000001_15L_Long_NA_angle_001_X_001_Y_001_01of03.xrm.bim.bim.bin	F	MA1	NA
MedianAvg_000001_15L_Long_T_angle_001_X_001_Y_001_01of03.xrm.bim.bim.bin	F	MA1	E
MedianAvg_000001_15L_trans_C_angle_001_X_001_Y_001_01of03.xrm.bim.bim.bin	F	MA1	E
MedianAvg_000001_15L_trans_NA_angle_001_X_001_Y_001_01of03.xrm.bim.bim.bin	F	MA1	NA
MedianAvg_000001_15L_trans_T_angle_001_X_001_Y_001_01of03.xrm.bim.bim.bin	F	MA1	E
MedianAvg_000001_16L_Long_Compressive_angle_001_X_001_Y_001_01of03.xrm.bim.bim.bin	F	RAL	E
MedianAvg_000001_16L_Long_NA_angle_001_X_001_Y_001_01of03.xrm.bim.bim.bin	F	RAL	NA
MedianAvg_000001_16L_Long_Tensile_angle_001_X_001_Y_001_01of03.xrm.bim.bim.bin	F	RAL	E
MedianAvg_000001_16L_Trans_C_angle_001_X_001_Y_001_01of03.xrm.bim.bim.bin	F	RAL	E
MedianAvg_000001_16L_Trans_NA_angle_001_X_001_Y_001_01of03.xrm.bim.bim.bin	F	RAL	NA
MedianAvg_000001_16L_Trans_T_angle_001_X_001_Y_001_01of03.xrm.bim.bim.bin	F	RAL	E
MedianAvg_000001_18L_Trans_C_angle_001_X_001_Y_001_01of03.xrm.bim.bim.bin	F	RAL	E
MedianAvg_000001_18L_Trans_NA_angle_001_X_001_Y_001_01of03.xrm.bim.bim.bin	F	RAL	NA
MedianAvg_000001_18L_Trans_T_angle_001_X_001_Y_001_01of03.xrm.bim.bim.bin	F	RAL	E
MedianAvg_000001_19L_Trans_C_angle_001_X_001_Y_001_01of03.xrm.bim.bim.bin	F	RAL	E
MedianAvg_000001_19L_Trans_NA_angle_001_X_001_Y_001_01of03.xrm.bim.bim.bin	F	RAL	NA
MedianAvg_000001_19L_Trans_T_angle_001_X_001_Y_001_01of03.xrm.bim.bim.bin	F	RAL	E
MedianAvg_000001_20120217_JM2_long_C_angle_001_X_001_Y_001	F	MA2	E

_01of03.xrm.bim.bim.bin			
MedianAvg_000001_20120217_JM2_long_NA_angle_001_X_001_Y_001_01of03.xrm.bim.bim.bin	F	MA2	NA
MedianAvg_000001_20120217_JM2_long_T_angle_001_X_001_Y_001_01of03.xrm.bim.bim.bin	F	MA2	E
MedianAvg_000001_20120218_JM6_long_C_angle_001_X_001_Y_001_01of03.xrm.bim.bim.bin	F	MA2	E
MedianAvg_000001_20120218_JM6_long_NA_angle_001_X_001_Y_001_01of03.xrm.bim.bim.bin	F	MA2	NA
MedianAvg_000001_20120218_JM6_long_T_angle_001_X_001_Y_001_01of03.xrm.bim.bim.bin	F	MA2	E
MedianAvg_000001_20120218_JM7_long_L_angle_001_X_001_Y_001_01of03.xrm.bim.bim.bin	F	ZOL	E
MedianAvg_000001_20120218_JM7_long_R_angle_001_X_001_Y_001_01of03.xrm.bim.bim.bin	F	ZOL	E
MedianAvg_000001_20120218_JM9_long_C_angle_001_X_001_Y_001_01of03.xrm.bim.bim.bin	F	MA2	NA
MedianAvg_000001_20120218_JM9_long_C2_angle_001_X_001_Y_001_01of03.xrm.bim.bim.bin	F	MA2	E
MedianAvg_000001_20120218_JM9_long_NA_angle_001_X_001_Y_001_01of03.xrm.bim.bim.bin	F	MA2	NA
MedianAvg_000001_20120218_JM9_long_T1_angle_001_X_001_Y_001_01of03.xrm.bim.bim.bin	F	MA2	E
MedianAvg_000001_20120218_JM9_long_T2_angle_001_X_001_Y_001_01of03.xrm.bim.bim.bin	F	MA2	E
MedianAvg_000001_20120219_C7R_long_C1_angle_001_X_001_Y_001_01of03.xrm.bim.bim.bin	F	C	E
MedianAvg_000001_C1L_Trans_C_angle_001_X_001_Y_001_01of03.xrm.bim.bim.bin	F	C	E
MedianAvg_000001_C1L_Trans_NA_angle_001_X_001_Y_001_01of03.xrm.bim.bim.bin	F	C	NA
MedianAvg_000001_C1L_Trans_T_angle_001_X_001_Y_001_01of03.xrm.bim.bim.bin	F	C	E
MedianAvg_000001_C2L_Long_C_angle_001_X_001_Y_001_01of03.xrm.bim.bim.bin	F	C	E
MedianAvg_000001_C2L_Long_NA_angle_001_X_001_Y_001_01of03.xrm.bim.bim.bin	F	C	NA
MedianAvg_000001_C2L_Long_T_angle_001_X_001_Y_001_01of03.xrm.bim.bim.bin	F	C	E
MedianAvg_000001_C4R_long_C_angle_001_X_001_Y_001_01of03.xrm.bim.bim.bin	F	C	E
MedianAvg_000001_C4R_long_NA_angle_001_X_001_Y_001_01of03.xrm.bim.bim.bin	F	C	NA
MedianAvg_000001_C4R_long_T_angle_001_X_001_Y_001_01of03.xrm.bim.bim.bin	F	C	E
MedianAvg_000001_C4r_trans_C_angle_001_X_001_Y_001_01of03.xrm.bim.bim.bin	F	C	E
MedianAvg_000001_C4r_trans_T_angle_001_X_001_Y_001_01of03.xrm.bim.bim.bin	F	C	E
MedianAvg_000001_C10_Trans_Again_C_angle_001_X_001_Y_001_01of03.xrm.bim.bim.bin	F	C	E
MedianAvg_000001_C10_Trans_Again_NA_angle_001_X_001_Y_001_01of03.xrm.bim.bim.bin	F	C	NA

MedianAvg_000001_C10_Trans_Again_T_angle_001_X_001_Y_001_01of03.xrm.bim.bim.bin	F	C	E
MedianAvg_000001_C10R_long_C_angle_001_X_001_Y_001_01of03.xrm.bim.bim.bin	F	C	E
MedianAvg_000001_C10R_long_NA_angle_001_X_001_Y_001_01of03.xrm.bim.bim.bin	F	C	NA
MedianAvg_000001_C10R_long_T_angle_001_X_001_Y_001_01of03.xrm.bim.bim.bin	F	C	E
MedianAvg_000001_JM1_Long_C_angle_001_X_001_Y_001_01of03.xrm.bim.bim.bin	F	ZOL	E
MedianAvg_000001_JM1_Long_NA_angle_001_X_001_Y_001_01of03.xrm.bim.bim.bin	F	ZOL	NA
MedianAvg_000001_JM1_Long_T_angle_001_X_001_Y_001_01of03.xrm.bim.bim.bin	F	ZOL	E
MedianAvg_000001_JM1_trans_C_angle_001_X_001_Y_001_01of03.xrm.bim.bim.bin	F	ZOL	E
MedianAvg_000001_JM1_trans_NA_angle_001_X_001_Y_001_01of03.xrm.bim.bim.bin	F	ZOL	NA
MedianAvg_000001_JM1_trans_T_angle_001_X_001_Y_001_01of03.xrm.bim.bim.bin	F	ZOL	E
MedianAvg_000001_JM2_Trans_C_angle_001_X_001_Y_001_01of03.xrm.bim.bim.bin	F	MA2	E
MedianAvg_000001_JM2_Trans_NA_angle_001_X_001_Y_001_01of03.xrm.bim.bim.bin	F	MA2	NA
MedianAvg_000001_JM2_Trans_T_angle_001_X_001_Y_001_01of03.xrm.bim.bim.bin	F	MA2	E
MedianAvg_000001_JM3_trans_C_angle_001_X_001_Y_001_01of03.xrm.bim.bim.bin	F	ZOL	E
MedianAvg_000001_JM3_trans_NA_angle_001_X_001_Y_001_01of03.xrm.bim.bim.bin	F	ZOL	NA
MedianAvg_000001_JM3_trans_T_angle_001_X_001_Y_001_01of03.xrm.bim.bim.bin	F	ZOL	E
MedianAvg_000001_Jm4_long_C_angle_001_X_001_Y_001_01of03.xrm.bim.bim.bin	F	MA2	E
MedianAvg_000001_Jm4_long_NA_angle_001_X_001_Y_001_01of03.xrm.bim.bim.bin	F	MA2	NA
MedianAvg_000001_Jm4_long_T_angle_001_X_001_Y_001_01of03.xrm.bim.bim.bin	F	MA2	E
MedianAvg_000001_Jm4_trans_C_angle_001_X_001_Y_001_01of03.xrm.bim.bim.bin	F	MA2	E
MedianAvg_000001_Jm4_trans_NA_angle_001_X_001_Y_001_01of03.xrm.bim.bim.bin	F	MA2	NA
MedianAvg_000001_Jm4_trans_T_angle_001_X_001_Y_001_01of03.xrm.bim.bim.bin	F	MA2	E
MedianAvg_000001_Jm5_Long_C_angle_001_X_001_Y_001_01of03.xrm.bim.bim.bin	F	ZOL	E
MedianAvg_000001_Jm5_Long_NA_angle_001_X_001_Y_001_01of03.xrm.bim.bim.bin	F	ZOL	NA
MedianAvg_000001_Jm5_Long_T_angle_001_X_001_Y_001_01of03.xrm.bim.bim.bin	F	ZOL	E
MedianAvg_000001_Jm5_Trans_C_angle_001_X_001_Y_001_01of03.xrm.bim.bim.bin	F	ZOL	E
MedianAvg_000001_Jm5_Trans_NA_angle_001_X_001_Y_001_01of03.xrm.bim.bim.bin	F	ZOL	NA

.xrm.bim.bim.bin			
MedianAvg_000001_Jm5_Trans_T_angle_001_X_001_Y_001_01of03.xrm.bim.bim.bin	F	ZOL	E
MedianAvg_000001_Jm6_Trans_C_angle_001_X_001_Y_001_01of03.xrm.bim.bim.bin	F	MA2	E
MedianAvg_000001_Jm6_Trans_NA_angle_001_X_001_Y_001_01of03.xrm.bim.bim.bin	F	MA2	NA
MedianAvg_000001_Jm6_Trans_T_angle_001_X_001_Y_001_01of03.xrm.bim.bim.bin	F	MA2	E
MedianAvg_000001_JM7_Trans_C_angle_000_X_001_Y_001_01of03.xrm.bim.bim.bin	F	ZOL	E
MedianAvg_000001_JM7_Trans_NA_angle_001_X_001_Y_001_01of03.xrm.bim.bim.bin	F	ZOL	NA
MedianAvg_000001_JM7_Trans_T_angle_001_X_001_Y_001_01of03.xrm.bim.bim.bin	F	ZOL	E
MedianAvg_000001_JM8_Long_C_angle_001_X_001_Y_001_01of03.xrm.bim.bim.bin	F	ZOL	E
MedianAvg_000001_JM8_Long_NA_angle_001_X_001_Y_001_01of03.xrm.bim.bim.bin	F	ZOL	NA
MedianAvg_000001_JM8_Long_T_angle_001_X_001_Y_001_01of03.xrm.bim.bim.bin	F	ZOL	E
MedianAvg_000001_JM8_Trans_C_angle_000_X_001_Y_001_01of03.xrm.bim.bim.bin	F	ZOL	E
MedianAvg_000001_JM8_Trans_NA_angle_001_X_001_Y_001_01of03.xrm.bim.bim.bin	F	ZOL	NA
MedianAvg_000001_JM8_Trans_T_angle_001_X_001_Y_001_01of03.xrm.bim.bim.bin	F	ZOL	E
MedianAvg_000001_JM9_Trans_C_angle_001_X_001_Y_001_01of03.xrm.bim.bim.bin	F	MA2	E
MedianAvg_000001_JM9_Trans_NA_angle_001_X_001_Y_001_01of03.xrm.bim.bim.bin	F	MA2	NA
MedianAvg_000001_JM9_Trans_T_angle_001_X_001_Y_001_01of03.xrm.bim.bim.bin	F	MA2	E
MedianAvg_000001_JM10_Long_C_angle_001_X_001_Y_001_01of03.xrm.bim.bim.bin	F	ZOL	E
MedianAvg_000001_JM10_Long_NA_angle_001_X_001_Y_001_01of03.xrm.bim.bim.bin	F	ZOL	NA
MedianAvg_000001_JM10_Long_T_angle_001_X_001_Y_001_01of03.xrm.bim.bim.bin	F	ZOL	E
MedianAvg_000001_JM10_Trans_C_angle_000_X_001_Y_001_01of03.xrm.bim.bim.bin	F	ZOL	E
MedianAvg_000001_JM10_Trans_NA_angle_000_X_001_Y_001_01of03.xrm.bim.bim.bin	F	ZOL	NA
MedianAvg_000001_JM10_Trans_T_angle_000_X_001_Y_001_01of03.xrm.bim.bim.bin	F	ZOL	E
MedianAvg_000001_JM12_Long_C_angle_001_X_001_Y_001_01of03.xrm.bim.bim.bin	F	MA2	E
MedianAvg_000001_JM12_Long_NA_angle_001_X_001_Y_001_01of03.xrm.bim.bim.bin	F	MA2	NA
MedianAvg_000001_JM12_Long_T_angle_001_X_001_Y_001_01of03.xrm.bim.bim.bin	F	MA2	E
MedianAvg_000001_JM12_Trans_C_angle_001_X_001_Y_001_01of03.xrm.bim.bim.bin	F	MA2	E

MedianAvg_000001_JM12_Trans_NA_angle_001_X_001_Y_001_01of03.xrm.bim.bim.bin	F	MA2	NA
MedianAvg_000001_JM12_Trans_T_angle_001_X_001_Y_001_01of03.xrm.bim.bim.bin	F	MA2	E
MedianAvg_000001_JM13_Trans_NA_angle_001_X_001_Y_001_01of03.xrm.bim.bim.bin	F	MA2	NA
MedianAvg_000001_JM13_Trans_T_angle_001_X_001_Y_001_01of03.xrm.bim.bim.bin	F	MA2	E
000001_1UA_1_angle_-05_X_001_Y_001_01of01.xrm.bim.bin	M	MA1	E
000001_1UA_2_angle_-05_X_001_Y_001_01of01.xrm.bim.bin	M	MA1	E
000001_1UA_3_angle_-05_X_001_Y_001_01of01.xrm.bim.bin	M	MA1	E
000001_1UA_4_angle_-05_X_001_Y_001_01of01.xrm.bim.bin	M	MA1	E
000001_1UA_5_angle_-05_X_001_Y_001_01of01.xrm.bim.bin	M	MA1	E
000001_1UA_6_angle_-05_X_001_Y_001_01of01.xrm.bim.bin	M	MA1	E
000001_1UA_7_angle_-05_X_001_Y_001_01of01.xrm.bim.bin	M	MA1	NA
000001_2UA_2_angle_-05_X_001_Y_001_01of01.xrm.bim.bin	M	ALE	E
000001_2UA_3_angle_-05_X_001_Y_001_01of01.xrm.bim.bin	M	ALE	E
000001_2UA_4_angle_-05_X_001_Y_001_01of01.xrm.bim.bin	M	ALE	E
000001_2UA_5_angle_-05_X_001_Y_001_01of01.xrm.bim.bin	M	ALE	E
000001_2UA_7_angle_-05_X_001_Y_001_01of01.xrm.bim.bin	M	ALE	NA
000001_3UA_1_angle_-05_X_001_Y_001_01of01.xrm.bim.bin	M	ALE	E
000001_3UA_2_angle_000_X_001_Y_001_01of01.xrm.bim.bin	M	ALE	E
000001_3UA_3_angle_000_X_001_Y_001_01of01.xrm.bim.bin	M	ALE	E
000001_3UA_4_angle_000_X_001_Y_001_01of01.xrm.bim.bin	M	ALE	E
000001_3UA_5_angle_000_X_001_Y_001_01of01.xrm.bim.bin	M	ALE	E
000001_3UA_6_angle_000_X_001_Y_001_01of01.xrm.bim.bin	M	ALE	E
000001_5UA_1_angle_-03_X_001_Y_001_01of01.xrm.bim.bin	M	RAL	E
000001_5UA_2_angle_-03_X_001_Y_001_01of01.xrm.bim.bin	M	RAL	E
000001_5UA_3_angle_-03_X_001_Y_001_01of01.xrm.bim.bin	M	RAL	E
000001_5UA_4_angle_-03_X_001_Y_001_01of01.xrm.bim.bin	M	RAL	E
000001_5UA_5_angle_-03_X_001_Y_001_01of01.xrm.bim.bin	M	RAL	E
000001_5UA_6_angle_-03_X_001_Y_001_01of01.xrm.bim.bin	M	RAL	E
000001_5UA_7_angle_-03_X_001_Y_001_01of01.xrm.bim.bin	M	RAL	NA
000001_5UA_8_angle_-03_X_001_Y_001_01of01.xrm.bim.bin	M	RAL	E
000001_6UA_1_angle_-06_X_001_Y_001_01of01.xrm.bim.bin	M	MA1	E
000001_6UA_2_angle_-06_X_001_Y_001_01of01.xrm.bim.bin	M	MA1	E
000001_6UA_3_angle_-06_X_001_Y_001_01of01.xrm.bim.bin	M	MA1	E
000001_6UA_4_angle_-06_X_001_Y_001_01of01.xrm.bim.bin	M	MA1	E
000001_6UA_5_angle_-06_X_001_Y_001_01of01.xrm.bim.bin	M	MA1	E
000001_6UA_6_angle_-06_X_001_Y_001_01of01.xrm.bim.bin	M	MA1	E
000001_6UA_7_angle_-06_X_001_Y_001_01of01.xrm.bim.bin	M	MA1	NA
000001_8AU_1_angle_-02_X_001_Y_001_01of01.xrm.bim.bin	M	RAL	E
000001_8UA_2_angle_000_X_001_Y_001_01of01.xrm.bim.bin	M	RAL	E
000001_8UA_3_angle_000_X_001_Y_001_01of01.xrm.bim.bin	M	RAL	E

000001_8UA_4_angle_000_X_001_Y_001_01of01.xrm.bim.bin	M	RAL	E
000001_8UA_6_angle_000_X_001_Y_001_01of01.xrm.bim.bin	M	RAL	E
000001_8UA_8_angle_000_X_001_Y_001_01of01.xrm.bim.bin	M	RAL	E
000001_9UA_1_angle_-06_X_001_Y_001_01of01.xrm.bim.bin	M	RAL	E
000001_9UA_2_angle_000_X_001_Y_001_01of01.xrm.bim.bin	M	RAL	E
000001_9UA_3_angle_000_X_001_Y_001_01of01.xrm.bim.bin	M	RAL	E
000001_9UA_4_angle_000_X_001_Y_001_01of01.xrm.bim.bin	M	RAL	NA
000001_9UA_5_angle_000_X_001_Y_001_01of01.xrm.bim.bin	M	RAL	E
000001_9UA_6_angle_000_X_001_Y_001_01of01.xrm.bim.bin	M	RAL	E
000001_13UA_1_angle_-07_X_001_Y_001_01of01.xrm.bim.bin	M	C	E
000001_13UA_2_angle_-07_X_001_Y_001_01of01.xrm.bim.bin	M	C	E
000001_13UA_3_angle_-07_X_001_Y_001_01of01.xrm.bim.bin	M	C	E
000001_13UA_4_angle_-07_X_001_Y_001_01of01.xrm.bim.bin	M	C	E
000001_13UA_5_angle_-07_X_001_Y_001_01of01.xrm.bim.bin	M	C	E
000001_13UA_6_angle_-07_X_001_Y_001_01of01.xrm.bim.bin	M	C	E
000001_13UA_7_angle_-07_X_001_Y_001_01of01.xrm.bim.bin	M	C	NA
000001_16UA_1_angle_-06_X_001_Y_001_01of01.xrm.bim.bin	M	ZOL	E
000001_16UA_2_angle_-06_X_001_Y_001_01of01.xrm.bim.bin	M	ZOL	E
000001_16UA_3_angle_-06_X_001_Y_001_01of01.xrm.bim.bin	M	ZOL	E
000001_16UA_4_angle_-06_X_001_Y_001_01of01.xrm.bim.bin	M	ZOL	E
000001_16UA_5_angle_-06_X_001_Y_001_01of01.xrm.bim.bin	M	ZOL	E
000001_16UA_6_angle_-06_X_001_Y_001_01of01.xrm.bim.bin	M	ZOL	E
000001_16UA_7_angle_-06_X_001_Y_001_01of01.xrm.bim.bin	M	ZOL	NA
000001_18UA_1_angle_-05_X_001_Y_001_01of01.xrm.bim.bin	M	MA2	E
000001_18UA_2_angle_-05_X_001_Y_001_01of01.xrm.bim.bin	M	MA2	E
000001_18UA_3_angle_-05_X_001_Y_001_01of01.xrm.bim.bin	M	MA2	E
000001_18UA_4_angle_-05_X_001_Y_001_01of01.xrm.bim.bin	M	MA2	E
000001_18UA_5_angle_-05_X_001_Y_001_01of01.xrm.bim.bin	M	MA2	E
000001_18UA_6_angle_-05_X_001_Y_001_01of01.xrm.bim.bin	M	MA2	E
000001_18UA_7_angle_-05_X_001_Y_001_01of01.xrm.bim.bin	M	MA2	NA
000001_20UA_1_angle_-10_X_001_Y_001_01of01.xrm.bim.bin	M	ZOL	E
000001_20UA_1_angle_-10_X_001_Y_001_01of01.xrm.bin	M	ZOL	E
000001_20UA_2_angle_000_X_001_Y_001_01of01.xrm.bim.bin	M	ZOL	E
000001_20UA_3_angle_000_X_001_Y_001_01of01.xrm.bim.bin	M	ZOL	E
000001_20UA_4_angle_000_X_001_Y_001_01of01.xrm.bim.bin	M	ZOL	E
000001_20UA_5_angle_000_X_001_Y_001_01of01.xrm.bim.bin	M	ZOL	E
000001_22UA_1_angle_-05_X_001_Y_001_01of01.xrm.bim.bin	M	ZOL	E
000001_22UA_2_angle_-05_X_001_Y_001_01of01.xrm.bim.bin	M	ZOL	E
000001_22UA_3_angle_-05_X_001_Y_001_01of01.xrm.bim.bin	M	ZOL	E
000001_22UA_4_angle_-05_X_001_Y_001_01of01.xrm.bim.bin	M	ZOL	E
000001_22UA_5_angle_-05_X_001_Y_001_01of01.xrm.bim.bin	M	ZOL	E
000001_22UA_6_angle_-05_X_001_Y_001_01of01.xrm.bim.bin	M	ZOL	E

000001_22UA_7_angle_-05_X_001_Y_001_01of01.xrm.bim.bin	M	ZOL	NA
000001_23UA_1_angle_-06_X_001_Y_001_01of01.xrm.bim.bin	M	MA2	E
000001_23UA_2_angle_-06_X_001_Y_001_01of01.xrm.bim.bin	M	MA2	E
000001_23UA_3_angle_-06_X_001_Y_001_01of01.xrm.bim.bin	M	MA2	E
000001_23UA_4_angle_-06_X_001_Y_001_01of01.xrm.bim.bin	M	MA2	E
000001_23UA_5_angle_-06_X_001_Y_001_01of01.xrm.bim.bin	M	MA2	E
000001_23UA_6_angle_-06_X_001_Y_001_01of01.xrm.bim.bin	M	MA2	E
000001_23UA_7_angle_-06_X_001_Y_001_01of01.xrm.bim.bin	M	MA2	NA
000074_2UA_1_angle_-05_X_004_Y_011_01of01.xrm.bim.bin	M	MA2	E

Results for total UA for samples above:

Filname	Mean	median	mode	Max	UA	UA/Bone
MedianAvg_000001_1L_Trans_C_angle_001_X_001_Y_001_01of03.xrm.bim.bin	0.863116	0.881199	2.22E-16	3.069344	2699265	0.010199
MedianAvg_000001_1L_Trans_NA_angle_001_X_001_Y_001_01of03.xrm.bim.bin	0.885903	0.923857	0.916291	2.788589	640153	0.002387
MedianAvg_000001_1L_Trans_T_angle_001_X_001_Y_001_01of03.xrm.bim.bin	0.919542	0.971097	2.22E-16	3.406959	2202335	0.008484
MedianAvg_000001_5L_Long_C_angle_001_X_001_Y_001_01of03.xrm.bim.bin	0.70574	0.756688	2.22E-16	2.533983	882841	0.003345
MedianAvg_000001_5L_Long_NA_angle_001_X_001_Y_001_01of03.xrm.bim.bin	0.710728	0.711247	0.693147	1.036647	27034	0.0001
MedianAvg_000001_5L_Long_T_angle_001_X_001_Y_001_01of03.xrm.bim.bin	0.725055	0.77319	2.22E-16	2.17485	478063	0.001841
MedianAvg_000001_9L_Long_C_angle_001_X_001_Y_001_01of03.xrm.bim.bin	0.833596	0.874506	2.22E-16	2.66419	865854	0.003273
MedianAvg_000001_9L_Long_NA_angle_001_X_001_Y_001_01of03.xrm.bim.bin	0.807205	0.842813	0.847298	2.117593	158181	0.000587
MedianAvg_000001_9L_Long_T_angle_001_X_001_Y_001_01of03.xrm.bim.bin	0.787875	0.856499	2.22E-16	2.199754	604624	0.002379

m.bin						
MedianAvg_000001_9L_Trans_C_angle_001_X_001_Y_001_01of03.xrm.bim.bim.bin	0.92942	1.024957	2.22E-16	2.682501	1087431	0.004188
MedianAvg_000001_9L_Trans_C_Corner_CrossHatch_angle_001_X_001_Y_001_01of03.xrm.bim.bim.bin	0.992286	1.068792	2.22E-16	3.549534	2608906	0.01014
MedianAvg_000001_9L_Trans_NA_angle_001_X_001_Y_001_01of03.xrm.bim.bim.bin	1.031563	1.049307	1.041454	1.791759	8554	3.16E-05
MedianAvg_000001_9L_Trans_T_angle_001_X_001_Y_001_01of03.xrm.bim.bim.bin	0.990713	1.062073	2.22E-16	2.502198	1124389	0.004289
MedianAvg_000001_9L_Trans_T_Possible_Crack_angle_001_X_001_Y_001_01of03.xrm.bim.bim.bin	0.924851	1.037429	2.22E-16	2.739681	419768	0.001684
MedianAvg_000001_11L_Long_C_angle_001_X_001_Y_001_01of03.xrm.bim.bim.bin	0.803789	0.842183	2.22E-16	2.391816	1132178	0.004262
MedianAvg_000001_11L_Long_NA_angle_001_X_001_Y_001_01of03.xrm.bim.bim.bin	0.82531	0.835687	0.847298	2.046771	484308	0.001801
MedianAvg_000001_11L_Long_T_angle_001_X_001_Y_001_01of03.xrm.bim.bim.bin	0.754182	0.830434	2.22E-16	2.752599	992553	0.003899
MedianAvg_000001_11L_Trans_C_angle_001_X_001_Y_001_01of03.xrm.bim.bim.bin	0.839668	0.905646	2.22E-16	3.008657	1081947	0.004164
MedianAvg_000001_11L_Trans_NA_angle_001_X_001_Y_001_01of03.xrm.bim.bim.bin	0.929172	0.940374	0.980829	2.75693	447506	0.001661
MedianAvg_000001_11L_Trans_T_angle_001_X_001_Y_001_01of03.xrm.bim.bim.bin	0.842279	0.902455	2.22E-16	2.423435	288795	0.001104
MedianAvg_000001_12L_Long_C_angle_001_X_001_Y_001_01of03.xrm.bim.bim.bin	1.02011	1.028167	2.22E-16	2.862412	5058382	0.019102
MedianAvg_000001_12L_Long_NA_angle_001_X_001_Y_001_01of03.xrm.bim.bim.bin	0.997557	1.01519	0.980829	2.403672	392184	0.001453

MedianAvg_000001_12L_Long_T_angle_001_X_001_Y_001_01of03.xrm.bim.bin	0.983607	1.037652	2.22E-16	2.779078	5139478	0.01998
MedianAvg_000001_13L_Long_C_angle_001_X_001_Y_001_01of03.xrm.bim.bin	0.83302	0.843531	0.847298	2.874249	4330367	0.016172
MedianAvg_000001_13L_Long_NA_angle_001_X_001_Y_001_01of03.xrm.bim.bin	0.826854	0.837041	0.847298	1.750281	524928	0.001938
MedianAvg_000001_13L_Long_T_angle_001_X_001_Y_001_01of03.xrm.bim.bin	0.814202	0.881775	2.22E-16	2.372319	1664457	0.006425
MedianAvg_000001_13L_Trans_C_angle_001_X_001_Y_001_01of03.xrm.bim.bin	0.947266	1.013699	2.22E-16	2.879794	902630	0.003487
MedianAvg_000001_13L_Trans_NA_angle_001_X_001_Y_001_01of03.xrm.bim.bin	0.835794	0.841598	0.847298	2.864667	877700	0.003245
MedianAvg_000001_13L_Trans_T_angle_001_X_001_Y_001_01of03.xrm.bim.bin	0.710609	0.755199	2.22E-16	3.095362	884952	0.0034
MedianAvg_000001_15L_Long_C_angle_001_X_001_Y_001_01of03.xrm.bim.bin	0.83285	0.978503	2.22E-16	2.606622	955806	0.003757
MedianAvg_000001_15L_Long_NA_angle_001_X_001_Y_001_01of03.xrm.bim.bin	0.913177	0.931123	0.916291	2.066538	72683	0.000269
MedianAvg_000001_15L_Long_T_angle_001_X_001_Y_001_01of03.xrm.bim.bin	0.884977	0.929536	2.22E-16	2.696241	814957	0.003111
MedianAvg_000001_15L_trans_C_angle_001_X_001_Y_001_01of03.xrm.bim.bin	0.99105	1.033185	1.041454	3.085518	506378	0.001884
MedianAvg_000001_15L_trans_NA_angle_001_X_001_Y_001_01of03.xrm.bim.bin	1.017179	1.03334	1.041454	2.302909	63782	0.000236
MedianAvg_000001_15L_trans_T_angle_001_X_001_Y_001_01of03.xrm.bim.bin	0.981399	1.024771	2.22E-16	3.135494	171721	0.000647
MedianAvg_000001_16L_Long_Compressive_angle	0.699471	0.764205	2.22E-16	2.859396	2630246	0.00994

_001_X_001_Y_001_01of03.xrm.bim.bim.bin						
MedianAvg_000001_16L_Long_NA_angle_001_X_001_Y_001_01of03.xrm.bim.bim.bin	0.760863	0.770494	0.77319	2.503034	637976	0.00236
MedianAvg_000001_16L_Long_Tensile_angle_001_X_001_Y_001_01of03.xrm.bim.bim.bin	0.71791	0.803782	2.22E-16	2.476938	1866085	0.007277
MedianAvg_000001_16L_Trans_C_angle_001_X_001_Y_001_01of03.xrm.bim.bim.bin	0.971393	1.029314	2.22E-16	3.477203	4030990	0.016092
MedianAvg_000001_16L_Trans_NA_angle_001_X_001_Y_001_01of03.xrm.bim.bim.bin	1.029299	1.03113	0.980829	3.39888	3000700	0.011143
MedianAvg_000001_16L_Trans_T_angle_001_X_001_Y_001_01of03.xrm.bim.bim.bin	0.999376	1.032749	2.22E-16	3.322012	596496	0.002245
MedianAvg_000001_18L_Trans_C_angle_001_X_001_Y_001_01of03.xrm.bim.bim.bin	0.827423	0.869144	2.22E-16	2.956428	3957572	0.015263
MedianAvg_000001_18L_Trans_NA_angle_001_X_001_Y_001_01of03.xrm.bim.bim.bin	0.885185	0.916291	0.916291	2.23925	40185	0.000149
MedianAvg_000001_18L_Trans_T_angle_001_X_001_Y_001_01of03.xrm.bim.bim.bin	0.824848	0.884685	2.22E-16	2.460402	746526	0.002861
MedianAvg_000001_19L_Trans_C_angle_001_X_001_Y_001_01of03.xrm.bim.bim.bin	0.87345	0.928878	2.22E-16	2.494123	525630	0.002029
MedianAvg_000001_19L_Trans_NA_angle_001_X_001_Y_001_01of03.xrm.bim.bim.bin	0.843197	0.862089	0.847298	1.16081	282	1.05E-06
MedianAvg_000001_19L_Trans_T_angle_001_X_001_Y_001_01of03.xrm.bim.bim.bin	0.759805	0.818633	2.22E-16	2.700615	1072659	0.004151
MedianAvg_000001_20120217_JM2_long_C_angle_001_X_001_Y_001_01of03.xrm.bim.bim.bin	0.679877	0.724005	2.22E-16	2.038812	327978	0.001233
MedianAvg_000001_20120217_JM2_long_NA_angle_001_X_001_Y_001_01of03.xrm.bim.bim.bin	0.695485	0.721721	0.693147	1.541902	584592	0.002173

MedianAvg_000001_2012 0217_JM2_long_T_angle_001_X_001_Y_001_01of03.xrm.bim.bim.bin	0.751089	0.797053	2.22E-16	1.72214	291887	0.001124
MedianAvg_000001_2012 0218_JM6_lomg_C_angle_001_X_001_Y_001_01of03.xrm.bim.bim.bin	0.930142	0.965955	2.22E-16	2.740372	2095661	0.007913
MedianAvg_000001_2012 0218_JM6_lomg_NA_angle_001_X_001_Y_001_01of03.xrm.bim.bim.bin	0.960902	0.982704	0.980829	1.905088	10753	3.98E-05
MedianAvg_000001_2012 0218_JM6_lomg_T_angle_001_X_001_Y_001_01of03.xrm.bim.bim.bin	0.971849	0.981668	0.980829	2.990647	3048976	0.011444
MedianAvg_000001_2012 0218_JM7_long_L_angle_001_X_001_Y_001_01of03.xrm.bim.bim.bin	0.064465	0.002345	2.22E-16	2.504428	18520248	0.18463
MedianAvg_000001_2012 0218_JM7_long_R_angle_001_X_001_Y_001_01of03.xrm.bim.bim.bin	0.689162	0.735111	2.22E-16	2.482921	996828	0.003825
MedianAvg_000001_2012 0218_JM9_long_C_angle_001_X_001_Y_001_01of03.xrm.bim.bim.bin	0.741336	0.766807	2.22E-16	2.000119	685589	0.002583
MedianAvg_000001_2012 0218_JM9_long_C2_angle_001_X_001_Y_001_01of03.xrm.bim.bim.bin	0.491312	0.715816	2.22E-16	2.426974	1.71E+08	0.84515
MedianAvg_000001_2012 0218_JM9_long_NA_angle_001_X_001_Y_001_01of03.xrm.bim.bim.bin	0.674646	0.684708	0.693147	2.573579	594483	0.002204
MedianAvg_000001_2012 0218_JM9_long_T1_angle_001_X_001_Y_001_01of03.xrm.bim.bim.bin	0.576574	0.594471	0.606136	1.382834	425621	0.001595
MedianAvg_000001_2012 0218_JM9_long_T2_angle_001_X_001_Y_001_01of03.xrm.bim.bim.bin	0.605405	0.645138	2.22E-16	1.571698	767523	0.002925
MedianAvg_000001_2012 0219_C7R_long_C1_angle_001_X_001_Y_001_01of03.xrm.bim.bim.bin	0.824381	0.892249	2.22E-16	1.885514	174712	0.000677
MedianAvg_000001_C1L_Trans_C_angle_001_X_001_Y_001_01of03.xrm.bim.bim.bin	1.132248	1.221505	2.22E-16	3.204722	546289	0.002092
MedianAvg_000001_C1L_Trans_NA_angle_001_X_001_Y_001_01of03.xrm.bim.bim.bin	1.216385	1.222549	1.203973	2.947683	1222879	0.004532

01_Y_001_01of03.xrm.bim.bim.bin						
MedianAvg_000001_C1L_Trans_T_angle_001_X_001_Y_001_01of03.xrm.bim.bim.bin	1.123749	1.191288	2.22E-16	3.087593	500907	0.001907
MedianAvg_000001_C2L_Long_C_angle_001_X_001_Y_001_01of03.xrm.bim.bim.bin	0.61063	0.651762	2.22E-16	2.09021	927981	0.003538
MedianAvg_000001_C2L_Long_NA_angle_001_X_001_Y_001_01of03.xrm.bim.bim.bin	0.661442	0.672697	0.693147	1.249916	90619	0.000336
MedianAvg_000001_C2L_Long_T_angle_001_X_001_Y_001_01of03.xrm.bim.bim.bin	0.642289	0.700473	2.22E-16	1.552971	931829	0.003606
MedianAvg_000001_C4R_long_C_angle_001_X_001_Y_001_01of03.xrm.bim.bim.bin	0.724068	0.76539	2.22E-16	2.833213	310598	0.001176
MedianAvg_000001_C4R_long_NA_angle_001_X_001_Y_001_01of03.xrm.bim.bim.bin	0.800262	0.803851	0.847298	2.369524	3215507	0.01191
MedianAvg_000001_C4R_long_T_angle_001_X_001_Y_001_01of03.xrm.bim.bim.bin	0.817297	0.868582	2.22E-16	2.528607	1755759	0.006833
MedianAvg_000001_C4r_trans_C_angle_001_X_001_Y_001_01of03.xrm.bim.bim.bin	1.083023	1.15105	2.22E-16	3.406738	1091678	0.004154
MedianAvg_000001_C4r_trans_T_angle_001_X_001_Y_001_01of03.xrm.bim.bim.bin	1.155736	1.196349	2.22E-16	4.154137	3862597	0.014736
MedianAvg_000001_C10_Trans_Again_C_angle_001_X_001_Y_001_01of03.xrm.bim.bim.bin	0.970939	1.023441	2.22E-16	3.146544	2317880	0.008909
MedianAvg_000001_C10_Trans_Again_NA_angle_001_X_001_Y_001_01of03.xrm.bim.bim.bin	0.831508	0.837291	0.847298	3.771483	1919348	0.007114
MedianAvg_000001_C10_Trans_Again_T_angle_001_X_001_Y_001_01of03.xrm.bim.bim.bin	0.633733	0.674954	2.22E-16	2.184694	1480471	0.00568
MedianAvg_000001_C10R_long_C_angle_001_X_001_Y_001_01of03.xrm.bim.bim.bin	0.944376	0.993881	2.22E-16	2.056563	406545	0.001527

MedianAvg_000001_C10R _long_NA_angle_001_X_0 01_Y_001_01of03.xrm.bim .bim.bin	0.981016	1.001103	0.980829	1.437791	1756	6.51E-06
MedianAvg_000001_C10R _long_T_angle_001_X_00 1_Y_001_01of03.xrm.bim. bim.bin	0.974958	1.020097	2.22E-16	2.635878	4040305	0.015382
MedianAvg_000001_JM1_ Long_C_angle_001_X_00 1_Y_001_01of03.xrm.bim. bim.bin	0.813138	0.826337	0.847298	1.726785	998680	0.003703
MedianAvg_000001_JM1_ Long_NA_angle_001_X_0 01_Y_001_01of03.xrm.bim .bim.bin	0.655353	0.668342	0.693147	1.209795	11359	4.21E-05
MedianAvg_000001_JM1_ Long_T_angle_001_X_001 _Y_001_01of03.xrm.bim.bi m.bin	0.52487	0.55544	2.22E-16	1.599822	651947	0.002454
MedianAvg_000001_JM1_ trans_C_angle_001_X_00 1_Y_001_01of03.xrm.bim. bim.bin	0.972606	1.022281	2.22E-16	3.041195	616012	0.002321
MedianAvg_000001_JM1_ trans_NA_angle_001_X_0 01_Y_001_01of03.xrm.bim .bim.bin	1.076916	1.088591	1.098612	3.743323	1487641	0.005533
MedianAvg_000001_JM1_ trans_T_angle_001_X_001 _Y_001_01of03.xrm.bim.bi m.bin	1.051818	1.118089	2.22E-16	3.432265	471484	0.001806
MedianAvg_000001_JM2_ Trans_C_angle_001_X_00 1_Y_001_01of03.xrm.bim. bim.bin	0.995741	1.016498	0.980829	2.03335	219437	0.000816
MedianAvg_000001_JM2_ Trans_NA_angle_001_X_0 01_Y_001_01of03.xrm.bim .bim.bin	0.833899	0.853233	0.847298	3.185135	3400511	0.01259
MedianAvg_000001_JM2_ Trans_T_angle_001_X_00 1_Y_001_01of03.xrm.bim. bim.bin	0.689364	0.705432	0.693147	2.6622	542174	0.002024
MedianAvg_000001_JM3_ trans_C_angle_001_X_00 1_Y_001_01of03.xrm.bim. bim.bin	0.944405	0.904253	2.22E-16	4.420446	1305263 2	0.049244
MedianAvg_000001_JM3_ trans_NA_angle_001_X_0 01_Y_001_01of03.xrm.bim .bim.bin	0.894941	0.90937	0.916291	2.03042	227459	0.000842
MedianAvg_000001_JM3_ trans_T_angle_001_X_001	0.798515	0.847298	2.22E-16	2.887723	1552997	0.005966

_Y_001_01of03.xrm.bim.bin						
MedianAvg_000001_Jm4_long_C_angle_001_X_001_Y_001_01of03.xrm.bim.bin	0.805883	0.827427	0.847298	2.943342	867849	0.00323
MedianAvg_000001_Jm4_long_NA_angle_001_X_001_Y_001_01of03.xrm.bim.bin	0.864622	0.888588	0.847298	2.890016	641473	0.002374
MedianAvg_000001_Jm4_long_T_angle_001_X_001_Y_001_01of03.xrm.bim.bin	0.868996	0.908894	2.22E-16	2.936892	654999	0.00249
MedianAvg_000001_Jm4_trans_C_angle_001_X_001_Y_001_01of03.xrm.bim.bin	0.596367	0.670384	2.22E-16	2.45427	477342	0.001643
MedianAvg_000001_Jm4_trans_NA_angle_001_X_001_Y_001_01of03.xrm.bim.bin	0.683676	0.689352	0.693147	2.761009	841525	0.003118
MedianAvg_000001_Jm4_trans_T_angle_001_X_001_Y_001_01of03.xrm.bim.bin	0.495092	0.655529	2.22E-16	2.472113	285492	0.001027
MedianAvg_000001_Jm5_Long_C_angle_001_X_001_Y_001_01of03.xrm.bim.bin	0.729047	0.720697	0.693147	3.359989	4415173	0.016529
MedianAvg_000001_Jm5_Long_NA_angle_001_X_001_Y_001_01of03.xrm.bim.bin	0.695574	0.700489	0.693147	1.929806	578114	0.00215
MedianAvg_000001_Jm5_Long_T_angle_001_X_001_Y_001_01of03.xrm.bim.bin	0.654463	0.714385	2.22E-16	1.831555	1196111	0.004672
MedianAvg_000001_Jm5_Trans_C_angle_001_X_001_Y_001_01of03.xrm.bim.bin	1.074655	1.09377	2.22E-16	3.326608	3569662	0.013377
MedianAvg_000001_Jm5_Trans_NA_angle_001_X_001_Y_001_01of03.xrm.bim.bin	1.09588	1.094118	1.098612	2.952988	3494487	0.012942
MedianAvg_000001_Jm5_Trans_T_angle_001_X_001_Y_001_01of03.xrm.bim.bin	1.148151	1.149638	1.098612	3.060896	2659252	0.009944
MedianAvg_000001_Jm6_Trans_C_angle_001_X_001_Y_001_01of03.xrm.bim.bin	1.00127	1.039408	2.22E-16	4.237001	2028127	0.007632

MedianAvg_000001_Jm6_ Trans_NA_angle_001_X_0 01_Y_001_01of03.xrm.bim .bim.bin	0.994608	1.016849	0.980829	1.353422	22	8.18E-08
MedianAvg_000001_Jm6_ Trans_T_angle_001_X_00 1_Y_001_01of03.xrm.bim. bim.bin	0.98434	1.027516	2.22E-16	2.564949	964797	0.003638
MedianAvg_000001_JM7_ Trans_C_angle_000_X_00 1_Y_001_01of03.xrm.bim. bim.bin	0.750722	0.778608	2.22E-16	2.434263	953859	0.003597
MedianAvg_000001_JM7_ Trans_NA_angle_001_X_0 01_Y_001_01of03.xrm.bim .bim.bin	0.785155	0.792777	0.77319	2.792504	1550447	0.005778
MedianAvg_000001_JM7_ Trans_T_angle_001_X_00 1_Y_001_01of03.xrm.bim. bim.bin	0.691566	0.718465	2.22E-16	2.03862	452144	0.0017
MedianAvg_000001_JM8_ Long_C_angle_001_X_00 1_Y_001_01of03.xrm.bim. bim.bin	0.920347	0.955511	1.11E-16	2.981529	862974	0.003245
MedianAvg_000001_JM8_ Long_NA_angle_001_X_0 01_Y_001_01of03.xrm.bim .bim.bin	0.917444	0.928219	0.916291	2.502198	1218472	0.004523
MedianAvg_000001_JM8_ Long_T_angle_001_X_001 _Y_001_01of03.xrm.bim.bi m.bin	0.777247	0.845075	2.22E-16	1.932259	231615	0.000906
MedianAvg_000001_JM8_ Trans_C_angle_000_X_00 1_Y_001_01of03.xrm.bim. bim.bin	0.91559	0.995935	2.22E-16	2.112407	370054	0.001432
MedianAvg_000001_JM8_ Trans_NA_angle_001_X_0 01_Y_001_01of03.xrm.bim .bim.bin	0.996069	1.016507	0.980829	2.239304	179534	0.000667
MedianAvg_000001_JM8_ Trans_T_angle_001_X_00 1_Y_001_01of03.xrm.bim. bim.bin	0.978827	1.015755	2.22E-16	3.451935	398372	0.001514
MedianAvg_000001_JM9_ Trans_C_angle_001_X_00 1_Y_001_01of03.xrm.bim. bim.bin	0.682265	0.730774	2.22E-16	1.806255	57216	0.000216
MedianAvg_000001_JM9_ Trans_NA_angle_001_X_0 01_Y_001_01of03.xrm.bim .bim.bin	0.716059	0.731582	0.693147	2.531289	1556713	0.005772
MedianAvg_000001_JM9_ Trans_T_angle_001_X_00	0.600459	0.658421	2.22E-16	2.211141	505670	0.001983

1_Y_001_01of03.xrm.bim.bim.bin						
MedianAvg_000001_JM10_Long_C_angle_001_X_001_Y_001_01of03.xrm.bim.bim.bin	0.82088	0.823404	2.22E-16	2.350685	5298049	0.019951
MedianAvg_000001_JM10_Long_NA_angle_001_X_001_Y_001_01of03.xrm.bim.bim.bin	0.761637	0.77319	0.77319	1.042485	120	4.46E-07
MedianAvg_000001_JM10_Long_T_angle_001_X_001_Y_001_01of03.xrm.bim.bim.bin	0.722311	0.783456	2.22E-16	1.363901	1238	4.79E-06
MedianAvg_000001_JM10_Trans_C_angle_000_X_001_Y_001_01of03.xrm.bim.bim.bin	0.669869	0.709314	2.22E-16	2.403672	2199797	0.008432
MedianAvg_000001_JM10_Trans_NA_angle_000_X_001_Y_001_01of03.xrm.bim.bim.bin	0.917766	0.905681	1.11E-16	4.486762	3624432	0.013513
MedianAvg_000001_JM10_Trans_T_angle_000_X_001_Y_001_01of03.xrm.bim.bim.bin	1.06402	1.14819	2.22E-16	2.823361	307314	0.001203
MedianAvg_000001_JM12_Long_C_angle_001_X_001_Y_001_01of03.xrm.bim.bim.bin	0.599875	0.661711	2.22E-16	1.956139	1470225	0.005694
MedianAvg_000001_JM12_Long_NA_angle_001_X_001_Y_001_01of03.xrm.bim.bim.bin	0.675729	0.688254	0.693147	1.272808	55812	0.000208
MedianAvg_000001_JM12_Long_T_angle_001_X_001_Y_001_01of03.xrm.bim.bim.bin	0.690877	0.731613	2.22E-16	2.646419	170351	0.00065
MedianAvg_000001_JM12_Trans_C_angle_001_X_001_Y_001_01of03.xrm.bim.bim.bin	1.00564	1.032122	2.22E-16	2.974428	2330564	0.008754
MedianAvg_000001_JM12_Trans_NA_angle_001_X_001_Y_001_01of03.xrm.bim.bim.bin	0.852009	0.861356	0.847298	2.020715	84538	0.000314
MedianAvg_000001_JM12_Trans_T_angle_001_X_001_Y_001_01of03.xrm.bim.bim.bin	0.644925	0.755497	2.22E-16	1.921419	415207	0.001726
MedianAvg_000001_JM13_Trans_NA_angle_001_X_001_Y_001_01of03.xrm.bim.bim.bin	0.849261	0.847298	0.847298	3.619481	3453849	0.012817

MedianAvg_000001_JM13 _Trans_T_angle_001_X_0 01_Y_001_01of03.xrm.bim .bim.bin	0.901302	0.878646	2.22E-16	4.056503	8396278	0.031909
000001_1UA_1_angle_- 05_X_001_Y_001_01of01. xrm.bim.bin	0.29137	0.324316	2.22E-16	0.81796	307843	0.001776
000001_1UA_2_angle_- 05_X_001_Y_001_01of01. xrm.bim.bin	0.366532	0.370244	0.405465	1.046787	428372	0.002415
000001_1UA_3_angle_- 05_X_001_Y_001_01of01. xrm.bim.bin	0.436127	0.443064	0.405465	0.956565	32137	0.000182
000001_1UA_4_angle_- 05_X_001_Y_001_01of01. xrm.bim.bin	0.280623	0.320599	2.22E-16	0.724157	825092	0.004724
000001_1UA_5_angle_- 05_X_001_Y_001_01of01. xrm.bim.bin	0.293738	0.342184	2.22E-16	0.770579	1039529	0.006133
000001_1UA_6_angle_- 05_X_001_Y_001_01of01. xrm.bim.bin	0.29999	0.378654	2.22E-16	0.802073	379461	0.002347
000001_1UA_7_angle_- 05_X_001_Y_001_01of01. xrm.bim.bin	0.373768	0.377762	0.405465	0.625472	2944	8.78E-06
000001_2UA_2_angle_- 05_X_001_Y_001_01of01. xrm.bim.bin	1.388371	1.414163	1.386294	1.852148	1179	6.58E-06
000001_2UA_3_angle_- 05_X_001_Y_001_01of01. xrm.bim.bin	1.278942	1.287578	1.386294	1.721801	8544	4.75E-05
000001_2UA_4_angle_- 05_X_001_Y_001_01of01. xrm.bim.bin	1.152223	1.432456	2.22E-16	2.548718	57499	0.000325
000001_2UA_5_angle_- 05_X_001_Y_001_01of01. xrm.bim.bin	1.174889	1.352271	1.386294	2.362739	126432	0.00071
000001_2UA_7_angle_- 05_X_001_Y_001_01of01. xrm.bim.bin	1.384416	1.379515	1.386294	4.284571	5001678	0.01486
000001_3UA_1_angle_- 05_X_001_Y_001_01of01. xrm.bim.bin	1.147052	1.154557	1.098612	1.848163	25344	0.00041
000001_3UA_2_angle_00 0_X_001_Y_001_01of01.x rm.bim.bin	1.081998	1.139916	1.098612	1.582921	1423	1.47E-05
000001_3UA_3_angle_00 0_X_001_Y_001_01of01.x rm.bim.bin	0.978404	1.118344	2.22E-16	1.621608	641	4.95E-06
000001_3UA_4_angle_00 0_X_001_Y_001_01of01.x rm.bim.bin	1.014047	1.021381	0.547592	1.864449	83711	0.000633
000001_3UA_5_angle_00 0_X_001_Y_001_01of01.x	1.04525	1.053762	1.098612	1.566298	22758	0.000173

rm.bim.bin						
000001_3UA_6_angle_00 0_X_001_Y_001_01of01.x rm.bim.bin	1.057821	1.066443	1.098612	1.965031	85692	0.000652
000001_5UA_1_angle_- 03_X_001_Y_001_01of01. xrm.bim.bin	0.591116	0.595065	0.587787	0.926654	15960	9.06E-05
000001_5UA_2_angle_- 03_X_001_Y_001_01of01. xrm.bim.bin	0.600674	0.605372	0.587787	0.942402	4653	2.64E-05
000001_5UA_3_angle_- 03_X_001_Y_001_01of01. xrm.bim.bin	0.581968	0.592677	0.559616	0.973789	20508	0.000115
000001_5UA_4_angle_- 03_X_001_Y_001_01of01. xrm.bim.bin	0.546681	0.601128	2.22E-16	1.098612	126570	0.000721
000001_5UA_5_angle_- 03_X_001_Y_001_01of01. xrm.bim.bin	0.574631	0.602996	2.22E-16	1.272966	195180	0.001108
000001_5UA_6_angle_- 03_X_001_Y_001_01of01. xrm.bim.bin	0.622721	0.62253	0.693147	1.526459	1964964	0.010998
000001_5UA_7_angle_- 03_X_001_Y_001_01of01. xrm.bim.bin	0.42712	0.553927	2.22E-16	1.830474	111542	0.000251
000001_5UA_8_angle_- 03_X_001_Y_001_01of01. xrm.bim.bin	0.599377	0.616555	2.22E-16	1.450182	374427	0.002111
000001_6UA_1_angle_- 06_X_001_Y_001_01of01. xrm.bim.bin	0.630824	0.764679	2.22E-16	1.447538	193760	0.001119
000001_6UA_2_angle_- 06_X_001_Y_001_01of01. xrm.bim.bin	0.717538	0.818443	2.22E-16	1.649789	365359	0.002126
000001_6UA_3_angle_- 06_X_001_Y_001_01of01. xrm.bim.bin	0.666118	0.839101	2.22E-16	1.797625	127554	0.000762
000001_6UA_4_angle_- 06_X_001_Y_001_01of01. xrm.bim.bin	0.76129	0.879874	2.22E-16	2.734368	352854	0.002023
000001_6UA_5_angle_- 06_X_001_Y_001_01of01. xrm.bim.bin	0.895909	0.897243	0.916291	2.211018	1240776	0.006952
000001_6UA_6_angle_- 06_X_001_Y_001_01of01. xrm.bim.bin	0.871696	0.875058	0.916291	1.895333	1388541	0.007766
000001_6UA_7_angle_- 06_X_001_Y_001_01of01. xrm.bim.bin	0.833001	0.826938	0.847298	3.141686	1758187	0.005264
000001_8AU_1_angle_- 02_X_001_Y_001_01of01. xrm.bim.bin	0.362326	0.369555	0.405465	0.955881	128866	0.002074
000001_8UA_2_angle_00	0.334939	0.373042	2.22E-16	1.006999	291569	0.00204

0_X_001_Y_001_01of01.x rm.bim.bin						
000001_8UA_3_angle_00 0_X_001_Y_001_01of01.x rm.bim.bin	0.378125	0.393417	2.22E-16	1.506297	969137	0.005461
000001_8UA_4_angle_00 0_X_001_Y_001_01of01.x rm.bim.bin	0.386306	0.400243	2.22E-16	1.166716	353791	0.00199
000001_8UA_6_angle_00 0_X_001_Y_001_01of01.x rm.bim.bin	0.636048	0.871113	2.22E-16	1.958814	66517	0.000297
000001_8UA_8_angle_00 0_X_001_Y_001_01of01.x rm.bim.bin	0.517647	0.767531	2.22E-16	2.319424	1.49E+08	0.682349
000001_9UA_1_angle_- 06_X_001_Y_001_01of01. xrm.bim.bin	0.811132	0.815114	0.847298	1.473482	149591	0.001006
000001_9UA_2_angle_00 0_X_001_Y_001_01of01.x rm.bim.bin	0.800992	0.816918	0.847298	1.228349	2714	1.35E-05
000001_9UA_3_angle_00 0_X_001_Y_001_01of01.x rm.bim.bin	0.774449	0.790042	0.693147	1.241866	4471	2.21E-05
000001_9UA_4_angle_00 0_X_001_Y_001_01of01.x rm.bim.bin	0.686543	0.693147	0.693147	1.530746	464935	0.00171
000001_9UA_5_angle_00 0_X_001_Y_001_01of01.x rm.bim.bin	0.523463	0.638087	2.22E-16	0.999063	470	1.91E-06
000001_9UA_6_angle_00 0_X_001_Y_001_01of01.x rm.bim.bin	0.395393	0.578888	2.22E-16	0.987387	15	6.97E-08
000001_13UA_1_angle_- 07_X_001_Y_001_01of01. xrm.bim.bin	0.533037	0.740188	2.22E-16	1.482832	40273	0.000366
000001_13UA_2_angle_- 07_X_001_Y_001_01of01. xrm.bim.bin	0.626721	0.778507	2.22E-16	2.539632	646391	0.004132
000001_13UA_3_angle_- 07_X_001_Y_001_01of01. xrm.bim.bin	0.740638	0.817445	2.22E-16	2.296799	1622614	0.009267
000001_13UA_4_angle_- 07_X_001_Y_001_01of01. xrm.bim.bin	0.73459	0.88768	2.22E-16	1.871802	89149	0.000524
000001_13UA_5_angle_- 07_X_001_Y_001_01of01. xrm.bim.bin	0.784649	0.905241	2.22E-16	1.981986	503414	0.002929
000001_13UA_6_angle_- 07_X_001_Y_001_01of01. xrm.bim.bin	0.856357	0.874364	0.916291	1.95791	138183	0.000776
000001_13UA_7_angle_- 07_X_001_Y_001_01of01. xrm.bim.bin	0.751368	0.758582	0.693147	1.063927	260	7.8E-07

000001_16UA_1_angle_-06_X_001_Y_001_01of01.xrm.bim.bin	0.654565	0.803418	2.22E-16	1.18856	5960	3.47E-05
000001_16UA_2_angle_-06_X_001_Y_001_01of01.xrm.bim.bin	0.863326	0.878458	0.916291	1.326544	21497	0.000121
000001_16UA_3_angle_-06_X_001_Y_001_01of01.xrm.bim.bin	0.797731	0.832613	0.847298	1.371224	34964	0.000196
000001_16UA_4_angle_-06_X_001_Y_001_01of01.xrm.bim.bin	0.880861	0.917305	0.916291	1.782135	67515	0.000379
000001_16UA_5_angle_-06_X_001_Y_001_01of01.xrm.bim.bin	0.877516	0.88369	0.24818	2.43531	53382	0.0003
000001_16UA_6_angle_-06_X_001_Y_001_01of01.xrm.bim.bin	0.843242	0.846481	0.847298	1.113254	137704	0.000778
000001_16UA_7_angle_-06_X_001_Y_001_01of01.xrm.bim.bin	0.8004	0.807372	0.81093	1.746909	127400	0.00038
000001_18UA_1_angle_-05_X_001_Y_001_01of01.xrm.bim.bin	0.75631	0.861863	2.22E-16	1.865371	693186	0.003946
000001_18UA_2_angle_-05_X_001_Y_001_01of01.xrm.bim.bin	0.853897	0.881379	0.916291	1.379194	5310	2.98E-05
000001_18UA_3_angle_-05_X_001_Y_001_01of01.xrm.bim.bin	0.850905	0.866166	0.916291	1.836032	31339	0.000175
000001_18UA_4_angle_-05_X_001_Y_001_01of01.xrm.bim.bin	0.709024	0.810408	2.22E-16	1.288786	11247	6.41E-05
000001_18UA_5_angle_-05_X_001_Y_001_01of01.xrm.bim.bin	0.850192	0.855882	0.847298	1.250749	31331	0.000178
000001_18UA_6_angle_-05_X_001_Y_001_01of01.xrm.bim.bin	0.838599	0.843087	0.847298	2.032189	996328	0.005565
000001_18UA_7_angle_-05_X_001_Y_001_01of01.xrm.bim.bin	0.764279	0.775839	0.693147	1.07914	18133	0.000101
000001_20UA_1_angle_-10_X_001_Y_001_01of01.xrm.bim.bin	0.541905	0.730361	2.22E-16	1.724238	48468	0.000208
000001_20UA_1_angle_-10_X_001_Y_001_01of01.xrm.bin	0.549182	0.747607	0	1.715291	99172	0.00042
000001_20UA_2_angle_000_X_001_Y_001_01of01.xrm.bim.bin	0.732375	0.81093	2.22E-16	2.128232	1628273	0.006067
000001_20UA_3_angle_000_X_001_Y_001_01of01.xrm.bim.bin	0.730921	0.82063	2.22E-16	2.170506	1520884	0.005864

000001_20UA_4_angle_0 00_X_001_Y_001_01of01. xrm.bim.bin	0.271958	0.297732	2.22E-16	0.844082	377027	0.001446
000001_20UA_5_angle_0 00_X_001_Y_001_01of01. xrm.bim.bin	0.33267	0.338296	0.405465	0.835839	155681	0.000578
000001_22UA_1_angle_- 05_X_001_Y_001_01of01. xrm.bim.bin	0.221929	0.239593	2.22E-16	0.588924	1017477	0.005788
000001_22UA_2_angle_- 05_X_001_Y_001_01of01. xrm.bim.bin	0.258282	0.261216	0.287682	0.68613	19120	0.000108
000001_22UA_3_angle_- 05_X_001_Y_001_01of01. xrm.bim.bin	0.249606	0.252067	2.22E-16	0.836248	49423	0.000279
000001_22UA_4_angle_- 05_X_001_Y_001_01of01. xrm.bim.bin	0.222053	0.266855	2.22E-16	1.709068	143229	0.000859
000001_22UA_5_angle_- 05_X_001_Y_001_01of01. xrm.bim.bin	0.202353	0.246769	2.22E-16	1.202682	192963	0.001188
000001_22UA_6_angle_- 05_X_001_Y_001_01of01. xrm.bim.bin	0.185457	0.238995	2.22E-16	1.012557	310322	0.00196
000001_22UA_7_angle_- 05_X_001_Y_001_01of01. xrm.bim.bin	0.237124	0.23923	0.223144	0.484991	208150	0.000627
000001_23UA_1_angle_- 06_X_001_Y_001_01of01. xrm.bim.bin	0.667851	0.769023	2.22E-16	1.271631	52794	0.000299
000001_23UA_2_angle_- 06_X_001_Y_001_01of01. xrm.bim.bin	0.773761	0.808501	2.22E-16	1.314946	10527	5.93E-05
000001_23UA_3_angle_- 06_X_001_Y_001_01of01. xrm.bim.bin	0.785531	0.816292	0.847298	1.134251	374	2.1E-06
000001_23UA_4_angle_- 06_X_001_Y_001_01of01. xrm.bim.bin	0.627965	0.732713	2.22E-16	1.586367	2116129	0.01195
000001_23UA_5_angle_- 06_X_001_Y_001_01of01. xrm.bim.bin	0.68422	0.741394	2.22E-16	1.308517	540837	0.003053
000001_23UA_6_angle_- 06_X_001_Y_001_01of01. xrm.bim.bin	0.74977	0.785028	0.693147	1.489398	313579	0.001766
000001_23UA_7_angle_- 06_X_001_Y_001_01of01. xrm.bim.bin	0.798993	0.813775	0.847298	1.232649	8437	2.52E-05
000074_2UA_1_angle_- 05_X_004_Y_011_01of01. xrm.bim.bin	1.247452	1.479076	2.22E-16	2.063441	893	5.06E-06

MATLAB Code:

Code to determine thickness for 90 degree rotated sample:

```
%Program written to use a set of data from a text file and determine the
%sample thickness for a specimen measured at SLAC
% written by Garry Brock - May, 2010

clear all;
close all;
clc
%Prompt user to get the thickness file, note file must be in the same
%folder as the M file.
file=uigetfile('*.txt','Please select the data you would like to use to determine sample thickness');
%Pull in data and create arrays for the position and intensity data.
A = dlmread(file,'\t',2,0);
Position=A(:,1);
Intensity=A(:,3);
%Plot the raw data of position vs. intensity
plot(Position,Intensity)
title('Intensity of line in image')
xlabel('Position (microns)')
ylabel('Intensity')

%determine all points less than 10 in intensity

Total_Length=max(Position);
Total_readings=size(Position);
Step_Size=Total_Length/Total_readings(1,1);
Count=0;
for j=1:1:Total_readings
    if Intensity(j,1)<10
        Count=Count+1;
    else
        Count=Count+0;
    end
end

Thickness=Count*Step_Size;
disp('The sample is: ')
file
disp('The thickness of the sample in microns is therefore: ')
Thickness
```

Code for determining total UA:

```
%Code to take bin files from TXM data and determine the percentage of
```

```
%Uranyl Acetate Staining of Microdamage present in each of the matrices
```

```
% Written by Garry Brock, March 11, 2011
```

```
tic
```

```
clear all;close all; clc;
```

```
% Import Bin Files for Interpretation
```

```
[filename,pathname]=uigetfile('*.bin','Please Select the .bin files created from TXM
```

```
images','MultiSelect','on');
```

```
% determine file size for loop
```

```
size=size(filename);
```

```
%loop files
```

```
for i=1:1:size(1,2)
```

```
    %get file names
```

```
    rn = sprintf('%s%s', pathname, filename{i});
```

```
    %read bin files
```

```
[metadata image] = readBINfile(rn);
```

```
%progressbar(i/size(1,2))
```

```
Sum=0;
```

```
T=0;
```

```
%if metadata.HBin >1
```

```
% image=image/(metadata.HBin.*metadata.VBin);
```

```
%end
```

```
%switch any below zero values for intensity to zero
```

```
for j=1:1:metadata.height;
```

```
    for k=1:1:metadata.width;
```

```
        if image(j,k)<0
```

```
            image(j,k)=0;
```

```
        end
```

```
    end
```

```
end
```

```
%convert histogram of data to a single column of data
```

```
Hist=image(:);
```

```
%determine mean of data
```

```
mean=mean2(Hist);
```

```
%determine median of data
```

```
median=median(Hist);
```

```
%determine mode of data
```

```
mode=mode(Hist);
```

```
%determine minimum of data
```

```
min=min(Hist);
```

```
%determine max of data
```

```

Max=max(Hist);
%Determine Histogram distribution
[N,X]=hist(Hist,1000);

N=N(1,3:1000);
X=X(1,3:1000);

[Np,ind]=max(N);
Xp=X(1,ind);
Xf=X(1,998);
Nf=N(1,998);

Length=1000-ind+1;

for z=1:1:Length
    a(1,z)=((X(1,z)-Xp)^2+(N(1,z)-Np)^2)^(1/2);
    b(1,z)=((Xf-X(1,z))^2+(Nf-N(1,z))^2)^(1/2);
    c(1,z)=((Xf-Xp)^2+(Nf-Np)^2)^(1/2);

    d(1,z)=((-a(1,z)^4+2*a(1,z)^2*(b(1,z)^2+c(1,z)^2)-b(1,z)^4+2*b(1,z)^2*c(1,z)^2-
c(1,z)^4)/2*c(1,z))^(1/2);
end
    [dmax,indmax]=max(d);
    X_threshold=X(1,indmax);
    X_cutoff=X_threshold+round(0.2*Xf);
    XC=indmax+200;
if X_cutoff<Xf
    for j=XC:1:998
        m=N(1,j);
    end
else
    m=0;
end
Sum=sum(m);

for k=3:1:998
    Total=N(1,k);
end

Bone=sum(Total);

% if min>0
%
% po=find(X>mode,1000);
% X50=X(po(end));
% [v,p]=max(N);
% ymax=v;
% xmax=X(p(end));
%
% for i=p:po(end)

```

```

% A= double(-(mode-ymax)/(X50-xmax));
% B=double(1);
% C=double(-(mode - (mode-ymax)/(X50-xmax)*X50));
%
% m=X(i);
% n=N(i);
%
% d(i)=(A*m + B*n +C)/sqrt(A^2 + B^2);
% end
%
% [v,p]=max(abs(d));
% T=X(p);
% end

%
% if X>T
% UA=find(X);
% Sum=N(UA);
% end
% sum=sum(Sum);

% for j=1:1:998;
% if mode>0
% if X(1,j)>mode
% M=max(N);
% cutoff=0.05*M;
% s=N(find(N<cutoff));
% Sum=sum(s);
% end
% end
% end
% %peakfit([X N],mode,0.3*mode,3,1)
%
% counts=0;
% Damage=0;
% for j=1:1:metadata.height;
% for k=1:1:metadata.width;
% if image(j,k)>=mode
% counts(j,1)=image(j,k);
% Damage=Damage+1;
% end
% end
% end
% UAAVG=mean2(counts);
% UASTD=std2(counts);
%
% undamaged=0;
% for j=1:1:metadata.height;
% for k=1:1:metadata.width;
% if image(j,k)<=mode

```

```

%     undamaged=undamaged+1;
%     end
% end
% end
% UA=Damage-undamaged;
file(i,2)=metadata.width;
file(i,3)=metadata.height;
file(i,4)=metadata.angles;
file(i,5)=metadata.pixelsize;
file(i,6)=metadata.HBin;
file(i,7)=metadata.VBin;
file(i,8)=metadata.energy;
file(i,9)=mean;
file(i,10)=median;
file(i,11)=mode;
file(i,12)=Max;
file(i,13)=min;
% file(i,14)=UAAVG;
% file(i,15)=UASTD;
% file(i,16)=UA;
file(i,14)=Sum;
file(i,15)=Sum/Bone
i
clear Hist image mean median mode Sum Max min T Bone a b c d M N X XC Xf Xp X_cutoff
X_threshold s
end
%disp(file)
F=transpose(filename);
rxls = sprintf('%s%s', pathname, 'data');
xlswrite(rxls,F,'Sheet1')
xlswrite(rxls,file,'Sheet2')
toc

```

Chapter 9

Appendix C: Chapter 5 Data

Below is the calculated values for each of the trabeculae for each of the measures:

Porosity by Depth for each sample:

	Group	Depth from Surface								
		0-5	5 to 10	10 to 15	15 to 20	20 to 25	25 to 30	30 to 35	35 to 40	inner portion
1L_1	MA1	0.845775	0.951469	0.98342	0.989933	0.977861	0.989811	0.999517		
1L_2	MA1	0.899165	0.939389	0.967653	0.991858	0.947792	0	0.995956		
5L	ALN	0.776638	0.853288	0.876072	0.906654	0.934946	0.961412	0.959976	0.952053	0.938937
9L_1	ALN	0.766156	0.859336	0.879531	0.873523	0.907325	0.909792	0.94044	0.953922	0.913042
9L_2	ALN	0.689757	0.895488	0.906791	0.897378	0.927517	0.972337	0.978483	0.975914	0.975165
11L										
12L	RAL	0.65734	0.814613	0.88548	0.913084	0.945737	0.942963	0.956077	0.934996	0.955471
15L	MA1	0.666616	0.81523	0.860134	0.90393	0.96528	0.988501	0.986961	0.988274	0.975116
16L	RAL	0.81208	0.931783	0.939559	0.940872	0.932272	0.940198	0.969317	0.941153	0.979627
18L	RAL	0.690146	0.841927	0.895917	0.914894	0.904686	0.948329	0.975963	0.981531	0.97846
19L	RAL	0.724924	0.848755	0.865931	0.911199	0.9497	0.960752	0.969191	0.984557	0.975569
C04	C	0.778743	0.933321	0.910575	0.940636	0.967882	0.949772	0.953148	0.964137	0.963852
C05	C	0.731956	0.86188	0.90076	0.923049	0.919824	0.941183	0.95649	0.953195	0.889349
JM5	ZOL	0.708837	0.896641	0.920993	0.954892	0.969801	0.98157	0.983186	0.980851	0.970081
Jm6	MA2	0.669678	0.801072	0.882271	0.94186	0.970907	0.954022	0.954112	0.970958	0.977621
JM7	ZOL	0.714928	0.895042	0.902061	0.91357	0.935226	0.949721	0.952582	0.953827	0.943499
JM9	MA2									
JM10	ZOL	0.857589	0.9122	0.963623	0.991783	0.962678	0.984289	0.974036	0.97457	0.934275
JM12	MA2	0.766783	0.85189	0.919898	0.97294	0.974198	0.952388	0.975898	0.989067	0.983961
JM13	MA2	0.744222	0.936734	0.964856	0.967797	0.984006	0.973179	0.977226	0.965865	0.972158

Lacunar-canalicular volumes for each sample:

Sample ID	Group	Lacunar Volume	Canalicular Volume	LAC_Volume
1L_1	MA1	0.015337	0.043861	0.059198
1L_2	MA1	0.019193	0.036582	0.055775
5L	ALN	0.036563	0.060951	0.097515
9L_1	ALN	0.027201	0.098644	0.125844
9L_2	ALN	0.021491	0.064618	0.08611
11L				
12L	RAL	0.033052	0.072992	0.106045
15L	MA1	0.030953	0.095562	0.126515
16L	RAL	0.020125	0.049761	0.069886
18L	RAL	0.018472	0.075868	0.09434
19L	RAL	0.0245	0.058886	0.083386
C04	C	0.022107	0.058493	0.0806
C05	C	0.037942	0.077213	0.115155
JM5	ZOL	0.016883	0.052595	0.069478
Jm6	MA2	0.026897	0.077148	0.104044
JM7	ZOL	0.022326	0.069649	0.091975
JM9	MA2			
JM10	ZOL	0.020765	0.036671	0.057436
JM12	MA2	0.022804	0.063206	0.08601
JM13	MA2	0.015391	0.043935	0.059326

Lacunar-Density and Volume

	Group	Total Lacunae	Total Volume	Lacunae Volume	Lacunar Density (#/mm ³)	Volume of Single Lacunae
1L_1	MA1	25	3.29287E-13	5.05031E-15	75921.70562	202.0122032
1L_2	MA1	6	9.95401E-14	1.91048E-15	60277.23658	318.4125209
5L	ALN	75	1.87619E-12	6.70661E-14	39974.73271	894.2149844
9L_1	ALN	13	2.78284E-13	7.56954E-15	46714.89624	582.2722688
9L_2	ALN	12	3.43619E-13	7.38488E-15	34922.40918	615.4069065
11L						
12L	RAL	24	6.14195E-13	2.03006E-14	39075.54719	845.857616
15L	MA1	16	2.86486E-13	8.86751E-15	55849.2285	554.2196241
16L	RAL	19	3.67848E-13	7.40293E-15	51651.70331	389.6279271
18L	RAL	19	4.76954E-13	8.81028E-15	39836.15306	463.6987192
19L	RAL	18	3.23053E-13	7.9149E-15	55718.33504	439.7164092
C04	C	10	2.56666E-13	5.67407E-15	38961.11377	567.4068011
C05	C	17	3.45477E-13	1.31082E-14	49207.37247	771.0726237
JM5	ZOL	60	2.00278E-12	3.38125E-14	29958.35803	563.5413119
Jm6	MA2	14	4.24009E-13	1.14044E-14	33018.16949	814.5985347
JM7	ZOL	55	1.52253E-12	3.39913E-14	36123.9903	618.024218
JM9	MA2					
JM10	ZOL	7	1.55882E-13	3.2369E-15	44905.80066	462.4144061
JM12	MA2	10	1.37071E-13	3.12583E-15	72954.75763	312.5829674
JM13	MA2	5	2.6919E-13	4.14309E-15	18574.2505	828.6185557
Totals		399	1.00095E-11	2.48863E-13	39862.05434	623.7177088

Below is the Matlab Code used for Calculations

Code for calculating the porosity at 5 micron intervals:

%This program is written for thresholding and calculating the BMD of slices

%of bone taken with TXM at the Stanford Synchrotron Radiation Lightsource.

%Input files should be in the format of a slice file with extension *.bin

```

% Values output are the bone mineral density and the porosity of the bone.

% Code written by Garry Brock, January 2014

% close all open GUIs and clear all data variables
clear all
close all
clc

% set up general variables for attenuation and volume
Attenuation=0;
Volume=0;
% Import files into matlab, select multiple files at once
[Filename_ART, Pathname_ART] = uigetfile('*.binslice','Please select set of ART files for
determination of mineral content ','multiselect','on')
filename_size=size(Filename_ART)
% Read in all of the data and save the image stack in a 3D matrix. Must have
% TXM binary .m files in the same folder for this to work!
for i=1:1:filename_size(1,2)
    rn = sprintf('%s%s', Pathname_ART, Filename_ART{i});
    [image_ART(:, :, i) metadata] = readfile(rn);

[image_width image_height]=size(image_ART);

end
%
% [Filename_FBP, Pathname_FBP] = uigetfile('*.binslice','Please select set of FBP files for
determination of mineral content ','multiselect','on')
% filename_size=size(Filename_FBP)
% % Read in all of the data and save the image stack in a 3D matrix. Must have
% % TXM binary .m files in the same folder for this to work!
% for i=1:1:filename_size(1,2)
%     rn = sprintf('%s%s', Pathname_FBP, Filename_FBP{i});
%     [image_FBP(:, :, i) metadata] = readfile(rn);
%
% [image_width image_height]=size(image_FBP);
%
% end

%%%%%%%%%%%%%% Code to Threshold the ART Image %%%%%%%%%%%%%%%

% resize matrix to more managable size for thresholding (use 10% of data
image_small=imresize(image_ART,0.01);

```

```

Image_Hist=image_small(:);
[Data Counts]=hist(Image_Hist,2000);
h=plot(Counts, Data)
%Plot and save a histogram of all of the data
Slicename=sprintf('%s%s%s',Pathname_ART, 'Hist_of_all_data','.tif');
saveas(h,Slicename,'tif')
[xstart,ystart]=ginput(1);
[xend,yend]=ginput(1);
%Choose points before and after the start of the gaussian region
lin_start = xstart; %input('Start of linear region? ');
lin_end = xend; %input('End of linear region? ');
lin_region_start = min(find(Counts>lin_start));
lin_region_end = min(find(Counts>lin_end));
%lin_region_start = min(find(dis>.4));
%lin_region_end = min(find(dis>.7));
Counts_cut = Counts(lin_region_start:lin_region_end);
Data_cut = Data(lin_region_start:lin_region_end);
%Fit a gaussian peak to the section of data
[f,gof,output] = fit(Counts_cut',Data_cut','gauss1')
figure(2)
%save image including the gaussian peak
h=plot(f,Counts_cut',Data_cut')
Slicename=sprintf('%s%s%s',Pathname_ART, 'Cut_Hist','.tif');
saveas(figure(2),Slicename,'tif')
%the mean is the second output of the gaussian function and the standard
%deviation is half of the third output
mean=f.b1;
sd=(f.c1)/2;

%create low and high thresholds by taking the mean plus or minus 3SD
%(should include 99.7 percent of the data thoeretically
Low_Thresh=mean-3*sd;
High_Thresh=mean+4*sd;

%Use the low and high threshold to remove the gold beads and background.
%Everying not falling within the bone region is changed to be a value of
%zero
[width height]=size(image_ART(:,:,1));
for i=1:1:width
    for j=1:1:height
        for k=1:1:filename_size(1,2)
            if image_ART(i,j,k)<Low_Thresh
                image_ART(i,j,k)=0;
            end
            if image_ART(i,j,k)>High_Thresh

```



```

%
% %Use the low and high threshold to remove the gold beads and background.
% %Everying not falling within the bone region is changed to be a value of
% %zero
% [width height]=size(image_FBP(:,:,1));
% for i=1:1:width
%   for j=1:1:height
%     for k=1:1:filename_size(1,2)
%       if image_FBP(i,j,k)<Low_Thresh
%         image_FBP(i,j,k)=0;
%       end
%       if image_FBP(i,j,k)>High_Thresh
%         image_FBP(i,j,k)=0;
%       end
%     end
%   end
% end
%
% %Save both falsecolor and grayscale images of each slice for both ART and
% %FBP
% figure(1)
% for k=1:1:filename_size(1,2)
%   Slicename=sprintf('%s%s%s%d%s',Pathname_ART, 'falsecolor_',Filename_ART{k},k,'.tif');
%   h=imagesc(image_ART(:,:,k));
%   saveas(h,Slicename,'tif')
% end
% for k=1:1:filename_size(1,2)
%   Slicename=sprintf('%s%s%s%d%s',Pathname_ART, 'grayscale_',Filename_ART{k},k,'.tif');
%   h=imagesc(image_ART(:,:,k)); colormap(gray);
%   saveas(h,Slicename,'tif')
% end
% for k=1:1:filename_size(1,2)
%   Slicename=sprintf('%s%s%s%d%s',Pathname_FBP, 'grayscale_',Filename_FBP{k},k,'.tif');
%   h=imagesc(image_FBP(:,:,k)); colormap(gray);
%   saveas(h,Slicename,'tif')
% end
% for k=1:1:filename_size(1,2)
%   Slicename=sprintf('%s%s%s%d%s',Pathname_FBP, 'grayscale_',Filename_FBP{k},k,'.tif');
%   h=imagesc(image_FBP(:,:,k)); colormap(gray);
%   saveas(h,Slicename,'tif')
% end
% Results=zeros(27,filename_size(1,2));
%

```

```

% %calculate the total attenuation and volume of the bone region. This can be
% %used to determine a measure of TMD
% for i=1:1:width
%   for j=1:1:height
%     for k=1:1:filename_size(1,2)
%       if image_ART(i,j,k)>0
%         Attenuation=Attenuation+image_FBP(i,j,k);
%         Volume=Volume+1;
%       end
%     end
%   end
% end
%
% TMD=Attenuation/Volume
% f
% gof
% Volume
% Area=Volume/k
% Diameter=((Area*(162*10^(-9))^2)/3.14)^(1/2)
for i=1:1:filename_size(1,2)
    i
    %thresholded image is converted to black and white binary image
    BW=im2bw(image_ART(:,:,i),0.0000001);
    figure(3);
    Slicename=sprintf('%s%s%s%d%s',Pathname_ART, 'BW_',Filename_ART{i},i,'.tif');
    h=imagesc(BW); colormap(gray);
    saveas(h,Slicename,'tif')

%Lacunae and canaliculi within the sample are filled in to get a bone
% volume
% se = strel('disk',31);
% conn=conndef(2,'maximal');
% BW2 = imfill(BW,conn,'holes');
% BW2=imdilate(BW2,se);
% BW2=imfill(BW2,conn,'holes');
% BW2=imerode(BW2,se);
BW2=BW;
figure(4);
Slicename=sprintf('%s%s%s%d%s',Pathname_ART, 'BW_filled_',Filename_ART{i},i,'.tif');
h=imagesc(BW2); colormap(gray);
saveas(h,Slicename,'tif')
%complement image is taken to get a thresholded region of background and
%the lacunar - canalicular network
BW_inv=imcomplement(BW);

```

```

figure(5);
Slicename=sprintf('%s%s%s%d%s',Pathname_ART, 'inverse_BW_',Filename_ART{i},i,'.tif');
h=imagesc(BW_inv); colormap(gray);
saveas(h,Slicename,'tif')
%complement image is taken to get solely the background
BW2_inv=imcomplement(BW2);
figure(6);
Slicename=sprintf('%s%s%s%d%s',Pathname_ART,
'inverse_BW_filled_',Filename_ART{i},i,'.tif');
h=imagesc(BW2_inv); colormap(gray);
saveas(h,Slicename,'tif')
%Porous region is calculated by summing the region of bone without the
%lacunar and canalicular network and then adding the background area. The
%inverse is then taken to get a measure of only the lacunar canalicular
%network.
Porosity=imcomplement(BW+BW2_inv);
figure(7);
Slicename=sprintf('%s%s%s%d%s',Pathname_ART, 'LAC_network_',Filename_ART{i},i,'.tif');
h=imagesc(Porosity); colormap(gray);
saveas(h,Slicename,'tif')
%The percent porosity is the sum of the matrix of the lacunar canalicular
%network divided by the total trabecular volume.
Percent_porosity=sum(sum(Porosity))/sum(sum(BW2));
%se represents the stater point for the eroded surface. A disk is chosen to
%remove data in a circular pattern from the outer edge of the sample. 62
%represents a circle of 20 micron diameter (62*162nm = 10 micron radius)
se = strel('disk',31);
%A region of 20 microns is eroded from the edge of the trabeculae using
%imerode
erodedBW = imerode(BW2,se);
figure(8);
Slicename=sprintf('%s%s%s%d%s',Pathname_ART, 'Eroded_1_',Filename_ART{i},i,'.tif');
h=imagesc(erodedBW); colormap(gray);
saveas(h,Slicename,'tif');
%Create a binary matrix of the outer ring of the trabeculae for analysis
Eroded_Area=BW2-erodedBW;
figure(9);
Slicename=sprintf('%s%s%s%d%s',Pathname_ART, 'Eroded_ring1_',Filename_ART{i},i,'.tif');
h=imagesc(Eroded_Area); colormap(gray);
saveas(h,Slicename,'tif');
Attenuation_First_5(i)=0;
volume_First_5(i)=0;
First_Total_Volume(i)=0;
Second_Total_Volume(i)=0;
Third_Total_Volume(i)=0;

```

```

Fourth_Total_Volume(i)=0;
Fifth_Total_Volume(i)=0;
Sixth_Total_Volume(i)=0;
Seventh_Total_Volume(i)=0;
Eighth_Total_Volume(i)=0;
Inside_Total_Volume(i)=0;

for j=1:1:width
    for k=1:1:height
        First_5_microns(j,k,1)=Eroded_Area(j,k,1)*BW(j,k,1);
        if First_5_microns(j,k,1) >0
            Attenuation_First_5(i)=First_5_microns(j,k,1)+Attenuation_First_5(i);
            volume_First_5(i)=volume_First_5(i)+1;
        end
        if Eroded_Area(j,k,1)>0
            First_Total_Volume(i)=First_Total_Volume(i)+1;
        end
    end
end
Results(1,i)=Attenuation_First_5(i);
Results(2,i)=volume_First_5(i);
Results(3,i)=First_Total_Volume(i);
%Caluclate the TMD for the next 5 microns
erodedBW_2 = imerode(erodedBW,se);
figure(10);
Slicename=sprintf('%s%s%s%d%s',Pathname_ART, 'Eroded_2_',Filename_ART{i},i,'.tif');
h=imagesc(erodedBW_2); colormap(gray);
saveas(h,Slicename,'tif');
%Create a binary matrix of the outer ring of the trabeculae for analysis
Eroded_Area2=erodedBW-erodedBW_2;
figure(11);
Slicename=sprintf('%s%s%s%d%s',Pathname_ART, 'Eroded_ring2_',Filename_ART{i},i,'.tif');
h=imagesc(Eroded_Area2); colormap(gray);
saveas(h,Slicename,'tif');
Attenuation_Second_5(i)=0;
volume_Second_5(i)=0;

for j=1:1:width
    for k=1:1:height
        Next_5_microns(j,k,1)=Eroded_Area2(j,k,1)*BW(j,k,1);
        if Next_5_microns(j,k,1) >0
            Attenuation_Second_5(i)=Next_5_microns(j,k,1)+Attenuation_Second_5(i);
            volume_Second_5(i)=volume_Second_5(i)+1;
        end
        if Eroded_Area2(j,k,1)>0

```

```

        Second_Total_Volume(i)=Second_Total_Volume(i)+1;
    end

end
end
Results(4,i)=Attenuation_Second_5(i);
Results(5,i)=volume_Second_5(i);
Results(6,i)=Second_Total_Volume(i);
%Caluclate the TMD for the next 5 microns (Third)
erodedBW_3 = imerode(erodedBW_2,se);
figure(10)
Slicename=sprintf('%s%s%s%d%s',Pathname_ART, 'Eroded_3_',Filename_ART{i},i, '.tif');
h=imagesc(erodedBW_3); colormap(gray);
saveas(h,Slicename, 'tif');
%Create a binary matrix of the outer ring of the trabeculae for analysis
Eroded_Area3=erodedBW_2-erodedBW_3;
figure(11)
Slicename=sprintf('%s%s%s%d%s',Pathname_ART, 'Eroded_ring3_',Filename_ART{i},i, '.tif');
h=imagesc(Eroded_Area3); colormap(gray);
saveas(h,Slicename, 'tif');
Attenuation_Third_5(i)=0;
volume_Third_5(i)=0;

for j=1:1:width
    for k=1:1:height
        Third_5_microns(j,k,1)=Eroded_Area3(j,k,1)*BW(j,k,1);
        if Third_5_microns(j,k,1) >0
            Attenuation_Third_5(i)=Third_5_microns(j,k,1)+Attenuation_Third_5(i);
            volume_Third_5(i)=volume_Third_5(i)+1;
        end
        if Eroded_Area3(j,k,1)>0
            Third_Total_Volume(i)=Third_Total_Volume(i)+1;
        end
    end

end
end
Results(7,i)=Attenuation_Third_5(i);
Results(8,i)=volume_Third_5(i);
Results(9,i)=Third_Total_Volume(i);
%Caluclate the TMD for the next 5 microns (Fourth)
erodedBW_4 = imerode(erodedBW_3,se);
figure(10)
Slicename=sprintf('%s%s%s%d%s',Pathname_ART, 'Eroded_4_',Filename_ART{i},i, '.tif');
h=imagesc(erodedBW_4); colormap(gray);
saveas(h,Slicename, 'tif');

```

```

%Create a binary matrix of the outer ring of the trabeculae for analysis
Eroded_Area4=erodedBW_3-erodedBW_4;
figure(11)
Slicename=sprintf('%s%s%s%d%s',Pathname_ART, 'Eroded_ring4_',Filename_ART{i},i,'.tif');
h=imagesc(Eroded_Area4); colormap(gray);
saveas(h,Slicename,'tif');
Attenuation_Fourth_5(i)=0;
volume_Fourth_5(i)=0;

for j=1:1:width
    for k=1:1:height
        Fourth_5_microns(j,k,1)=Eroded_Area4(j,k,1)*BW(j,k,1);
        if Fourth_5_microns(j,k,1) >0
            Attenuation_Fourth_5(i)=Fourth_5_microns(j,k,1)+Attenuation_Fourth_5(i);
            volume_Fourth_5(i)=volume_Fourth_5(i)+1;
        end
        if Eroded_Area4(j,k,1)>0
            Fourth_Total_Volume(i)=Fourth_Total_Volume(i)+1;
        end
    end
end
end
Results(10,i)=Attenuation_Fourth_5(i);
Results(11,i)=volume_Fourth_5(i);
Results(12,i)=Fourth_Total_Volume(i);
%Caluclate the TMD for the next 5 microns (Fifth)
erodedBW_5 = imerode(erodedBW_4,se);
figure(10)
Slicename=sprintf('%s%s%s%d%s',Pathname_ART, 'Eroded_5_',Filename_ART{i},i,'.tif');
h=imagesc(erodedBW_5); colormap(gray);
saveas(h,Slicename,'tif');
%Create a binary matrix of the outer ring of the trabeculae for analysis
Eroded_Area5=erodedBW_4-erodedBW_5;
figure(11)
Slicename=sprintf('%s%s%s%d%s',Pathname_ART, 'Eroded_ring5_',Filename_ART{i},i,'.tif');
h=imagesc(Eroded_Area5); colormap(gray);
saveas(h,Slicename,'tif');
Attenuation_Fifth_5(i)=0;
volume_Fifth_5(i)=0;

for j=1:1:width

    for k=1:1:height
        Fifth_5_microns(j,k,1)=Eroded_Area5(j,k,1)*BW(j,k,1);
        if Fifth_5_microns(j,k,1) >0
            Attenuation_Fifth_5(i)=Fifth_5_microns(j,k,1)+Attenuation_Fifth_5(i);

```

```

        volume_Fifth_5(i)=volume_Fifth_5(i)+1;
    end
    if Eroded_Area5(j,k,1)>0
        Fifth_Total_Volume(i)=Fifth_Total_Volume(i)+1;
    end
end
end
Results(13,i)=Attenuation_Fifth_5(i);
Results(14,i)=volume_Fifth_5(i);
Results(15,i)=Fifth_Total_Volume(i);
%Caluclate the TMD for the next 5 microns (Sixth)
erodedBW_6 = imerode(erodedBW_5,se);
figure(10)
Slicename=sprintf('%s%s%s%d%s',Pathname_ART, 'Eroded_6_',Filename_ART{i},i,'.tif');
h=imagesc(erodedBW_6); colormap(gray);
saveas(h,Slicename,'tif');
%Create a binary matrix of the outer ring of the trabeculae for analysis
Eroded_Area6=erodedBW_5-erodedBW_6;
figure(11)
Slicename=sprintf('%s%s%s%d%s',Pathname_ART, 'Eroded_ring6_',Filename_ART{i},i,'.tif');
h=imagesc(Eroded_Area6); colormap(gray);
saveas(h,Slicename,'tif');
Attenuation_Sixth_5(i)=0;
volume_Sixth_5(i)=0;

for j=1:1:width
    for k=1:1:height
        Sixth_5_microns(j,k,1)=Eroded_Area6(j,k,1)*BW(j,k,1);
        if Sixth_5_microns(j,k,1) >0
            Attenuation_Sixth_5(i)=Sixth_5_microns(j,k,1)+Attenuation_Sixth_5(i);
            volume_Sixth_5(i)=volume_Sixth_5(i)+1;
        end
        if Eroded_Area6(j,k,1)>0
            Sixth_Total_Volume(i)=Sixth_Total_Volume(i)+1;
        end
    end
end
end
Results(16,i)=Attenuation_Sixth_5(i);
Results(17,i)=volume_Sixth_5(i);
Results(18,i)=Sixth_Total_Volume(i);
%Caluclate the TMD for the next 5 microns (Seventh)
erodedBW_7 = imerode(erodedBW_6,se);
figure(10)
Slicename=sprintf('%s%s%s%d%s',Pathname_ART, 'Eroded_7_',Filename_ART{i},i,'.tif');
h=imagesc(erodedBW_7); colormap(gray);

```

```

saveas(h,Slicename,'tif');
%Create a binary matrix of the outer ring of the trabeculae for analysis
Eroded_Area7=erodedBW_6-erodedBW_7;
figure(11)
Slicename=sprintf('%s%s%s%d%s',Pathname_ART, 'Eroded_ring7_',Filename_ART{i},i,'.tif');
h=imagesc(Eroded_Area7); colormap(gray);
saveas(h,Slicename,'tif');
Attenuation_Seventh_5(i)=0;
volume_Seventh_5(i)=0;

for j=1:1:width
    for k=1:1:height
        Seventh_5_microns(j,k,1)=Eroded_Area7(j,k,1)*BW(j,k,1);
        if Seventh_5_microns(j,k,1) >0
            Attenuation_Seventh_5(i)=Seventh_5_microns(j,k,1)+Attenuation_Seventh_5(i);
            volume_Seventh_5(i)=volume_Seventh_5(i)+1;
        end
        if Eroded_Area7(j,k,1)>0
            Seventh_Total_Volume(i)=Seventh_Total_Volume(i)+1;
        end
    end
end
end
Results(19,i)=Attenuation_Seventh_5(i);
Results(20,i)=volume_Seventh_5(i);
Results(21,i)=Seventh_Total_Volume(i);
%Caluclate the TMD for the next 5 microns (Eighth)
erodedBW_8 = imerode(erodedBW_7,se);
figure(10)
Slicename=sprintf('%s%s%s%d%s',Pathname_ART, 'Eroded_8_',Filename_ART{i},i,'.tif');
h=imagesc(erodedBW_8); colormap(gray);
saveas(h,Slicename,'tif');
%Create a binary matrix of the outer ring of the trabeculae for analysis
Eroded_Area8=erodedBW_7-erodedBW_8;
figure(11)
Slicename=sprintf('%s%s%s%d%s',Pathname_ART, 'Eroded_ring8_',Filename_ART{i},i,'.tif');
h=imagesc(Eroded_Area8); colormap(gray);
saveas(h,Slicename,'tif');
Attenuation_Eighth_5(i)=0;
volume_Eighth_5(i)=0;

for j=1:1:width
    for k=1:1:height
        Eighth_5_microns(j,k,1)=Eroded_Area8(j,k,1)*BW(j,k,1);
        if Eighth_5_microns(j,k,1) >0
            Attenuation_Eighth_5(i)=Eighth_5_microns(j,k,1)+Attenuation_Eighth_5(i);

```

```

        volume_Eighth_5(i)=volume_Eighth_5(i)+1;
    end
    if Eroded_Area8(j,k,1)>0
        Eighth_Total_Volume(i)=Eighth_Total_Volume(i)+1;
    end
end
end
Results(22,i)=Attenuation_Eighth_5(i);
Results(23,i)=volume_Eighth_5(i);
Results(24,i)=Eighth_Total_Volume(i);

%Caluclate the TMD for the Center

Attenuation_Center(i)=0;
volume_Center(i)=0;

for j=1:1:width
    for k=1:1:height
        Center(j,k,1)=erodedBW_8(j,k,1)*BW(j,k,1);
        if Center(j,k,1) >0
            Attenuation_Center(i)=Center(j,k,1)+Attenuation_Center(i);
            volume_Center(i)=volume_Center(i)+1;
        end
        if erodedBW_8(j,k,1)>0
            Inside_Total_Volume(i)=Inside_Total_Volume(i)+1;
        end
    end
end
end
Results(25,i)=Attenuation_Center(i);
Results(26,i)=volume_Center(i);
Results(27,i)=Inside_Total_Volume(i);

LAC_Volume(i)=0;
Lacunae_Volume(i)=0;
Total_Volume(i)=0;
se=strel('disk',6);
BW3=imerode(Porosity,se);
BW3=imdilate(BW3,se);
figure(12)
Slicename=sprintf('%s%s%s%d%s',Pathname_ART, 'lacunae',Filename_ART{i},i, '.tif');
h=imagesc(BW3); colormap(gray);
saveas(h,Slicename,'tif');
for j=1:1:width
    for k=1:1:height
        LAC(j,k,1)=BW2(j,k,1)*BW3(j,k,1);
    end
end

```

```

    if LAC(j,k,1) >0
        Lacunae_Volume(i)=Lacunae_Volume(i)+1;

    end
    if BW2(j,k,1)>0
        Total_Volume(i)=Total_Volume(i)+1;
    end
    if BW(j,k,1)>0
        LAC_Volume(i)=LAC_Volume(i)+1;
    end
end
end
Results(28,i)=LAC_Volume(i);
Results(29,i)=Lacunae_Volume(i);
Results(30,i)=Total_Volume(i);

end

xlswrite('Porosity2',Results,'1L_2')

```

Code for Calculating the Lacunar-Canalicular Network

```

%This program is written for thresholding and calculating the BMD of slices
%of bone taken with TXM at the Stanford Synchrotron Radiation Lightsource.
%Input files should be in the format of a slice file with extension *.bin

% Values output are the bone mineral density and the porosity of the bone.

%Code written by Garry Brock, January 2014

%close all open GUIs and clear all data variables
clear all
close all
clc

%set up general variables for attenuation and volume
Attenuation=0;
Volume=0;
%Import files into matlab, select multiple files at once
[Filename_ART, Pathname_ART] = uigetfile('*.binslice','Please select set of ART files for
determination of mineral content ','multiselect','on')
filename_size=size(Filename_ART)
%Read in all of the data and save the image stack in a 3D matrix. Must have
%TXM binary .m files in the same folder for this to work!
for i=1:1:filename_size(1,2)

```

```

    rn = sprintf('%s%s', Pathname_ART, Filename_ART{i});
[image_ART(:, :, i) metadata] = readfile(rn);

[image_width image_height]=size(image_ART);

end
%
% [Filename_FBP, Pathname_FBP] = uigetfile('*.*binslice','Please select set of FBP files for
determination of mineral content ','multiselect','on')
% filename_size=size(Filename_FBP)
% %Read in all of the data and save the image stack in a 3D matrix. Must have
% %TXM binary .m files in the same folder for this to work!
% for i=1:1:filename_size(1,2)
%     rn = sprintf('%s%s', Pathname_FBP, Filename_FBP{i});
% [image_FBP(:, :, i) metadata] = readfile(rn);
%
% [image_width image_height]=size(image_FBP);
%
% end

%%%%%%%%%%%%%% Code to Threshold the ART Image %%%%%%%%%%%%%%%

%resize matrix to more managable size for thresholding (use 10% of data
image_small=imresize(image_ART,0.01);
Image_Hist=image_small(:);
[Data Counts]=hist(Image_Hist,2000);
h=plot(Counts, Data)
%Plot and save a histogram of all of the data
Slicename=sprintf('%s%s%s',Pathname_ART, 'Hist_of_all_data','.tif');
saveas(h,Slicename,'tif')
[xstart,ystart]=ginput(1);
    [xend,yend]=ginput(1);
    %Choose points before and after the start of the gaussian region
    lin_start = xstart; %input('Start of linear region? ');
    lin_end = xend; %input('End of linear region? ');
    lin_region_start = min(find(Counts>lin_start));
    lin_region_end = min(find(Counts>lin_end));
    %lin_region_start = min(find(dis>.4));
    %lin_region_end = min(find(dis>.7));
    Counts_cut = Counts(lin_region_start:lin_region_end);
    Data_cut = Data(lin_region_start:lin_region_end);
    %Fit a gaussian peak to the section of data
[f,gof,output] = fit(Counts_cut',Data_cut','gauss1')
figure(2)
%save image including the gaussian peak

```

```

h=plot(f,Counts_cut',Data_cut')
Slicename=sprintf('%s%s%s',Pathname_ART, 'Cut_Hist','tiff');
saveas(figure(2),Slicename,'tiff')
%the mean is the second output of the gaussian function and the standard
%deviation is half of the third output
mean=f.b1;
sd=(f.c1)/2;

%create low and high thresholds by taking the mean plus or minus 3SD
%(should include 99.7 percent of the data thoeretically
Low_Thresh=mean-3*sd;
High_Thresh=mean+4*sd;

%Use the low and high threshold to remove the gold beads and background.
%Everything not falling within the bone region is changed to be a value of
%zero
[width height]=size(image_ART(:,:,1));
for i=1:1:width
    for j=1:1:height
        for k=1:1:filename_size(1,2)
            if image_ART(i,j,k)<Low_Thresh
                image_ART(i,j,k)=0;
            end
            if image_ART(i,j,k)>High_Thresh
                image_ART(i,j,k)=0;
            end
        end
    end
end

end
end

for i=1:1:filename_size(1,2)
    i
    %thresholded image is converted to black and white binary image
    BW=im2bw(image_ART(:,:,i),0.0000001);
    figure(3);
    Slicename=sprintf('%s%s%s%d%s',Pathname_ART, 'BW_',Filename_ART{i},i,'tiff');
    h=imagesc(BW); colormap(gray);
    saveas(h,Slicename,'tiff')

%Lacunae and canaliculi within the sample are filled in to get a bone
%volume
se = strel('disk',155);
conn=conndef(2,'maximal');
BW2 = imfill(BW,conn,'holes');

```

```

BW2=imdilate(BW2,se);
BW2=imfill(BW2,conn,'holes');
BW2=imerode(BW2,se);

figure(4);
Slicename=sprintf('%s%s%s%d%s',Pathname_ART, 'BW_filled_',Filename_ART{i},i,'.tif');
h=imagesc(BW2); colormap(gray);
saveas(h,Slicename,'tif')

BW_inv=imcomplement(BW);
figure(5);
Slicename=sprintf('%s%s%s%d%s',Pathname_ART, 'inverse_BW_',Filename_ART{i},i,'.tif');
h=imagesc(BW_inv); colormap(gray);
saveas(h,Slicename,'tif')

BW2_inv=imcomplement(BW2);
figure(6);
Slicename=sprintf('%s%s%s%d%s',Pathname_ART,
'inverse_BW_filled_',Filename_ART{i},i,'.tif');
h=imagesc(BW2_inv); colormap(gray);
saveas(h,Slicename,'tif')

Porosity=imcomplement(BW+BW2_inv);
figure(7);
Slicename=sprintf('%s%s%s%d%s',Pathname_ART, 'LAC_network_',Filename_ART{i},i,'.tif');
h=imagesc(Porosity); colormap(gray);
saveas(h,Slicename,'tif')
%
% Percent_porosity=sum(sum(Porosity))/sum(sum(BW2));
%
% for j=1:1:width
%   for k=1:1:height
%     LAC(j,k,1)=BW(j,k,1)*BW2(j,k,1);
%   end
% end
% Slicename=sprintf('%s%s%s%d%s',Pathname_ART, 'LAC_',Filename_ART{i},i,'.tif');
% h=imagesc(LAC); colormap(gray);
% saveas(h,Slicename,'tif')
end

```